Charge Symmetry Violation in the Extraction of Strangeness Form Factors of the Nucleon

Ali Abdullah M. Alkathiri

Supervisors:
Assoc. Prof. Ross D. Young
Assoc. Prof. James M. Zanotti

A thesis submitted towards the degree of
Doctor of Philosophy

Faculty of Sciences
School of Physical Sciences
Department of Physics

March 2019

Abstract

The strange quark contributions to the electromagnetic form factors of the proton are ideal quantities to study the role of hidden flavour in the properties of the proton. This has motivated intense experimental measurements of these form factors. A major remaining source of systematic uncertainty in these determinations is the assumption that charge symmetry violation (CSV) is negligible. In this analysis, recent theoretical determinations of the CSV form factors are used and the available parity-violating electron scattering (PVES) data, up to $Q^2 \sim 1\text{GeV}^2$, are reanalysed. This analysis considers systematic expansions of the strangeness electric and magnetic form factors of the proton. The results provide an update to the determination of strangeness over a range of Q^2 where, under certain assumptions about the effective axial form factor, an emergence of non-zero strangeness is revealed in the vicinity of $Q^2 \sim 0.6$ GeV^2. Given the recent theoretical calculations, it is apparent that the current limits on the CSV do not have a significant impact on the interpretation of the measurements and hence suggests an opportunity for a next generation of parity-violating measurements to more precisely map the distribution of strange quarks.

The size of the γZ box correction is particularly significant to the Standard Model (SM) test by the Q_{weak} Experiment. The uncertainties that arise from the underlying γZ interference structure functions can be constrained by phenomenological models such as the Adelaide-Jefferson Lab-Manitoba (AJM) model. Recently, a new lattice method was proposed to compute the structure functions directly from a lattice calculation of the electromagnetic Compton amplitude $T_1^{\gamma\gamma}$. This method paves the way for a possible extension that involves studying the γZ interference Compton amplitude $T_1^{\gamma Z}$ at low Q^2. The question about the required accuracy of $T_1^{\gamma Z}$ on the lattice to improve the phenomenological models was studied.

Statement of Originality

I certify that this work contains no material which has been accepted for the award of any other degree or diploma in my name, in any university or other tertiary institution and, to the best of my knowledge and belief, contains no material previously published or written by another person, except where due reference has been made in the text. In addition, I certify that no part of this work will, in the future, be used in a submission in my name, for any other degree or diploma in any university or other tertiary institution without the prior approval of the University of Adelaide and where applicable, any partner institution responsible for the joint-award of this degree.

I give permission for the digital version of my thesis to be made available on the web, via the University's digital research repository, the Library Search and also through web search engines, unless permission has been granted by the University to restrict access for a period of time.

Ali Abdullah M. Alkathiri

Acknowledgements

First and foremost, I thank God Almighty for the wisdom and perseverance that He has bestowed upon me during this research.

Throughout writing this thesis, a number of people have greatly supported me, for whom I am extremely grateful. Thus, I would like to take this opportunity to thank them.

I owe my deepest gratitude to my supervisors, Ross Young and James Zanotti, for their helpful comments, motivation and stimulating discussions. They have been there providing their heartfelt support at all times during this research. Without their guidance, this thesis would not have been possible and I shall be eternally grateful to them for their encouragements.

Also, I would like to thank Wally Melnitchouk and Nathan Hall for useful discussions and their helpful comments on my questions.

I would also like to express my gratitude to the CSSM and School of Physical Sciences staff. In particular, I thank Sharon Johnson and Silvana Santucci for their administrative support. I also thank Ramona Adorjan for her computing and technical assistance. Thanks to Scribendi centre for proofreading my thesis.

I would like to express my sincere gratitude to my sponsor in Saudi Arabia, Taif University, for the financial support to complete my Master's degree and PhD at the University of Adelaide. I thank the Saudi Culture Mission in Australia for the administrative communication with my sponsor in Saudi Arabia.

I would like to extend my thanks to my officemates, Zachary Koumi, Anum Qureshi, Marco Santoni and Dylan Harries for chat times.

I would like also to thank my friends outside the university. Special thanks go to my friends Hasan Assaedi and Batil Alharbi for their wonderful friendship and for everything that they have done to help me.

Unlimited thanks also go to my parents for their warm support. They always help me to be optimistic when I encounter a challenge. They taught me that my job in life is to learn with patience and see the best in people. I would also like extend my very warm thanks and sincere appreciation to my wife, Badriah, who was my main source of continual love and support during this research, even when she was overseas. She encouraged me to put forth my best effort throughout this research. These acknowledgments would not be complete without thanking my children Khalid, Faris and Reem. I thank my little children for making me so happy with their adorable smiles.

I dedicate this work to my son Khalid whom I missed during my Master degree program. Someday I hope my son would be able to understand my situation. Much love and hugs for you Khalid from your Dad.

Contents

List of Figures

List of Tables

List of Abbreviations

DIS	Deep Inelastic Scattering
SLAC	Stanford Linear Accelerator Center
SM	Standard Model
QCD	Quantum Chromodynamics
PV	Parity-Violating
PDG	Particle Data Group
$\overline{\mathrm{MS}}$	Modified Minimal Subtraction
LHC	Large Hadron Collider
μ_N	Nuclear Magneton
ChPT	Chiral Perturbation Theory
BChPT	Heavy Baryon Chiral Perturbation Theory
EMC	European Muon Collaboration
QPM	Quark-Parton Model
PVES	Parity-Violating Electron Scattering
EM	Electromagnetic
NuTeV	Neutrinos at the Tevatron
CDHS	CERN-Dortmund-Heidelberg-Saclay
CCFR	Columbia-Chicago-Fermilab-Rochester
VMD	Vector Meson Dominance
NJL	Nambu and Jona-Lasinio Model
LQCD	Lattice Quantum Chromodynamics
ppm	Parts Per Million

OSR	On-Shell Renormalisation
SAMPLE	Singlet Anomalous Moment of the Proton using Longitudinally Polarized Electrons
HAPPEx	Hall A Proton Parity Experiment
AJM	Adelaide-Jefferson Lab-Manitoba
PDFs	Parton Distribution Functions
CB	Christy and Bosted
LO	Leading Order
NLO	Next-Leading Order
OPE	Operator Product Expansion
CSV	Charge Symmetry Violation

Chapter 1

Introduction

In 1911, Ernest Rutherford introduced his atomic theory that describes the atomic structure as possessing a central charge (later known as a positive nucleus) surrounded by a cloudy negative distribution of orbiting electrons. He developed his theory based on the results of an experiment of shooting a beam of alpha particles through a thin foil of gold. That results proved the existence of the atomic nucleus where a small portion of alpha particles was scattered back from the gold sheet, while a large percentage of these particles passed through the sheet with no deflection.

In 1919, Rutherford proved the existence of the hydrogen nucleus in other nuclei based on results from an experiment in which alpha particles were fired into the nitrogen gas, and the produced hydrogen nuclei were detected by scintillation detectors. This result described as the discovery of the proton.

In 1964, the quark model was individually developed by Murray Gell-Mann and George Zweig. In 1968, deep inelastic scattering (DIS) experiments at the Stanford Linear Accelerator Center (SLAC) verified that the proton consists of point-like particles. These particles were later known as up (u) and down (d) quarks. The DIS experiments indirectly confirmed the existence of strange (s) quark that plays a fundamental role in describing the kaons that have been discovered in cosmic rays in 1947.

The Standard Model (SM) of particle physics is a theoretical framework which presently renders the best explanation of the interactions and properties of the elementary particles. These elementary particles are divided into leptons, quarks and gauge bosons. Leptons and quarks form the fundamental constituents of matter, while bosons are the force carriers of different interactions between leptons and quarks. The SM is a combination of the quantum chromodynamics (QCD), which describes the strong interaction between gluons and quarks in the nucleon, and the electroweak theory. The electroweak theory is a unified theory of two fundamental interactions, the electromagnetic and the weak interactions.

In the SM, nucleons are formed of their valence quarks, i.e., proton and neutron with valence quark content (uud) and (udd), respectively, in addition to virtual QCD vacuum-generated quark-antiquark pairs that emerge and annihilate in the quark-gluon sea inside the nucleon. At high-energy regions where the physics is perturbative, QCD can describe strong interaction and hadronic phenomena, for example, 'colour confinement'. However, at low-energy regions where the theory is nonperturbative, the situation is more complicated.

Theoretically, the sea quarks can consist of any of the six different flavours of quarks, i.e., up (u), down (d), strange (s), charm (c), beauty (b) and top (t), however, the most possible quark-antiquark pairs comprise u, d and s quarks. Generally, it is challenging to separate the sea u and d quark contributions from their corresponding valence quarks. However, the s quark contributions are totally from the sea. Despite the strangeness, which is a quantum number that was introduced in the 1950s by Gell-Mann and Nishijima, of nucleons being zero, the s quarks could have a space-time distribution inside the nucleons. Therefore, questions can be raised about the strange quark's contribution to the static properties of the nucleon.

The investigation of the strange quark contributions, that would necessarily be related to the 'sea', to the nucleon static properties such as mass (scalar matrix elements), the electromagnetic properties (vector matrix elements) and the spin (axial vector matrix elements), is particularly interesting. The two quantities usually considered in the context of the strange quark contributions at low momentum transfers are the strange charge radius and the strange magnetic moment.

The SM electroweak theory, which has been developed in the last half-century, introduced successful tools to study the structure of the nucleon using the weak interaction. The parity-violating (PV) interaction of electron with nucleon renders information on the weak neutral current of nucleon and its related quark structure, including sensitivity to strange quark-antiquark effects.

In Chapter 2, a brief overview of the SM is presented as it is the main framework of this study. Since the interference of the weak and electromagnetic interactions has a particular focus, a short introduction to the electroweak theory is also included. Although the SM has demonstrated its successes in predicting many experimental results, it is seen as incomplete. Performing precision measurements can be utilised as a SM test. In Section 2.3, as an example, the Q_{weak} experiment, which placed new constraints on search for new physics, is briefly highlighted.

It is instructive to highlight, in general, the role of the strange quark within nucleon structure. Chapter 3 describes the physics of strange quark-antiquark pairs $\overline{s}s$ in the nucleon and provides motivation for the PV electron scattering method to study the strange quark content of the nucleon.

A survey of different theoretical approaches to studying the strangeness contribution to the electromagnetic (EM) vector form factors of the nucleon will be presented in Chapter 4, concentrating on their predictions of the strange magnetic form factor G_M^s and strange electric form factor G_E^s at zero momentum transfer $Q^2 = 0$, i.e., focusing on the strange magnetic moment $\mu_s \equiv G_M^s(Q^2 = 0)$ and the strangeness mean-square radius $\langle r_s^2 \rangle_E = -6 \; dG_E^s(Q^2)/dQ^2(Q^2 = 0)$. Other definitions of charge radius are certainly possible, but this is the most common one in the literature.

In addition to the purely electromagnetic interaction, which dominates electron scattering, the electron also interacts via the weak interaction. Although the weak interaction, which violates parity, is several orders of magnitude smaller than the electromagnetic interaction, which conserves parity, the weak interaction can play an important role in studying a part of nucleon structure that cannot be investigated through studies that only consider the electromagnetic interaction.

In 1988, Kaplan and Manohar [1] suggested that the strange electric and magnetic form factor contributions can be estimated through measurements of the weak neutral current matrix elements. In the following year, McKeown [2] and Beck [3] suggested an experimental program to measure the weak neutral current of the proton using PV electron scattering in order to estimate the strange quark contribution to the vector matrix elements.

Chapter 5 considers the formalism involved in the description of PV asymmetry for elastic electron-proton scattering, elastic electron-helium-4 scattering and quasielastic electron-deuteron scattering. Higher-order electroweak corrections will also be highlighted and included in the analysis of this work. In the present work, the axial-vector form factors encode higher-order radiative corrections and hadronic anapole contributions, and the dominant contribution is determined by the considered data set. In Section 5.4, the main experimental programs that discuss PV electron scattering from the proton, helium-4 or deuteron with varying kinematic conditions and measured A_{PV} will be summarised. The set of all available PV electron scattering data, up to the currently available limit of $Q^2 \sim 1\text{GeV}^2$, is presented at the end of this chapter.

Chapter 6 will serve to illustrate the analysis of the considered dataset to determine the form factors of the strange quark content. A major remaining source of systematic uncertainty in these determinations is the assumption that charge symmetry violation (CSV) is negligible. In Section 6.3, CSV effects will be investigated using theoretical CSV calculations.

The strangeness content of the proton acts as a background role in precisely interpreting, for example, the Q_{weak} [4] or P2 [5] collaborations measurements of the proton's weak charge Q_W^p. In contrast to the formalism relevant to atomic parity violation experiments, an energy-dependent correction arising from the γZ box correction was highlighted by Gorchtein and Horowitz [6]. The size of this correction is particularly significant to the standard model test by the Q_{weak} Experiment [4]. The most recent calculation of the γZ box correction will be used in the global analysis introduced in Chapter 6 with utilising the updated relevant inputs presented in 2016 PDG.

The γZ box correction, so far, is understood within phenomenological models such as Adelaide-Jefferson Lab-Manitoba (AJM) model [7]. A recent new lattice method has been proposed to compute the structure functions directly from a lattice calculation of the electromagnetic Compton amplitude $T_1^{\gamma\gamma}$ [8]. This method opens the door for a possible extension involving the γZ interference Compton amplitude $T_1^{\gamma Z}$ at low Q^2. In Chapter 7, the question of what accuracy of $T_1^{\gamma Z}$ on the lattice is necessary to improve the phenomenological models will be studied.

Finally, in Chapter 8, the results of this work will be summarised to draw a complete picture about CSV effects and the strange quark electromagnetic form factors in the nucleon properties. Some main conclusions about the phenomenological models of the γZ box correction also will be revisited.

Chapter 2

The Standard Model and Beyond

The Standard Model (SM) of particle physics describes the present understanding of the fundamental particles and their interactions. It is commonly believed that the atoms have a central nucleus surrounded by a cloud of electrons, and that the nucleus is composed of smaller particles, i.e., protons and neutrons. Protons and neutrons, collectively known as nucleons, are made of quarks, which are currently understood to be fundamental particles.

In this chapter, a brief overview of the SM will be introduced. Since this work is essentially done in the context of the interference of the weak and electromagnetic interactions, a short introduction to the electroweak theory will be presented.

In spite of the tremendous achievements of the SM, it does not adequately explain some phenomena. Performing precision measurements can therefore provide a test of the SM. In Section 2.3, as an example, the Q_{weak} experiment [4], which places new constraints on search for new physics, will be briefly highlighted. Further useful discussion on electroweak tests can be found in [9–11].

2.1 The Standard Model

The SM of particle physics successfully describes three fundamental forces, electromagnetic, weak and strong interactions.

The SM classifies all known elementary particles into fermions (half-integer spin) and bosons (integer spin). Fermions are divided into three generations of leptons and quarks according to their characteristics, such as, mass and electric charge, while bosons are divided into gauge bosons (force carries, spin$\neq$0) and scalar bosons (spin=0), see Fig. 2.1. The Higgs boson, a massive scalar boson which was recently discovered [12, 13], associated with the Higgs field is responsible for generating mass for fundamental particles in the SM.

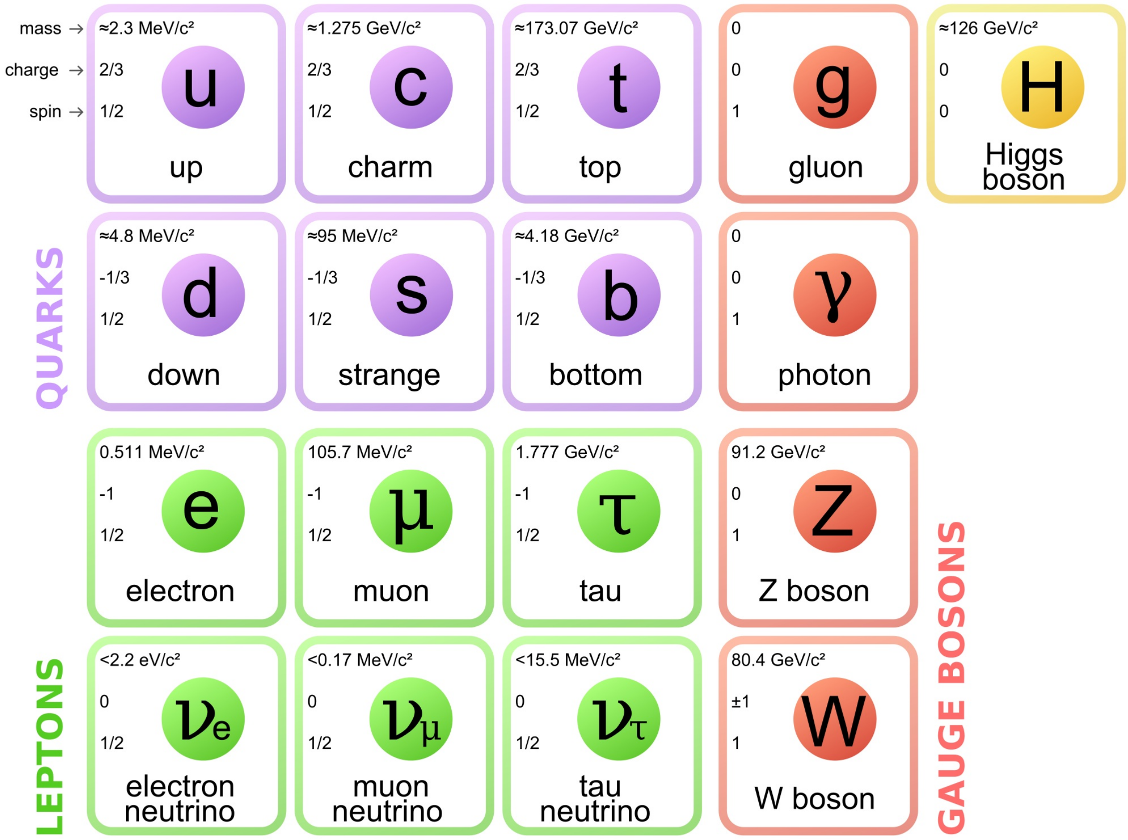

Figure 2.1: The Standard Model (SM) of particle physics. Figure taken from [14].

Based on the $SU(3)_c \times SU(2)_L \times U(1)_Y$ gauge group, the strong interactions are related to the quarks' colour symmetry group $SU(3)_c$, and the electroweak interactions are a result of the $SU(2)_L \times U(1)_Y$. The subscripts c refers to colour, L means that the $SU(2)$ acts only on left-handed fermions and the Y refers to the weak hypercharge.

The interaction between the quarks and leptons that make up matter occurs via the exchange of vector bosons (gauge bosons). The photon carries the electromagnetic force. In the case of QCD, gluons are responsible for the strong force—they combine the quarks to make up mesons (quark-antiquark) and baryons (three bound quarks). Mesons and baryons are collectively called hadrons. The $W^{\pm}$ and Z^0 bosons carry the weak force. Leptons experience only the electromagnetic and weak interactions. Table 2.1 presents the SM forces and their mediating particles (gravitational force is not included).

Each of the SM forces have a 'charge' that can be occupied by the different particles. The 'charge' for the electromagnetic interaction is what is usually thought of as a charge. The weak charges are expressed in terms of the weak mixing angle. The strong colour charge is red, green or blue—composite particles can only exist in

Table 2.1: The SM forces and their carrier particle (gravitational force is not included). The data is taken from Particle Data Group (PDG) [15].

Particle	Mediates Interaction	Mass[GeV]	Q_{EM}
γ	Eelectromagnetic	0	0
$W^{\pm}$, Z^0	Weak	80.4, 91.2	±1, 0
gluons	Strong	0	0

combinations. Table 2.2 shows some of the SM particles (fermions) properties such as the electric charge (Q) and the weak current couplings (g_V and g_A).

The present work utilises the interference of the weak and electromagnetic forces, so the next section will introduce a brief overview of the electroweak theory.

2.2 Electroweak Theory

It has been observed that neutral weak current couple to the particles with different strength. From Table 2.2, the vector coupling g_V is related to the weak isospin and to the electric charge, while the axial-vector coupling g_A is related to the weak isospin. The theoretical basis for the unification of the SM electroweak theory was first introduced by Glashow [16]. Glashow included the Z^0 boson as an extension of electroweak unification models. Under the resulting $SU(2) \times U(1)$ gauge group, the electroweak unification is achieved.

The electroweak Lagrangian that describes the interaction and kinetic terms for the Standard Model fermions and gauge bosons can be given by

$$\begin{aligned}\mathcal{L}_{EW} =& \overline{\chi}_L \gamma^\mu \Big(i\partial_\mu - g\vec{T} \cdot \vec{W}_\mu - g'\frac{Y}{2}B_\mu \Big)\chi_L + \overline{\psi}_R \gamma^\mu \Big(i\partial_\mu - g'\frac{Y}{2}B_\mu \Big)\psi_R \\ & - \frac{1}{4}\vec{W}_{\mu\nu} \cdot \vec{W}^{\mu\nu} - \frac{1}{4}B_{\mu\nu}B^{\mu\nu} \\ =& \overline{\chi}_L \gamma^\mu i\partial_\mu \chi_L - gJ^{i\mu} \cdot W^i_\mu - g'\frac{1}{2}j^{Y\mu}B_\mu + \overline{\psi}_R \gamma^\mu i\partial_\mu \psi_R - g'\frac{1}{2}j^{Y\mu}B_\mu \\ & - \frac{1}{4}\vec{W}_{\mu\nu} \cdot \vec{W}^{\mu\nu} - \frac{1}{4}B_{\mu\nu}B^{\mu\nu},\end{aligned} \tag{2.1}$$

where χ_L refers to the left-handed fermion doublet and ψ_R refers to the right-handed fermion singlet. $\vec{T}$ are the generators of $SU(2)_L$ and are related to the Pauli matrices τ, i.e., $T_i = \frac{\tau_i}{2}$ where $i = 1, 2, 3$ (see Appendix A). The hypercharge Y is the generator of $U(1)_Y$. $\vec{W}_\mu$ and B_μ are the gauge fields associated with $SU(2)_L$ and

Table 2.2: Selected properties of the three generations of SM particles. Q is the electromagnetic charge in units of e. g_V and g_A are the vector and axial-vector weak current couplings, respectively.

	Generation					
Fermions	1	2	3	Q	g_V	g_A
Lepton	ν_e	ν_μ	ν_τ	0	1	-1
	e	μ	τ	-1	$-1+4\sin^2\theta_W$	1
Quark	u	c	t	2/3	$1-8/3\sin^2\theta_W$	-1
	d	s	b	$-1/3$	$-1+4/3\sin^2\theta_W$	1

$U(1)_Y$, respectively. g and g' are the coupling constants. $J^{i\mu}$ is the weak current

$$\begin{aligned} J^{i\mu} =& \overline{\chi}_L \gamma^\mu T_i \chi_L \\ =& \overline{\chi}_L \gamma^\mu \frac{\tau_i}{2} \chi_L, \end{aligned} \tag{2.2}$$

where the third current ($i = 3$) describes the weak neutral current (it does not change the charge of the particle involved in the interaction). $j^{Y\mu}$ is the weak hypercharge current

$$j^{Y\mu} = \overline{\chi}_L \gamma^\mu Y \chi_L + \overline{\psi}_R \gamma^\mu Y \psi_R. \tag{2.3}$$

The electromagnetic current can be defined in terms of the weak neutral current $J^{3\mu}$ and weak hypercharge current $j^{Y\mu}$ as

$$j^{em}_\mu = J^3_\mu + \frac{1}{2} j^Y_\mu, \tag{2.4}$$

or in terms of the generators (Gell-Mann–Nishijima formula) as

$$Q = T^3 + \frac{Y}{2}. \tag{2.5}$$

The field strength $\vec{W}_{\mu\nu}$ and $B_{\mu\nu}$ are given by

$$\begin{aligned} \vec{W}_{\mu\nu} &= \partial_\mu \vec{W}_\nu - \partial_\nu \vec{W}_\mu - g\vec{W}_\mu \times \vec{W}_\nu, \\ B_{\mu\nu} &= \partial_\mu B_\nu - \partial_\nu B_\mu. \end{aligned} \tag{2.6}$$

The Lagrangian Eq. (2.1) is gauge invariant under the $SU(2)_L$ and $U(1)_Y$ transformations. However, in describing the real physics, the $\vec{W}_\mu$ and B_μ need to be replaced by the gauge fields $W^\pm$, Z_μ and A_μ. $W^\pm$ and Z_μ mediate the weak interaction, and A_μ is the photon field that carries the electromagnetic force. $W^\pm$ bosons couple only to the left-handed doublet fermions, and $W^{\pm}$ fields can be written as

$$W^{\pm} = \frac{1}{\sqrt{2}}\Big(W^1_\mu \mp iW^2_\mu\Big). \tag{2.7}$$

Z boson and photon couple to right- and left-handed fermions. Therefore, from mixing of the two vector fields W^3_μ and B_μ, Z_μ and A_μ fields can be defined in terms of W^3_μ and B_μ as

$$\begin{aligned} Z_\mu &= \frac{1}{\sqrt{g^2+g'^2}}\Big(gW^3_\mu - g'B_\mu\Big), \\ A_\mu &= \frac{1}{\sqrt{g^2+g'^2}}\Big(g'W^3_\mu + gB_\mu\Big). \end{aligned} \tag{2.8}$$

Defining the weak mixing angle (Weinberg angle) in terms of the coupling constants g and g' as

$$\sin\theta_W = \frac{g'}{\sqrt{g^2+g'^2}}, \qquad \cos\theta_W = \frac{g}{\sqrt{g^2+g'^2}}, \tag{2.9}$$

leads to redefining Z_μ and A_μ fields as

$$\begin{aligned} Z_\mu &= \cos\theta_W W^3_\mu - \sin\theta_W B_\mu, \\ A_\mu &= \cos\theta_W B_\mu + \sin\theta_W W^3_\mu. \end{aligned} \tag{2.10}$$

Using these expressions allows one to write

$$\begin{aligned} -gJ^3_\mu W^{3\mu} - \frac{g'}{2}j^Y_\mu B^\mu = &-\Big(g\sin\theta_W J^3_\mu + g'\cos\theta_W\frac{j^Y_\mu}{2}\Big)A^\mu \\ &-\Big(g\cos\theta_W J^3_\mu - g'\sin\theta_W\frac{j^Y_\mu}{2}\Big)Z^\mu. \end{aligned} \tag{2.11}$$

In order to obtain the electromagnetic part from A_μ, one needs to apply the condition

$$g\sin\theta_W = g'\cos\theta_W = e. \tag{2.12}$$

Hence, Eq. (2.11) becomes

$$\begin{aligned}
-gJ^3_\mu W^{3\mu} - \frac{g'}{2} j^Y_\mu B^\mu =& - e j^{em}_\mu A^\mu - \frac{g}{\cos\theta_W}(J^3_\mu - \sin^2\theta_W) Z^\mu \\
=& - e \sum_f Q_f \overline{\psi}_f \gamma_\mu \psi_f A^\mu \\
& - \frac{g}{\cos\theta_W} \sum_f \overline{\psi}_f \gamma_\mu \Big[\frac{1}{2}(1-\gamma^5) T^3_f - \sin^2\theta_W Q_f\Big] \psi_f Z^\mu \\
=& - e \sum_f Q_f \overline{\psi}_f \gamma_\mu \psi_f A^\mu \\
& - \frac{g}{4\cos\theta_W} \sum_f \overline{\psi}_f \gamma_\mu \Big[g^f_V + g^f_A \gamma^5\Big] \psi_f Z^\mu, \qquad (2.13)
\end{aligned}$$

where $g^f_V = 2T^3_f - 4Q_f \sin^2\theta_W$ and $g^f_A = -2T^3_f$[1]. Note that for the fermions, the above equation should be applied to their chiral components separately.

The Electroweak Lagrangian can be rewritten as

$$\begin{aligned}
\mathcal{L}_{EW} =& \overline{\chi}_L \gamma^\mu i\partial_\mu \chi_L + \overline{\psi}_L \gamma^\mu i\partial_\mu \psi_L \\
& - \frac{g}{\sqrt{2}}\Big(J^{+\mu} W^+_\mu + J^{-\mu} W^-_\mu\Big) \\
& - e j^{em\mu} A_\mu - \frac{g}{4\cos\theta_W} J^{NC\mu} Z_\mu \\
& - \frac{1}{4} \vec{W}_{\mu\nu} \cdot \vec{W}^{\mu\nu} - \frac{1}{4} B_{\mu\nu} B^{\mu\nu}, \qquad (2.14)
\end{aligned}$$

where $j^{em\mu}$ is the usual electromagnetic current,

$$j^{em\mu} = \sum_f Q_f \overline{\psi}_f \gamma^\mu \psi_f, \qquad (2.15)$$

and $J^{NC\mu}$ is the weak neutral current,

$$J^{NC\mu} = \sum_f \overline{\psi}_f \gamma^\mu \Big[g^f_V + g^f_A \gamma_5\Big] \psi_f. \qquad (2.16)$$

The gauge symmetry prevents the gauge bosons from acquiring masses, i.e., mass terms for any gauge bosons are prohibited since they are not invariant under gauge transformations. Fermion masses are also prohibited because they mix left- right-handed fields and therefore violate gauge invariance. Thus, the above Lagrangian contains massless fields. In order to generate the masses of the physical particles, the

---

[1] The convention used in [10] has been followed in this work. In the literature, the charged and neutral currents are affected by a factor of $\frac{1}{2}$. To overcome this difference, one simply needs to redefine the coupling constants in the scattering amplitude.

symmetry gauge theory of electroweak interactions is spontaneously broken [17, 18] when adding a complex scalar Higgs doublet $\phi = \begin{pmatrix} \phi^+ \\ \phi^0 \end{pmatrix}$ to the model with potential given by

$$V(\phi) = \mu^2 \phi^\dagger \phi + \frac{\lambda}{2}(\phi^\dagger \phi)^2. \tag{2.17}$$

This is called the Higgs mechanism [19–22], Fig. 2.2.

For negative μ^2 and positive λ, the ground state of the potential $V(\phi)$ does not appear at $\phi = 0$. Since there is a circle of minima (an infinite number of minima) centered around $\phi = 0$, the choice of the minimum is arbitrary, see Fig. 2.2. By convention, the minimum of the form

$$\phi_0 = \frac{1}{\sqrt{2}} \begin{pmatrix} 0 \\ v \end{pmatrix} \tag{2.18}$$

has been chosen, where v is the vacuum expectation value. This approach of obtaining an asymmetric ground state is called spontaneous symmetry breaking. Breaking the gauge symmetry (albeit in a way that leaves the Lagrangian invariant) allows us to have mass terms. After spontaneous symmetry breaking, the photon remains massless since the electromagnetic gauge symmetry has not been spontaneously broken, and the weak gauge bosons are found to acquire mass.

2.3 Beyond the SM

The weak coupling constant g in the vertex factors for neutral and charged weak current interactions can be defined in terms of the masses of the weak exchange bosons Z and $W^\pm$ as

$$g^2 = \frac{8G_F M_W^2}{\sqrt{2}} = \frac{8G_F M_Z^2 \cos^2\theta_W}{\sqrt{2}}, \tag{2.19}$$

where G_F is the Fermi constant. The relevant SM parameter, here, is the weak mixing angle $\sin^2\theta_W$. In the electroweak theory, g is linked to the electromagnetic charge by $e = g\sin\theta_W$, Eq. (2.12).

In regards to the experimentally precision extraction, a renormalised definition of the $\sin^2\theta_W$ is required. The on-shell scheme [23–26] renormalised definition of $\sin^2\theta_W$ at tree level is given by

$$\sin^2\theta_W = 1 - \frac{M_W^2}{M_Z^2}, \tag{2.20}$$

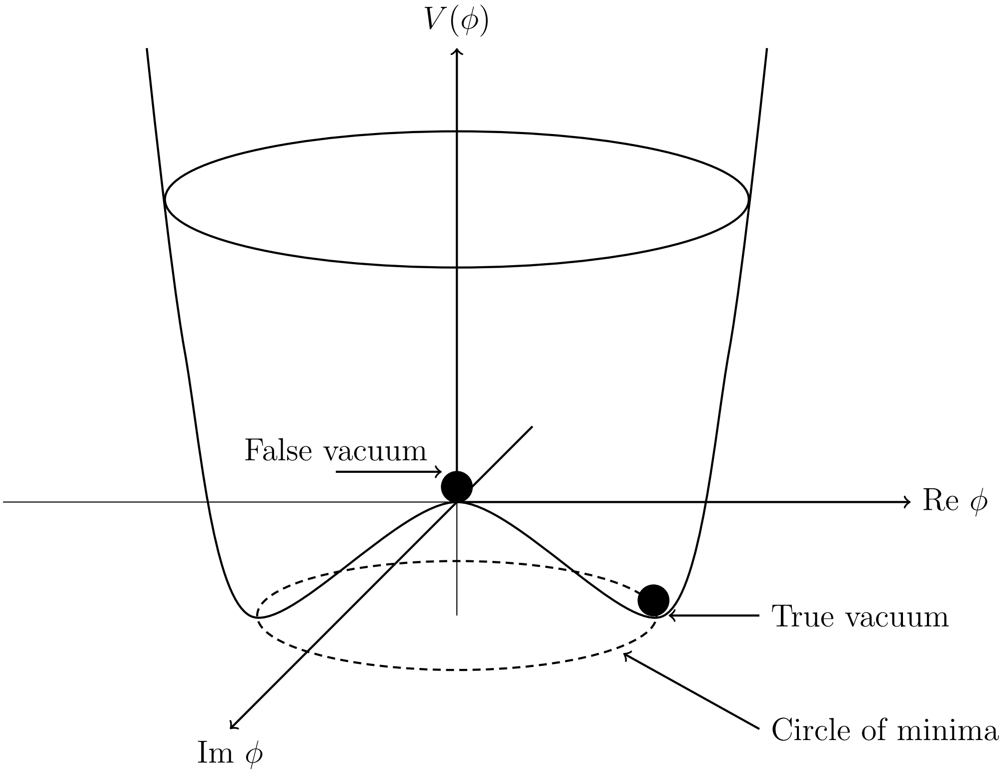

Figure 2.2: Higgs mechanism and the potential $V(\phi)$, Eq. (2.17), for negative value of μ^2.

and this definition was used broadly at an early stage. Due to finding that the top quark mass m_t is large, the above renormalised expression became largely unfavoured because its use induced misleading radiative corrections, which means that an alternative expression is required [9]. Currently, the most popularly used expression of the weak mixing angle is derived from the modified minimal subtraction ($\overline{\mathrm{MS}}$) renormalisation scheme [27] and is given by

$$\sin^2\theta_W(\mu)_{\overline{\mathrm{MS}}} = e^2(\mu)_{\overline{\mathrm{MS}}}/g^2(\mu)_{\overline{\mathrm{MS}}}, \tag{2.21}$$

where μ is an arbitrary energy scale and given by $\mu = \sqrt{|q^2|} \equiv Q$, where q^2 is the four-momentum transfer squared. As strong coupling $\alpha_s(Q)$ exhibits a running with respect to the energy, so does $\sin^2\theta_W$ as shown in Fig. 2.3.

Precision measurements can be used as Standard Model tests, where a detected disagreement with the SM prediction will signify the signs of physics beyond the SM. The Q_{weak} experiment [4], which did determine the proton's weak charge, Q_W^p, to a precision of 6%, is suitable for probing mass scales of new physics in the TeV range.

In addition to the Q_{weak} experiment, previous parity-violating electron scattering

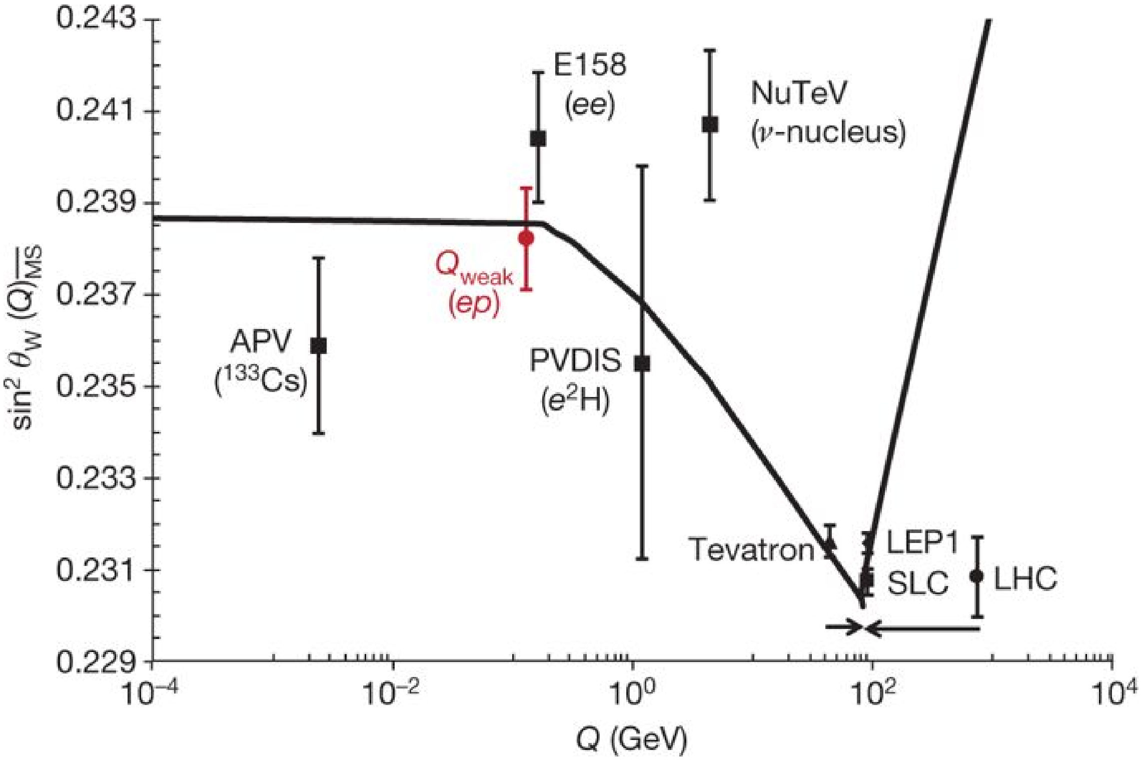

Figure 2.3: The running of $\sin^2\theta_W$ with respect to the energy scale Q in the $\overline{\text{MS}}$ renormalisation scheme [28]. This plot is adapted from [4].

(PVES) experiments, which are defined formally in Chapter 5, may be used to place constraints on new physics beyond the Standard Model [29] and to reduce hadronic structure uncertainties that are related to the knowledge of the strange quark and the axial form factors contributions.

The Q_{weak} experiment involves the interaction of electrons and the valence quarks in the proton. The effective low-energy Lagrangian that characterises the virtual-exchange of a Z^0-boson can be expressed as [30]

$$\mathcal{L}_{NC}^{eq} = -\frac{G_F}{\sqrt{2}}\bar{e}\gamma_\mu\gamma_5 e\sum_q C_{1q}\bar{q}\gamma^\mu q, \tag{2.22}$$

where C_{1q} are the weak vector coupling constants. The parity-violating part of the Lagrangian can be defined as a combination of the Standard Model Lagrangian and a Lagrangian for new physics [30]:

$$\mathcal{L}_{NC}^{eq} = -\frac{G_F}{\sqrt{2}}\bar{e}\gamma_\mu\gamma_5 e\sum_q C_{1q}\bar{q}\gamma^\mu q + \frac{g^2}{4\Lambda^2}\bar{e}\gamma_\mu\gamma_5 e\sum_q h_V^q\bar{q}\gamma^\mu q, \tag{2.23}$$

where Λ, g and h_V^q are the mass scale, the coupling constant and effective coefficients related to the new physics, respectively. The precise measurements obtained by

Q_{weak} collaboration put considerable constraints on many new physics scenarios, i.e., more precise the measurement of the proton's weak charge means more significant constraints on new physics.

Assuming the 95%-confidence-level, the sensitivity to the mass scale of new physics in terms of Q_W^p and its uncertainty $\pm\Delta Q_W^p$ can be expressed as [4]

$$\frac{\Lambda_\pm}{g} = \nu\sqrt{\frac{4\sqrt{5}}{|Q_W^p \pm 1.96\Delta Q_W^p - Q_W^p(SM)|}}, \tag{2.24}$$

where $\nu^2 = \sqrt{2}/(2G_F)$, Λ is the mass reach for new physics and 1.96 indicates that a 95%-confidence-level was chosen. The sensitivity to the mass scale can be expressed as a function of the possible range of the flavour mixing angle, θ_h, of the new physics with setting the isospin dependence by $h_V^u = \cos\theta_h$ and $h_V^d = \sin\theta_h$.

The Q_{weak} result, where the most precise and smallest asymmetry measurement was obtained, put considerable constraints on wide range of search of new physics beyond the SM. For example, the Q_{weak}'s measurements put considerable limits on the studies of leptoquarks (hypothetical particles that can change quarks into leptons and vice-versa). Furthermore, this result is sensitive to searches for an additional neutral gauge bosons (Z') and different supersymmetric models. Moreover, the information extracted from this experiment may serve as a test to identify new physics that could be found in the future at the Large Hadron Collider (LHC).

In addition to the usefulness of PVES as a tool to probe new physics beyond the SM, this technique can be used to provide precise information about nucleon structure. Particularly, it places tight constraints on the size of the strange quark contribution which is difficult to predict theoretically. Theoretical estimations for the strangeness contribution to the nucleon electromagnetic form factors can be done using some approaches, for example, chiral perturbation theory (ChPT), dispersion relations, vector meson dominance (VMD) and lattice quantum chromodynamics (LQCD). However, these estimations, as reviewed briefly in Chapter 4, widely vary.

In this work, a complete global analysis of all PVES asymmetry data, up to the currently available limit of $Q^2 \sim 1\text{GeV}^2$, for the proton, ^{4}He and deuteron is presented. A considerable remaining source of systematic uncertainty in the experimental measurements of the strangeness form factors of the proton is the assumption that charge symmetry violation (CSV) is negligible. As the CSV effects have not been throughly quantified, several theoretical predictions of CSV [31–35] in the proton's electromagnetic (EM) form factors are taken into account in the current work.

It is appropriate that the next chapter be dedicated to highlighting the role of strangeness in nucleon structure. In particular, it will present a relevant perspective for studying the content of the strange quark-antiquark pairs of the neutral weak form factors.

Chapter 3

The Strangeness in the Nucleon

The first hint that the proton has a nontrivial structure occurred when Frisch and Stern[1] conducted a measurement of the proton's magnetic moment μ_p [36, 37]. Their results showed the μ_p to be more than one nuclear magneton (μ_N), $\sim 2.5\mu_N$. Then, in 1940, Alvarez and Bloch made a first direct measurement of the neutron's magnetic moment and was found to be $\sim -1.93(2)\mu_N$ [38]. These findings violated the assumption at the time that the proton and neutron are elementary particles.

In the late 1960s, deep inelastic scattering (DIS) experiments conducted at Stanford Linear Accelerator Center (SLAC) confirmed that the nucleon is composed of point-like Dirac particles (quarks). Soon after, quantum chromodynamics (QCD) was developed to describe the interaction between these quarks by introducing a gauge colour force between quarks.

The modern description of the proton is that it is composed of three valence quarks, i.e., two up quarks and a down quark, that are held together by the strong force. The valence quarks are surrounded by virtual QCD vacuum-generated quark-antiquark pairs that emerge and annihilate in the quark-gluon sea inside the proton. There is no constraint on the quark flavours of the sea quarks, however, the lightest quark pairs ($u\overline{u}$, $d\overline{d}$ and $s\overline{s}$) are most likely to exist within the sea quarks. Hence, the strange quark contribution to the proton properties derives from the sea quarks. Fig. 3.1 illustrates this description for proton structure.

Although the net strangeness, which is a quantum number that was independently proposed in the 1950's by Gell-Mann[2] and Nishijima [39–41], of the nucleon is zero, the s quarks could still have a space-time distribution inside the nucleon.

At high momentum transfers, where the theory is perturbative, QCD can de-

---

[1] Stern was awarded the 1943 Nobel prize for the first measurement for the proton's magnetic moment, μ_p.

[2] Gell-Mann received the 1969 Nobel Prize in physics for his work on the classification of elementary particles and their associated interactions.

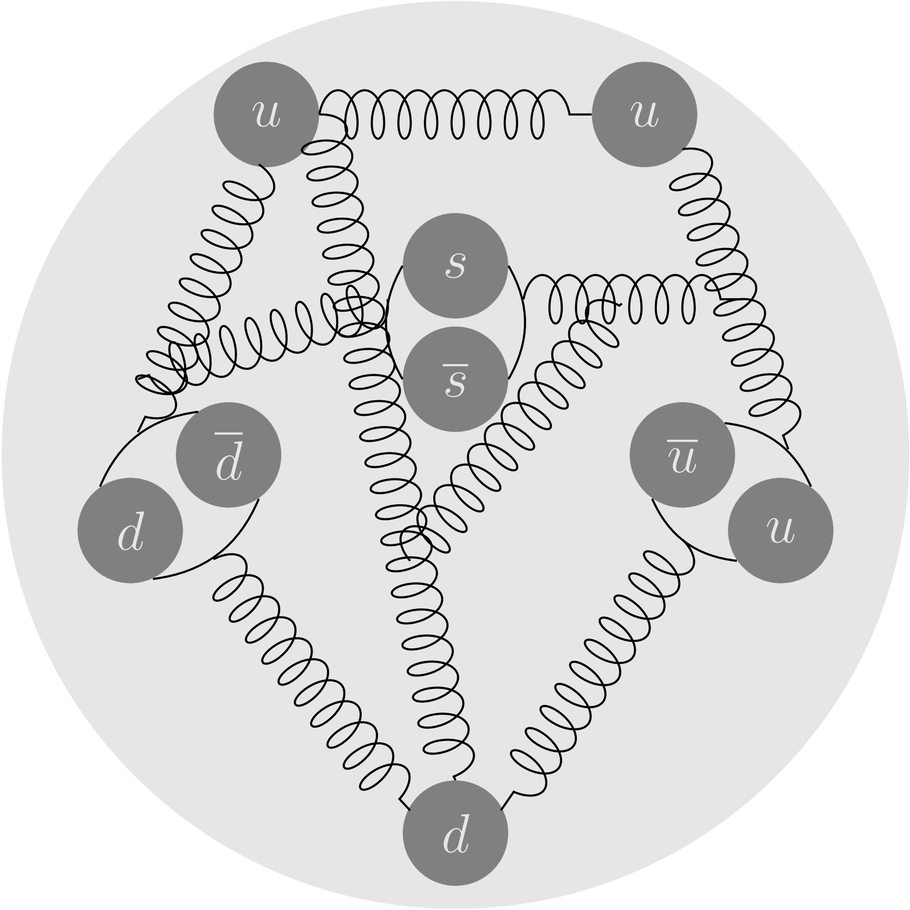

Figure 3.1: The proton's internal structure.

scribe the strong interaction and hadronic phenomena. However, at low momentum transfers, where the theory is nonperturbative, the situation is more complicated due to the large coupling constant α_s in this momentum region (it is of the order of unity at low energy).

Most of the observations that have been made are restricted to the proton because the free neutron does not exist in nature. On account of this fact, the strangeness in the proton will be briefly highlighted in the next sections in order to present the appropriate viewpoint for discussion of the strange quark-antiquark pairs $\overline{s}s$ content in the nucleon through the parity-violating (PV) electron scattering method described in Chapter 5.

3.1 Strangeness in the Nucleon Mass

The contribution of the strange quark to the nucleon mass is characterised by the strange quark sigma term, σ_s.

Sigma terms are, in general, given by the matrix elements of the scalar quark currents $\overline{q}q$ between nucleon states. Therefore, the σ_s and σ_l terms can be defined as [42]

$$\begin{aligned}\sigma_s &= m_s\big\langle N|\overline{s}s|N\big\rangle,\\ \sigma_l &= m_l\big\langle N|\overline{u}u+\overline{d}d|N\big\rangle,\end{aligned}\tag{3.1}$$

where σ_l is the light quark sigma term, $m_l = (m_u + m_d)/2$ is the average up and down quark mass and m_s is the strange quark mass.

The strange nucleon sigma term σ_s has traditionally been poorly determined. Phenomenologically, the determination of σ_s reveals a wide range of values, which indicates that the strange quark contribution is between 0 and more than 30% of the nucleon mass [43]. It is generally calculated from the small difference between σ_l and the non-singlet combination σ_0. The σ_0 can be written as

$$\sigma_0 = m_l\big\langle N|\overline{u}u+\overline{d}d-2\overline{s}s|N\big\rangle.\tag{3.2}$$

The σ_l can be derived from π-N scattering using dispersion calculation [44, 45] and the σ_s can be determined from the physically observed baryon mass spectrum. The preceding sigma terms are connected with each other by the relation

$$\sigma_s = \frac{m_s}{2m_l}(\sigma_l - \sigma_0).\tag{3.3}$$

Most commonly, one can define the y-parameter to represent the strangeness content of the nucleon as

$$y = \frac{2\big\langle N|\overline{s}s|N\big\rangle}{\big\langle N|\overline{u}u+\overline{d}d|N\big\rangle} = \frac{2m_l\sigma_s}{m_s\sigma_l}.\tag{3.4}$$

In addition to characterising the purely sea quark content of the nucleon, this parameter plays an important role in dark matter detection rates, which depend sensitively on the nucleon scalar matrix elements.

The determination of σ_s is remarkably sensitive to the difference between σ_l and σ_0, Eq. (3.3). A recent and comprehensive analysis that is based on the Roy-Steiner equations for πN scattering obtained a value of $\sigma_l = 59.1 \pm 3.5$ MeV [46]. Given the considerable uncertainty of the value of σ_s extracted from σ_l due to the experimental uncertainties and variance of the πN scattering data, the limited precision of higher-order chiral corrections to the hyperon mass and the uncertainty associated with the quark mass ratio, the extrapolation of the data to the unphysical region (Cheng-Dashen points), there is a notable scope for lattice QCD to present a significant constraint on sigma terms. In recent years, several lattice QCD studies, e.g., [47–53], have been conducted to determine the sigma terms. Within the framework of lattice QCD, two methods are employed to determine these sigma terms. The first is a direct measurement of the scalar matrix elements by 3-point function methods (direct method). The second extracts the sigma terms through the use of the Feynman-Hellmann theorem (spectrum method).

In the first method, relevant ratios of 3-point and 2-point correlation functions are constructed to extract the required matrix elements. The construction of the correlation functions requires two different forms of Wick contraction. In particular, as shown in Fig. 3.2, there are contributions from quark-line connected and disconnected operator insertions for up and down quarks and only disconnected insertion for strange quarks. The disconnected contributions, which require 'all-to-all' quark propagators to be calculated, are extremely challenging and this is especially important for the strange quark contributions in the nucleon [54–56].

Instead of the direct 3-point method, one can consider the Feynman-Hellman theorem [57, 58] which relates the nucleon scalar matrix elements to the dependence of the nucleon mass on the quark masses via the equations

$$\sigma_l = m_l \langle N|\overline{u}u + \overline{d}d|N\rangle = m_l \frac{\partial M_N}{\partial m_l}, \tag{3.5}$$

$$\sigma_s = m_s \langle N|\overline{s}s|N\rangle = m_s \frac{\partial M_N}{\partial m_s}. \tag{3.6}$$

The Gell-Mann-Oakes-Renner (GOR) relation [59] is usually invoked such that M_N is defined as a function of the squares of meson masses. Therefore, the derivatives are expected to be evaluated at the quark mass values that correspond to the physical pion and kaon masses:

$$\sigma_l = m_\pi^2 \frac{\partial M_N}{\partial m_\pi^2}, \tag{3.7}$$

$$\sigma_s = \bar{m}_K^2 \frac{\partial M_N}{\partial \bar{m}_K^2}, \tag{3.8}$$

where $\bar{m}_K^2 = m_K^2 - m_\pi^2/2$. The difficulty associated with this approach is that a number of simulations at different values of the light and strange quark masses are required in order to evaluate the derivative.

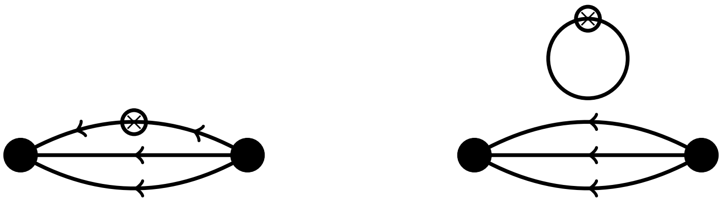

Figure 3.2: Feynman diagrams of connected (left) and disconnected (right) operator insertions that contribute to the nucleon 3-point function.

3.2 Axial Matrix Element and Strangeness in the Nucleon Spin

In the quark-parton model (QPM), the spin-dependent structure function $g_1(x, Q^2)$ in terms of the spin-dependent quark distributions $\Delta q(x, Q^2)$ is defined as

$$g_1(x, Q^2) = \frac{1}{2}\sum_q e_q^2 \Delta q(x, Q^2), \tag{3.9}$$

where e_q are the electric charges of the quarks introduced in Table 2.2 and

$$\Delta q(x, Q^2) = q^+(x, Q^2) - q^-(x, Q^2) + \overline{q}^+(x, Q^2) - \overline{q}^-(x, Q^2). \tag{3.10}$$

The squared four-momentum transfer Q^2 can be suppressed since g_1 exhibits an approximate independence of Q^2 and depends only on the Bjorken variable x in high-Q^2 DIS.

For a polarised nucleon, $q^{+(-)}(x)$ reflects the number density of the quark of flavour q with the superscript $+$ $(-)$ reflecting that the quark's polarisation is parallel (anti-parallel) to that of the nucleon, and x is the fraction of the momentum of the proton carried by the quark in the infinite momentum frame. The total contribution of the quark and anti-quark of flavour q to the spin of the nucleon is

$$\Delta q = \int_0^1 \Delta q(x) dx. \tag{3.11}$$

Δq is related to the matrix element of the axial current of the nucleon.

Within the framework of the non-relativistic quark model, which was independently pioneered by Zweig [60] and Gell-Mann [61], the spin of the nucleon is entirely attributed to the quarks.

An experimental constraint can be implemented on Δu, Δd and Δs. There are several measurements of spin asymmetry in DIS of longitudinally polarised muons by longitudinally polarised nucleons, in which the cross section is described by the structure function $g_2(x)$ in addition to $g_1(x)$. In this regard, there are a number of experiments that have been conducted at, for example, SLAC [62, 63], in which a primary concern in measuring $g_1(x)$ was to study the Ellis-Jaffe [64] and Bjorken sum rules [65, 66].

To the first moment, working with the three lightest quark flavours, the Ellis-Jaffe sum rule can be defined as [67]

$$\Gamma_1 = \int_0^1 g_1(x)dx = \frac{1}{2}\Big[\frac{4}{9}\Delta u + \frac{1}{9}\Delta d + \frac{1}{9}\Delta s\Big]. \tag{3.12}$$

Rewriting Eq. (3.11) in terms the $SU(3)_f$ nucleon axial charges, i.e.,

$$\begin{aligned} a_3 &= \Delta u - \Delta d, \\ a_8 &= \Delta u + \Delta d - 2\Delta s, \\ a_0 &= \Delta u + \Delta d + \Delta s, \end{aligned} \tag{3.13}$$

leads to

$$\Gamma_1 = \frac{3}{36}a_3 + \frac{1}{36}a_8 + \frac{4}{36}a_0, \tag{3.14}$$

where a_3, a_8 and a_0 are isovector, octet and singlet combinations, respectively. To evaluate Γ_1 for the proton (Γ_1^p), the value of $a_3 = -g_A/g_V = 1.2723 \pm 0.0023$, which describes the ratio of axial-vector g_A to vector g_V couplings in neutron β-decay, is used [15]. In addition, the assumption that the strange quark contribution is zero ($\Delta s = 0$) resolves the difficulties associated with a_0, which has not been determined experimentally. In this case, one has $a_0 = a_8$. The value of $a_8 = 0.58 \pm 0.03$ is determined from the best fit to Λp, $\Xi\Lambda$ and Σn hyperon β-decays [15], with an assumption of $SU(3)$ flavour symmetry, i.e., assuming only three lightest quark flavours, u, d and s. Therefore, for the Ellis-Jaffe sum rule for the proton one obtains

$$\Gamma_1^p = \int_0^1 g_1^p(x)dx = 0.187 \pm 0.003. \tag{3.15}$$

The Ellis-Jaffe sum for the neutron (Γ_1^n) can be evaluated by changing the sign of the isovector term a_3:

$$\Gamma_1^n = \int_0^1 g_1^n(x)dx = -0.025 \pm 0.003. \tag{3.16}$$

Assuming $SU(3)$ flavour symmetry, the isovector and octet combinations, a_3 and a_8, respectively, can be used to describe the octet baryon β-decay parameters F and D

as

$$\begin{aligned} a_3 &= F + D, \\ a_8 &= 3F - D. \end{aligned} \tag{3.17}$$

The Bjorken sum rule implies an additional constraint on Δu and Δd as [66]

$$\int_0^1 \Big[g_1^p(x) - g_1^n(x) \Big] dx = \frac{1}{6}(\Delta u - \Delta d) = \frac{1}{6} a_3. \tag{3.18}$$

The Ellis-Jaffe and Bjorken sum rules need to be modified in order to account for QCD radiative corrections that have been estimated up to order $\alpha_s^3(Q^2)$, e.g., see [68, 69]. The next-to-leading order (NLO) QCD approximation to the Ellis-Jaffe sum rule for the proton, Γ_1^p, can be written as [67]

$$\Gamma_1^p = \frac{3}{36} a_3 \left[1 - \frac{\alpha_s(Q^2)}{\pi} \right] + \frac{5}{36} a_8 \left[1 - \frac{7}{15} \frac{\alpha_s(Q^2)}{\pi} \right]. \tag{3.19}$$

Physicists have been puzzled since the discovery by European Muon Collaboration (EMC) [70], in which the spin-dependent structure function $g_1(x)$ for the proton was determined and found to be in disagreement with the Ellis-Jaffe sum rule. This determination showed that the quarks are responsible for a relatively small fraction of the spin of the proton and also that Δs is small and negative. This discovery conflicts with the quark model and this issue is known as the 'proton spin crisis'.

In practice, comparisons of these predictions of Γ_1 with experiments are model-dependent for many reasons. To calculate the integrals of $g_1(x)$ over the full x ranges, the data need to be extrapolated to $x = 1$ and $x = 0$. For large x, the $g_1(x)$ structure function approaches zero as x tends to 1. However, there are difficulties at low x related to model dependence [71]. Furthermore, including the NLO QCD corrections to Γ_1 leads to propagating uncertainties in the evaluation of g_1 with the four-momentum transfer Q^2, where $g_1(x)$ has a significant Q^2-dependence because of QCD corrections. The QCD evolution of the gluon contribution to the Ellis-Jaffe sum rule also cannot be estimated unambiguously [67]. Moreover, regarding a_8, the assumption of $SU(3)$ flavour symmetry is violated in the nature. In spite of these difficulties, majority of the NLO calculations conclude with a negative and small value for Δs, e.g., see [72, 73].

The contribution of Δs to PVES is suppressed by the weak charge of the electron. However, Δs is not suppressed in elastic neutrino-nucleon scattering. Fits to neutrino-proton scattering cross section data found that Δs is compatible with the result from DIS [74, 75]. Global fits of parity-violating elastic electron-proton scattering data combined with ν–p and $\overline{\nu}$–p scattering data suggest that Δs is negative [76, 77] in agreement with DIS.

The proton spin puzzle still exists today, and recent quantitative estimations of the quarks' contribution to the proton's spin are about 30% [78–80]. The orbital angular momentum of the quarks inside the proton is anticipated to play an important role in solving this puzzle as discussed in [81]. The authors of [82] reported the first lattice QCD calculation of the gluon spin in the nucleon. Their estimations indicate that the gluon significantly contributes to the proton's spin.

3.3 Strangeness in the Nucleon's Momentum

The Neutrinos at the Tevatron (NuTeV) collaboration measured the fraction of the nucleon momentum carried by the strange sea to the fraction of the momentum carried by the non-strange sea using data from experiments conducted at the Fermi National Accelerator Laboratory. The data were obtained via deep inelastic neutrino-nucleon scattering, which is depicted in Fig. 3.3 [83, 84]. Based on these data, the NuTeV collaboration measured the ratio k_s,

$$k_s = \frac{\int_0^1 x[s(x,Q^2) + \overline{s}(x,Q^2)]dx}{\int_0^1 x[\overline{u}(x,Q^2) + \overline{d}(x,Q^2)]dx}, \tag{3.20}$$

and found $k_s = 0.42 \pm 0.07(\text{stat}) \pm 0.06(\text{sys})$ at Q^2=16 GeV^2 [86]. This result reflects the existence of the strange quark in the nucleon's sea. However, it is difficult to relate this result to the static properties of the nucleon [85].

Similar several experiments have been conducted, e.g., CDHS [87], Columbia-Chicago-Fermilab-Rochester (CCFR) [88, 89], CHARMII [90], NOMAD [91, 92] NuTeV [93–96] and CHORUS [97, 98] collaborations, and reported relatively small values of k_s compared with a recent measured value of $k_s = 1.13^{+0.08}_{-0.13}$ at $x = 0.023$ and $Q^2 = 1.9$ GeV^2 [99].

Beside the previous ratio k_s, there is another relevant quantity,

$$\eta_s = \frac{\int_0^1 x[s(x,Q^2) + \overline{s}(x,Q^2)]dx}{\int_0^1 x[u(x,Q^2) + d(x,Q^2)]dx}, \tag{3.21}$$

which describes the momentum fraction ratio of the strange quark to the total non-strange quark content, and its values range from 5% to 10%.

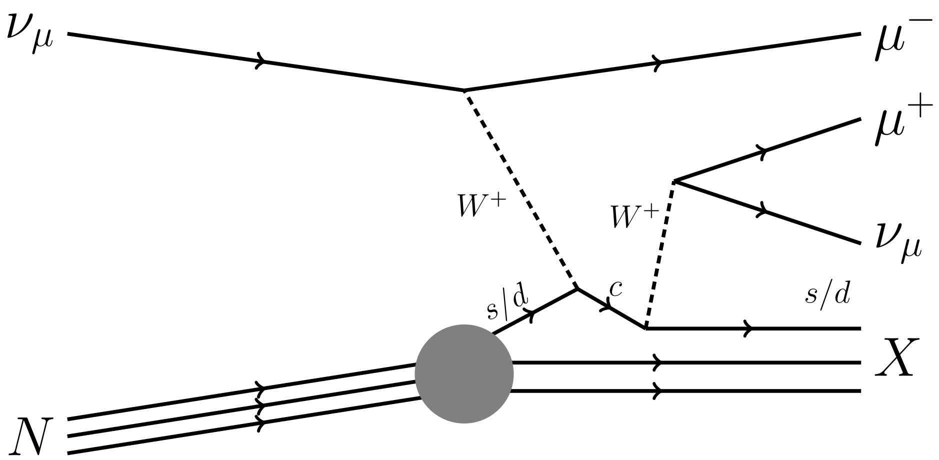

Figure 3.3: Neutrino-nucleon charged current deep inelastic scattering. The neutrinos ν_μ interact with strange quark s to produce a negative muon μ^- and a charm quark c, and the c quark subsequently decay to produce a positive muon μ^+, yielding dimuon pairs $(\mu^+\mu^-)$ [85].

3.4 Strange Vector Matrix Elements

The strange quark contribution to the nucleon EM form factors is encoded in the strange vector matrix element $\langle N|\bar{s}\gamma^\mu s|N\rangle$.

In 1988, Kaplan and Manohar [1] proposed that the strange electric and magnetic form factors contributions, G_E^s and G_M^s, respectively, can be accessed by measurements of the neutral weak current matrix elements in neutrino-nucleon scattering. Shortly after, in 1989, McKeown [2] and Beck [3] suggested an experimental study to measure the weak neutral current of the proton using parity-violating electron scattering in order to determine the strange quark contribution to the vector matrix elements. This method generated significant interest within the community and was followed by more than two decades of experimental investigations. This thesis is devoted to such a method to study the strange quark contribution to the proton's EM form factors.

The theoretical predictions of the strangeness form factors will be reviewed in Chapter 4. The parity-violating electron scattering method and the main experimental programs that consider this method will be presented in Chapter 5.

Chapter 4

Theoretical Prediction of G_E^s and G_M^s

As discussed in the previous chapter, the calculation of the static properties of the nucleon in QCD is a challenging task. This can be attributed to the fact that the strong coupling constant, α_s, is large at low energies. This means that using a perturbative expansion is not possible to to characterise the interaction in power series of α_s. Because of the difficulty of directly calculating the strange quark contribution to the properties of the nucleon, one needs to consider other approaches in which controlled rough estimations can be achieved.

There are two quantities that are frequently considered to describe the behaviour of electric and magnetic strange quark form factors, $G_E^s(Q^2)$ and $G_M^s(Q^2)$, respectively, at zero momentum transfer ($Q^2 = 0$); the strange charge mean square radius $\left\langle r_s^2 \right\rangle_E$ and the strange magnetic moment $\mu_s = G_M^s(Q^2 = 0)$. The electromagnetic form factor provides information about the spatial distribution of the charge and magnetisation within the nucleon, and this distribution helps us to learn the spatial dimension of the hadrons.

The strange quark contribution to the electric form factor at zero Q^2 is constrained to be zero as there is no net strangeness in the nucleon. Most models are devoted to investigate the contribution to the strange magnetic moment and the strangeness radius. Furthermore, the Q^2-dependence of the EM strange form factors has been examined by several theoretical methods.

A survey of the most popular theoretical studies is presented below. For easy comparison, different theoretical predictions of μ_s and $\left\langle r_s^2 \right\rangle_E$ are summarised in Table 4.1 at the end of this chapter.

4.1 Theoretical Prediction of G_E^s and G_M^s

According to Steven Weinberg [100], the Goldstone bosons[1] are weakly interacting fields, and the loop effects are suppressed by inverse powers of the chiral symmetry breaking scale $\Lambda_\chi \sim 1$ GeV associated with the power series in momentum p that fulfils $p \ll \Lambda_\chi$. $\Lambda_\chi = 4\pi f_\pi$, where f_π is the pion decay constant. Consequently, at low energy, the effective interaction between the Goldstone bosons can be described perturbatively. This technique was developed by Gasser and Leutwyler [42, 101] leading to ChPT.

Extension of the meson sector effective calculation to include the nucleon is associated with a difficulty. The nucleon mass M_N does not vanish in the chiral limit and its value is very similar to the chiral symmetry breaking scale Λ_χ. This means that the nucleon mass destroys the idea of a perturbative scheme because higher-derivative terms which involve the nucleon field are not suppressed, i.e, $M_N/\Lambda_\chi \sim 1$. To deal with this difficulty, Jenkins and Manohar introduced a formalism in which the nucleon is treated as a heavy static fermion so that the M_N dependence can be absorbed into a series of interaction vertices (moving the M_N dependence from the propagator to the vertices) with increasing power of the inverse nucleon mass [102]. This formalism provided the so-called heavy baryon chiral perturbation theory (BChPT).

In this section, various theoretical approaches to describe the strangeness of the nucleon are highlighted. The survey below is by no means complete, but it provides the most critical and widespread of several physical pictures and their results. The reader can refer to [85, 103, 104] for general reviews on the theoretical predictions for the nucleon's strange vector form factors.

4.1.1 Heavy Baryon Chiral Perturbation Theory (BChPT)

Extension of the BChPT from $SU(2)$ to $SU(3)$ needs to be considered to calculate the strange quark contributions. Introducing K loops leads to additional phenomenological counterterms.

A number of these counterterms are fit to the experimentally measured baryon octet magnetic moments. However, two flavour-singlet channel counterterms are still unknown. These two counterterms are related to the strangeness magnetic moment and radius. Therefore, the BChPT is not able to determine the strangeness content

---

[1] Goldstone bosons are massless and spinless particles associated with the models that exhibit spontaneous symmetry breaking of global symmetries in quantum field theory. They are occasionally called Nambu-Goldstone bosons.

of the nucleon [103].

Hammer *et al.* analysed the Q^2-dependence of G_M^s up to fourth order in the chiral expansion $\mathcal{O}(p^4)$ and argued that there is a significant cancellation between loop contributions from $\mathcal{O}(p^3)$ and $\mathcal{O}(p^4)$, which means that the Q^2 slope of the G_M^s displays an enhanced sensitivity to an unknown $\mathcal{O}(p^4)$ counterterm [105]. Therefore, with this issue, one needs to request additional model-dependent assumptions to estimate the size of the chiral counterterms in order to present predictions for the strange vector form factors of the nucleon.

4.1.2 Vector Meson Dominance (VMD)

The vector meson dominance (VMD) model was proposed before the introduction of QCD to describe photon-hadron interactions [106–108]. In the VMD model, the photon can fluctuate into an intermediate vector meson, which finally interacts with the hadron. This interaction is schematically illustrated by the Feynman diagram in Fig. 4.1. Explicitly, the matrix element of the electromagnetic current between any hadronic states $|A\rangle$ and $|B\rangle$ at a squared four-momentum transfer, q^2, in the vector meson resonances region can be written as a summation over intermediate vector states V as [67]

$$\langle B|J_\mu^{EM}|A\rangle = \sum_V \frac{f_V}{(m_V^2 - q^2 - i\Gamma_V m_V)} \langle B|V_\mu|A\rangle, \tag{4.1}$$

where m_V and Γ_V are the mass and the decay width of the vector meson V. $f_V = m_V^2/g_V$ is the vector-meson-photon coupling constant, where g_V is a constant related to the physical vector meson mass. $\langle B|V_\mu|A\rangle$ reflects the strength for the coupling of the meson V to the state $|A\rangle$ as it experiences a transition to the state $|B\rangle$.

The electromagnetic current defined in Eq. (2.15), for the three lightest quarks (u, d and s), can be written as a sum of the electromagnetic current of the three lightest vector mesons (ρ, ω and ϕ) as

$$J_\mu^{EM} = \frac{1}{\sqrt{2}} J_\mu^{(\rho)} + \frac{1}{3\sqrt{2}} J_\mu^{(\omega)} - \frac{1}{3} J_\mu^{(\phi)}, \tag{4.2}$$

where $J_\mu^{(V=\rho,\omega,\phi)}$ are the vector meson V electromagnetic currents.

f_V in Eq. (4.1) describes how much the physical state of the vector meson overlaps with the quark-antiquark pairs created by the electromagnetic current operator when

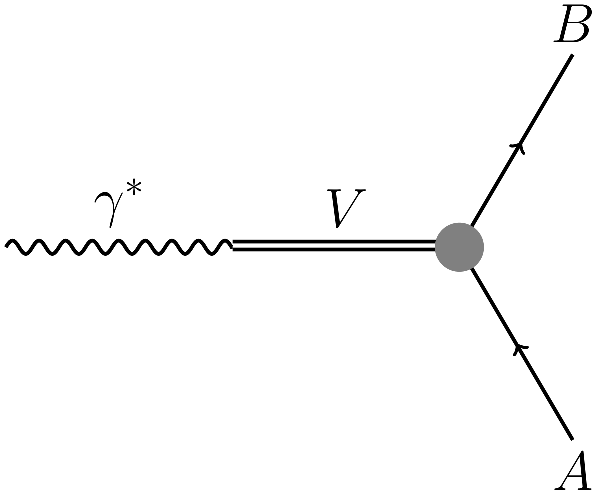

Figure 4.1: The illustrative Feynman diagram of the vector meson dominance model. γ^* is a space-like photon ($q^2 < 0$) fluctuating into an intermediate vector meson V. A and B are the initial and final states of the hadron, respectively.

applied to the vacuum state $|0\rangle$ [67]:

$$\begin{aligned}
\langle\rho|J_\mu^{EM}|0\rangle &= \frac{1}{\sqrt{2}}\langle\rho|J_\mu^{(\rho)}|0\rangle = f_\rho\epsilon_\mu, \\
\langle\omega|J_\mu^{EM}|0\rangle &= \frac{1}{3\sqrt{2}}\langle\omega|J_\mu^{(\omega)}|0\rangle = f_\omega\epsilon_\mu, \\
\langle\phi|J_\mu^{EM}|0\rangle &= -\frac{1}{3}\langle\phi|J_\mu^{(\phi)}|0\rangle = -f_\phi\epsilon_\mu,
\end{aligned} \tag{4.3}$$

where ϵ_μ are polarisation vectors of the vector meson .

From the quark composition of the vector mesons, one notes that ρ is an isovector meson, whereas ω and ϕ are isoscalars. The isoscalar ($I = 0$) and isovector ($I = 1$) nucleon form factors written in terms of the combinations of the Dirac $F_1^{p,n}$ and Pauli $F_2^{p,n}$ form factors of the proton and neutron are considered[2]

$$\begin{aligned}
F_{1,2}^{I=0}(q^2) &= \frac{F_{1,2}^p(q^2) + F_{1,2}^n(q^2)}{2}, \\
F_{1,2}^{I=1}(q^2) &= \frac{F_{1,2}^p(q^2) - F_{1,2}^n(q^2)}{2}.
\end{aligned} \tag{4.4}$$

$F_i(q^2)$, for $i = 1,\ 2$, can be written as [109]

$$F_i(q^2) = \sum_V \frac{a_i^V}{m_V^2 - q^2}, \tag{4.5}$$

---

[2] Instead of considering the protons and neutrons, it is common to use their isospin symmetry properties (see Appendix A).

where $a_i^V = f_V g_i^{VNN}$ is the pole residual. g^{VNN} denotes the coupling of the meson V to the nucleon. $F_i(q^2)$ is the approximated form of the dispersion relation:[3]

$$F_i(q^2) = F_i(0) + \frac{q^2}{\pi} \int_{t_0}^{\infty} \frac{\Im m\ F_i(t)}{t(t - q^2 - i\epsilon)}\, dt, \tag{4.6}$$

with the spectral functions $\Im m\ F_i(t)$ written as

$$\Im m\ F_i(t) = \pi \sum_V a_i^V \delta(t - m_V^2). \tag{4.7}$$

The lower limit of integration, t_0, is provided by the threshold of the lightest possible intermediate state that contributes to the form factors. The lightest possible hadronic intermediate state in the case of the isoscalar form factor is a system of three pions (rather than two in the case of the isovector form factor) as long as the small isospin breaking effect is neglected [67]. Hence, t_0 is $9m_\pi^2$ and $4m_\pi^2$ for the isoscalar and isovector form factors, respectively.

Within the framework of the vector meson dominance model, Hohler *et al.* [109] have done a global fit of the electron-nucleon elastic cross section. They performed a three-pole fit to both the isovector and isoscalar form factors. They fixed the second isoscalar pole at ϕ mass and used the third pole to reflect the contributions from higher resonances. In that analysis, Hohler *et al.* obtained a large value for ϕNN coupling, and this value suggests a large strangeness content of the nucleon. This result violates the OZI rule of the disconnected quark lines [110][4]. Hohler *et al.* result was supported by Jaffe who concluded that $\mu_s = -0.31 \pm 0.09\ \mu_N$ and $\langle r_s^2 \rangle_E \sim 0.14 \pm 0.09\ \text{fm}^2$ [111]. Jaffe indicated that these results are sensitive to the value of the small mixing angle, ϵ, between ω and ϕ.

Forkel [112] updated Jaffe's minimal 3-pole ansatz and then extended the pole approximation to implement the asymptotic QCD momentum dependence and found that the size of the 3-pole results reduced by about a factor of 2.5.

Although the results from different VMD studies are consistent with each other, the model-dependence in such studies should be taken into account.

---

[3] The subtracted form is used here instead of the unsubtracted one (see Appendix A). The dispersion relations approach will be revisited in Section 4.1.6.

[4] The OZI rule states that the contribution of the disconnected quark lines is suppressed. The large value of ϕNN indicates that the OZI rule is violated where the ϕ meson is made of $s\bar{s}$, which is disconnected from the u and d quarks in the nucleon.

4.1.3 Kaon Loop

A different model to predict the nucleon's strangeness form factors will be briefly highlighted in this subsection. This model does not require consistency of chiral expansion and includes a kaon loop contribution [104, 113–116]. Such an approach is called kaon loop model in which the proton can fluctuate into a K (the lightest strange meson) and a hyperon Λ, then the $s\bar{s}$ quarks annihilate leaving the original proton. The strangeness of the proton is characterised by the $K^+\Lambda^0$ intermediate state, which interact with either photon or Z bosons. This process is depicted in Fig. 4.2.

The authors of [113] and [117] performed a one-loop calculation using a monopole form for the meson-nucleon form factor and a dipole form, respectively. Indeed, such calculations are sensitive to the form factor and the value of the cutoff parameter Λ. Furthermore, introducing such form factors leads to the inclusion of seagull diagrams (contact terms at the hadronic vertices, lower two diagrams in Fig. 4.2) in order to satisfy the Ward-Takahashi identity as required by gauge invariance. The choice of these contact terms is not unique and, as noted in [113] results in a $\sim 30\%$ difference in μ_s and $\langle r_s^2 \rangle_E$ in two different procedures of deducing these seagull contact terms.

The strange magnetic moment and radius obtained from the one-loop calculation performed in [113] are $\mu_s = -0.31 \pm 0.05\ \mu_N$ and $\langle r_s^2 \rangle_E = -0.03 \pm 0.003\ \text{fm}^2$, where the uncertainties represent the variation of the cutoff parameter Λ within the range estimated from fits to baryon-baryon scattering, $1.2 \leq \Lambda_{\text{Bonn}} \leq 1.4$ GeV. The authors of [113] argued that one-loop calculations that consider only the lightest pseudoscalar mesons are not able to characterise the nucleon form factors at low-energy regions.

In [118], Malheiro and Melnitchouk mentioned that the impulse approximation, in which the hadronic Fock space is truncated at the one-meson level and contributions arising from many-body currents are neglected, used in the kaon loop calculation leads to a violation of Lorentz covariance. They evaluated the contribution stemming from this concerning violation. Once this contribution was subtracted, they obtained a small and positive value of the strange magnetic moment, $\mu_s = 0.01\ \mu_N$.

Geiger and Isgur performed a non-relativistic quark model calculation to consider the contribution arising from a complete set of OZI-allowed strong Y^*K^* hadronic loops [115], where $Y^*(K^*)$ is the excited intermediate baryon (meson). They accomplished the calculation within an unquenched quark model and obtained a small and positive value of the strange magnetic moment with $\mu_s = 0.035\ \mu_N$, and a negative value of $\langle r_s^2 \rangle_E$ with $\sim -0.04\ \text{fm}^2$. Meißner *et al.* performed calculations in which

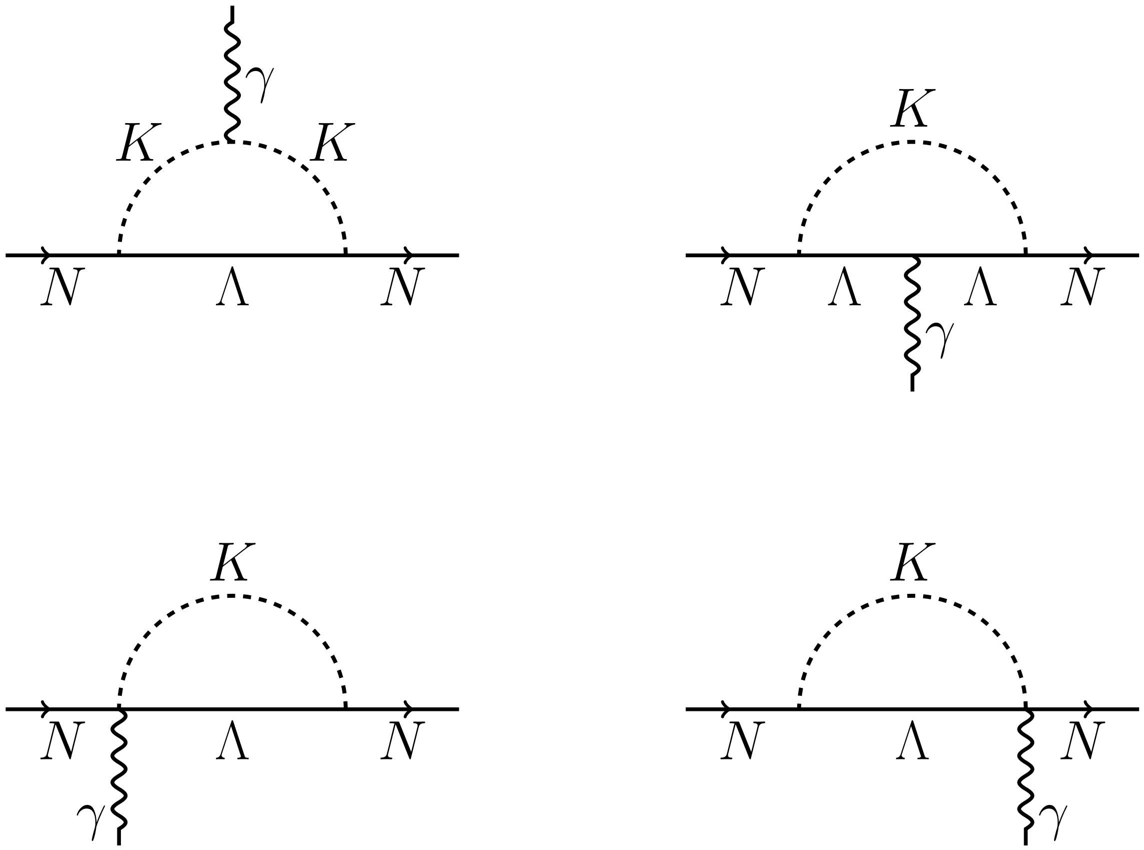

Figure 4.2: Feynman diagrams for kaon loop contribution with γ coupling to either the kaon K or the hyperon Λ. The lower two diagrams (seagull diagrams) are included to fulfil the Ward-Takahashi identity as required by gauge invariance.

the OZI-allowed ϕ meson coupling to the nucleon with inclusion of K^* loops and hyperon excitations has been investigated within a meson-exchange model [119]. They found positive values for both $\langle r_s^2 \rangle_E$ and μ_s.

Forkel *et al.* [120] analysed the dependence of the strange-quark content on the NYK^* form factors in the loop model calculations. They stated that the contributions from the lightest KY intermediate states were adequate for approximate estimates of the nucleon's vector strangeness content in one-loop models. However, they also pointed out that the contributions from K^* remain non-negligible in the large momentum transfer regions.

As a result of these difficulties, one can say that kaon loop calculations are not able to make a conclusive statement about the sign of the $\langle r_s^2 \rangle_E$ and μ_s.

4.1.4 Constituent Quark Model

In [1], Kaplan and Manohar proposed that a constituent quark is comprised of a current QCD quark that is surrounded by a complicated cloud of virtual gluons and

$q\overline{q}$ pairs. Accordingly, it is possible that the constituent U and D quarks inside the nucleon have a strangeness contribution. Kaplan and Manohar stressed that this picture of constituent quarks does not contradict the quark model. In particular, this proposed model does not destroy some of the successful predictions of the quark model, such as the value for the baryon magnetic moments.

In this model, constituent quarks' nontrivial structure is governed by spontaneously broken chiral symmetry induced by the flavour-mixing 't Hooft interaction. This is the so-called chiral quark model.

There are several different methods that one can use to study the strange quark effects within the framework of the constituent quarks model. One of these method utilises the so-called Nambu and Jona-Lasinio model (NJL) [121, 122][5].

The generalisation of the NJL model to $N_f \geq 3$ including $U(1)_A$ symmetry breaking by a $2N_f$-quark interaction has been introduced in [123]. Within the Hartree-Fock approximation, this term entirely generates flavour mixing which is responsible for the strange quark effects in the constituent U and D quarks [123].

Forkel *et al.* performed an estimation of the strangeness radius of the nucleon within the framework of the constituent quark model and obtained a positive and small value of $\langle r_s^2 \rangle_E = 0.0169$ fm^2 [124].

Within the NJL model, the authors of [125] used Yabu-Ando approach [126] to incorporating strange degrees of freedom into the soliton picture. They provided limits for the strange magnetic moment with $-0.05\ \mu_N \leq \mu_s \leq 0.25\ \mu_N$ and for the strange electric radius with -0.25 fm$^2 \leq \langle r_s^2 \rangle_E \leq -0.15$ fm^2 [125].

In [127], the magnitude of the μ_s and $G_M^s(Q^2)$ for $Q^2 \lesssim 1.0$ GeV^2 have been estimated using an extended chiral constituent quark model that studies the contributions stemming from all possible five-quark Fock components to μ_s. The authors' method was inspired by an idea that was proposed by Zou and Riska [128], in which the strangeness magnetic moment of the proton can be described by including five-quark Fock states in the proton. The authors of [127] included the contribution from the nondiagonal matrix elements of the transition between the strangeness and the three-quark components of the proton $\langle uud|\mu_s|uuds\overline{s}\rangle$ and found that the value of μ_s is small and negative.

One should concern about the associated shortcomings with the chiral quark model, in particular, the problem of double counting. This means that there is an ambiguity since the pseudoscalar $Q\overline{Q}$ bound state and the octet of light pseudoscalar Goldstone are introduced in the chiral quark effective theory [103].

---

[5] Yoichiro Nambu was granted one half of the Nobel Prize in Physics in 2008 for his discovery of the mechanism of spontaneous broken symmetry in subatomic physics. The other half awarded to Makoto Kobayashi and Toshihide Maskawa for their discovery of the origin of the broken symmetry.

4.1.5 Skyrme and Soliton Models

Well before the advent of QCD and chiral symmetry, Skyrme assumed that the baryons are solitons in a mesonic field theory. The Skyrme soliton is a topological soliton constructed based on the effective Lagrangian of the chiral non-linear sigma model[6] [129, 130].

The Skyrme model considers a 2×2 unitary field. When considering the strangeness content in the nucleon, one needs to extend the Skyrme model to $SU(3)$.

According to [131], several calculations based on the $SU(3)$ Skyrme model contain ambiguities. $SU(3)$ flavour symmetry breaking needs to be carefully taken into the account. For flavour symmetry breaking, the authors of [131] introduced non-minimal derivative terms in the Lagrangian. From that calculation, the strange magnetic moment and strange charge radius are shown to be negative with $\mu_s = -0.13$ μ_N and $\langle r_s^2 \rangle_E = -0.11$ fm^2, respectively. A calculation within the chiral soliton-quark model was done in [132, 133] and the results were a positive strange magnetic moment and a negative strangeness radius. These studies supported a previous analysis [134], which reported a positive strange magnetic moment of $\mu_s = 0.37$ μ_N based on $SU(3)$ group structure of the chiral models' calculations.

In the Skyrme model, the strangeness current is obtained from the difference between the baryon number and hypercharge currents, and any calculation of strange matrix elements depends on the small difference between two large but uncertain quantities is therefore unreliable [124].

4.1.6 Dispersion Relations

Dispersion relations are a nonperturbative method to study the strangeness of nucleon based on general grounds. The dispersion theory, in general, relies on some basic principles of physics: relativistic covariance, causality and unitarity [135] (see Appendix B).

The Dirac and Pauli form factors, $F_{1,2}(q^2)$ (see Eq. 5.9), measured in electron scattering, are considered as functions of the variable $z = q^2$, and are linked to the region of spacelike momentum transfer, $Q^2 = -q^2 > 0$. From causality, the complex functions $F_{1,2}(z)$ maintain specific analytic properties that allow for a continuation into the complex $z = q^2$ plane, as depicted in Fig. 4.3, and lead to the dispersion relations linking the imaginary and real parts of these form factors, i.e., Cauchy's

---

[6] Currently, in fact, the Skyrme model can be considered as a low-energy effective theory for QCD in the large number of the colours, N_c, limit.

theorem. Using Cauchy's integral formula allows one to explicitly write

$$F_{1,2}(q^2) = F_{1,2}(0) + \frac{q^2}{\pi}\int_{t_0}^{\infty} dt \frac{\Im m\ F_{1,2}(t)}{t(t - q^2 - i\epsilon)}, \tag{4.8}$$

where t_0 is given by the lightest hadronic intermediate state contributing to the form factors. The physical bound of $F_{1,2}(0)$ can be employed. The imaginary parts are treated as spectral functions, i.e., Eq. (4.7).

The general dispersion relation is related to all possible on-shell intermediate states. For the strangeness form factors, some of the allowed intermediate states (continuum) contributions are purely mesonic 3π, 5π, 7π, $K\overline{K}$, ... and purely baryonic $N\overline{N}$, $\Lambda\overline{\Lambda}$.... One can also take into account the states that contain both mesons and baryons, such as $N\overline{N}\pi\pi$.

The on-shell continuation from $K\overline{K}$ is the most relevant to the dispersion relation in a study of nucleon strangeness, since it forms the lightest intermediate state comprising valence s and $\overline{s}$ quarks. In this regard, the authors of [136] performed the first calculations. The spectral functions were related to the partial waves and the kaon strangeness form factor [136]. Musolf *et al.* [136] showed that, when considering the kaon's strange form factor to be point-like, $F_K^{(s)} = -1$, the Born approximation of $K\overline{K} \to N\overline{N}$ amplitude is similar to those resulting from one-loop kaon calculations with a significant violation of unitarity in the physical region. Therefore, they suggested that rescattering corrections are required by unitarity.

In [137–139], the authors improved this analysis. They fixed the $J = 1$ partial wave amplitudes in the physical region at their unitarity bounds. They observed that the time-like F_K^s is dominated by the ϕ resonance. In their analysis, the strangeness magnetic moment and strangeness radius were found to be $\mu_s = -0.42\ \mu_N$ and $\langle r_s^2 \rangle_E = -0.07\ \text{fm}^2$, respectively.

The work presented in [140] discussed the importance of the contribution arising from multi-meson intermediate states that do not contain valence s or $\overline{s}$-quarks. Although the contribution from these states violates the naive interpretation of the OZI-rule, the authors found the that magnitude of this contribution was similar to that of the lightest OZI-allowed intermediate state, the $K\overline{K}$ continuum.

4.1.7 Lattice Quantum Chromodynamics (LQCD)

The theoretical approaches discussed in the previous sections are not able to render a complete physical understanding of the nucleon's strangeness content.

Lattice quantum chromodynamics (LQCD), first proposed by Wilson[7] in 1974 [141],

---

[7] Wilson was awarded the 1982 Nobel Prize in Physics for his work on phase transitions.

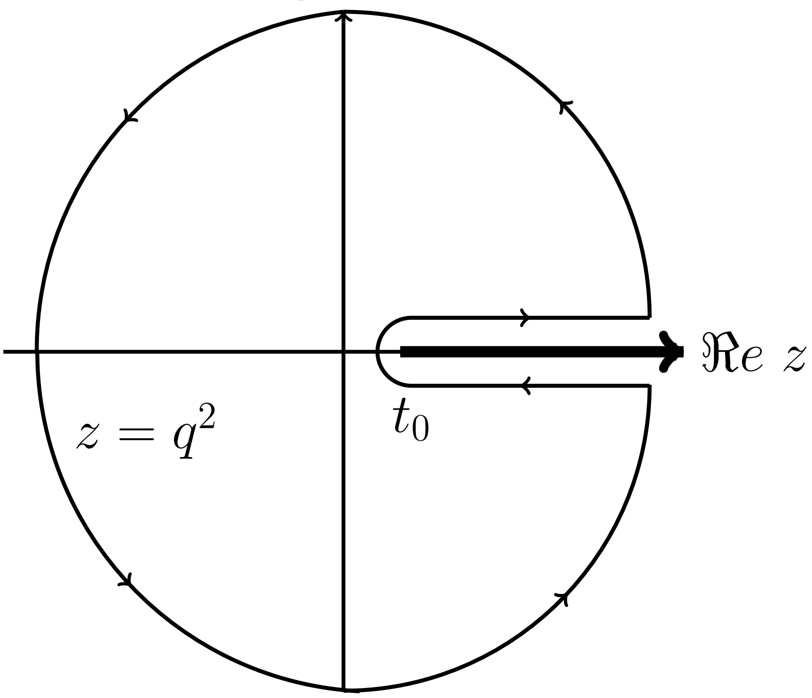

Figure 4.3: Analytic structure for the form factors of the nucleon in the complex $z = q^2$ plane.

is a nonperturbative approach to solving numerically the QCD. LQCD is a gauge theory formulated on a discrete Euclidean space-time grid (or lattice), and it has successfully described many properties of hadrons. In this section, a general overview of the LQCD approach will be provided.

LQCD is a nonperturbative implementation of field theory based on the Feynman path integral formalism.

Within the framework of lattice QCD, the chiral extrapolation plays a significant role. Lattice calculations are often performed at larger-than-physical quark masses. For a quenched lattice theory, where vacuum polarisation loops are neglected, the relevant theory requires to be modified to the quenched chiral perturbation theory [142].

The contributions of the strange quark to the electromagnetic form factors of the nucleon in lattice QCD can be derived from a three-point Green's function. Both Feynman diagrams of connected and disconnected operator insertions, illustrated in Fig. 3.2, contribute to the nucleon three-point function. The disconnected operator insertions are very computationally expensive compared to the connected insertions.

The first quenched lattice calculation of the strangeness magnetic moment of the nucleon and strangeness Sachs electric mean-square radius[8] was performed in [143], and the results of that work are $\mu_s = -0.36 \pm 0.20~\mu_N$, $\langle r_s^2 \rangle_E = -0.061 \pm 0.003$ fm^2 and $\langle r_s^2 \rangle_E = -0.16 \pm 0.06$ fm^2 with a monopole mass from $G_M^s(q^2)$. An updated calculation [144] shifted the value of the strange magnetic moment to be $\mu_s = -0.28 \pm 0.10~\mu_N$.

Within the study of the disconnected sea-quark contribution to nucleon magnetic moments, Leinweber derived a set of QCD equalities for octet baryons under the assumption of charge symmetry [145].

A calculation within this framework was performed in [146] and the value of $\mu_s = -0.16 \pm 0.18~\mu_N$ was obtained with the ratio of s and d disconnected quark loops ${}^l R_d^s = 0.55$. A similar procedure was completed in [147] and the value of $\mu_s = -0.046 \pm 0.019~\mu_N$ was obtained with the ratio ${}^l R_d^s = 0.139 \pm 0.042$, where a correction from the quenched ChPT to full ChPT was considered.

A recent evaluation, where the full QCD was employed (vacuum polarisation loops were taken into account, but the disconnected current was not computed directly), has described the Q^2-dependence of ${}^l R_d^s$, where an estimation of ${}^l R_d^s$ from effective field theory with finite-range regularisation was accomplished [148]. In that work, experimental numbers for the electromagnetic factors were combined with lattice QCD results for the connected light quark contributions, leading to an estimate of the s quark contribution. In [148], Shanahan *et al.* concluded that the strange magnetic moment is small and negative, $\mu_s = -0.07 \pm 0.03~\mu_N$, whereas they were not able to make a conclusive statement about the sign of $\langle r_s^2 \rangle_E$.

In [149], Green *et al.* argued the procedure that was followed in [148] depended on a sensitive cancellation between large quantities, and consequently is limited in its statistical precision and somewhat responsive to systematic errors in the lattice calculations. They made a direct lattice QCD calculation of the strange nucleon electromagnetic form factors in a specific range of Q^2 and performed model-independent fits of the form factors using a z-expansion. The authors found that $\mu_s = -0.022 \pm 0.004 \pm 0.004 \pm 0.006~\mu_N$ and $\langle r_s^2 \rangle_E = -0.0067 \pm 0.0010 \pm 0.0017 \pm 0.0015$ fm^2 (non zero signal for the first time), where the first two uncertainties are statistical and systematic and the third uncertainty is due to extrapolation to the physical point. A previous direct calculation found that the strange magnetic moment is consistent with zero, $\mu_s = -0.017 \pm 0.025 \pm 0.007~\mu_N$ (the first error is statistical and the second error indicates the uncertainties in Q^2 and chiral extrapolations), where $N_f = 2 + 1$ clover fermion lattice QCD calculations have been presented with heavier pion masses [150]. Recently, a direct estimation of the strange elec-

---

[8] Sachs and Dirac charge radii will be revisited in more detail in the next chapter.

tromagnetic form factors including, for the first time, the physical pion mass was presented in [151], where a model-independent z-expansion to extract the strange magnetic moment and strange charge radius from the electromagnetic form factors in a specific kinematic range of momentum transfer Q^2 was performed. From that calculation, the strange magnetic moment and strange charge radius are shown to be nonzero with $\mu_s = -0.064 \pm 0.017\ \mu_N$ and $\langle r_s^2 \rangle_E = -0.0043 \pm 0.0021\ \text{fm}^2$, where the uncertainties show the combined statistical and systematic uncertainties added in quadrature [151].

4.2 Summary and Discussion

The above theoretical review emphasises that predictions of the strange magnetic moment μ_s widely vary. Most of the theoretical frameworks lead to negative values, while a few give positive values. A similar situation has been encountered for the strangeness electric mean-square radius $\langle r_s^2 \rangle_E$. Various models conclude with positive outcomes, while the others end with negative predictions. Moreover, this survey shows that significant theoretical uncertainties are associated with the theoretical approaches. For reader convenience, Table 4.1 presents a summary of various theoretical predictions of μ_s and $\langle r_s^2 \rangle_E$.

Thus far, it is possible to state that the theoretical approaches render ambiguous estimations. Treatments within the effective theory framework such as BChPT to predict the strangeness of the nucleon are associated with difficulties related to the unknown low-energy constant (counterterms). Phenomenological models that use dispersion relation involving VMD utilising pole approaches in the unphysical region suffer from the insufficiency of the high precision data for the time-like electromagnetic form factors. Lattice QCD is a first-principles approach to QCD, and therefore it can provide model-independent predictions. However, most of the early lattice QCD studies are based on the quenched approximation and they only considered the calculation of the connected diagram contribution. Very recently, there have been several extensive direct calculations of nucleon strangeness that involve calculations of the disconnected diagram, which is extremely expensive to be computed.

Table 4.1: Theoretical predictions of strangeness magnetic moment μ_s in units of the nuclear magneton μ_N and the strangeness electric mean-square radius $\left\langle r_s^2 \right\rangle_E$ in fm^2.

Theoretical Model	$\mu_s[\mu_N]$	$\left\langle r_s^2 \right\rangle_E[\text{fm}^2]$	Ref.
Vector Meson Dominance (VMD)	-0.31±0.09	0.14±0.09	[111]
Simple Kaon Loop	-0.31±0.05	-0.03±0.003	[113]
Kaon Loop including excited hadronic states	0.035	-0.04	[115]
NJL soliton	-0.05→+0.25	-0.25→-0.15	[125]
Extended Chiral Constituent Quark Model	-0.067±0.004	–	[127]
SU(3) Skyrme (broken symmetry)	-0.13	-0.11	[131]
SU(3) Skyrme (broken symmetry)	0.37	–	[134]
Dispersion	-0.42	-0.07	[139]
Lattice (first quenched calculation)	-0.36±0.20	-0.061→-0.16	[143]
Lattice	-0.064±0.017	-0.0043±0.0021	[151]

Chapter 5

Parity-Violating (PV) Elastic Electron–Nucleon Scattering

It is known that, in addition to the purely electromagnetic (EM) interaction that conserves parity, the electron also interacts via the weak interaction that violates parity. Despite the fact that the weak interaction is several orders of magnitude smaller than the electromagnetic interaction, the weak interaction can play a critical role when analysing a part of nucleon structure that cannot be investigated through studies that only consider the EM interaction.

Nucleon structure can be described in terms of the valence quarks and the sea quarks that are held together by the strong force carried by gluons. The strange quark contribution to the nucleon EM form factor is then a pure sea quark effect.

In 1988, Kaplan and Manohar [1] proposed that the strange electric and magnetic form factors contributions, G_E^s and G_M^s, respectively, can be estimated through the measurements of the weak neutral current matrix elements in neutrino-nucleon scattering. Shortly after, in 1989, McKeown [2] and Beck [3] suggested an experimental probe that used parity-violating electron scattering to measure the weak neutral current of the proton in order to acquire information relevant to the strange quark vector matrix elements. This method for the study of these matrix elements generated significant interest among the community and was followed by more than two decades of experimental investigations.

The PV asymmetry A_{PV} is defined as the difference divided by the sum of the cross sections for the scattering of circularly polarised positive and negative helicity electrons on an unpolarised target:

$$A_{PV} = \frac{\sigma_+ - \sigma_-}{\sigma_+ + \sigma_-}. \tag{5.1}$$

The processes of lowest order contributions to electron-nucleon scattering, plane-wave Born approximation (tree level) with a single-boson (γ or Z^0) exchange, are depicted in Fig. 5.1. The electromagnetic interaction (γ-exchanged) is parity-conserving, while the weak interaction (Z^0-exchanged) contains vector and axial-vector components having opposite behaviour under a parity transformation and is the origin of the parity-violating, non-zero value of the A_{PV}. In this scattering, the incident electron with four-momentum $k = (E, \vec{k})$ is scattered from a target nucleon at rest in the lab frame with four-momentum $p = (M_N, 0)$ through scattering angle θ to an outgoing electron with four-momentum $k' = (E', \vec{k}')$ exchanging Z^0 or photon. After the scattering process, the nucleon is described with four-momentum $p' = (E_N, \vec{p}')$. The momentum transfer in the scattering process, the energy and momentum lost by the electron, is given by $Q = (\omega, \vec{q})$, where $\omega = E - E'$ and $\vec{q} = \vec{k} - \vec{k}'$. In this scattering event, the electron is treated in the extreme relativistic limit, $m_e = 0$. The invariant squared four-momentum transfer Q^2 of the scattering is defined as $Q^2 = \omega^2 - \vec{q}^2 = -q^2 > 0$. For elastic electron scattering, $Q^2 = 4EE' \sin^2(\theta/2)$.

The total invariant amplitude of elastic electron-nucleon scattering is the sum of the electromagnetic $\mathcal{M}^\gamma$ and neutral weak current $\mathcal{M}^Z$ amplitudes. The cross section σ is proportional to $\mathcal{M}^\gamma$ and $\mathcal{M}^Z$:

$$\sigma \; \alpha \; |\mathcal{M}^\gamma + \mathcal{M}^Z|^2. \tag{5.2}$$

This relation will be revisited in a subsequent section and discussed in more detail.

For two decades, great efforts have been dedicated to the measurement of the parity-violating asymmetry to study the strangeness content contributions to the nucleon EM form factors.

This chapter will discuss the relevant formalism to the description of PV asymmetry for elastic electron-proton scattering, elastic electron-helium-4 scattering and quasielastic electron-deuteron scattering. Higher-order electroweak corrections will be highlighted and considered in the analysis of this work. In the present work, the axial-vector form factors are managed as implicitly containing higher-order radiative corrections and hadronic anapole contributions, and the total of these contributions will be evaluated from the analysis of the considered data set. The last section of this chapter will briefly highlights the experimental programs that discuss PV electron scattering from the proton, helium-4 or deuteron with varying kinematic conditions and measured A_{PV}. The set of all available PV electron scattering data from the proton, helium-4 or deuteron, up to the currently available limit of $Q^2 \sim 1\text{GeV}^2$, that are considered in this work will be presented at the end of this chapter.

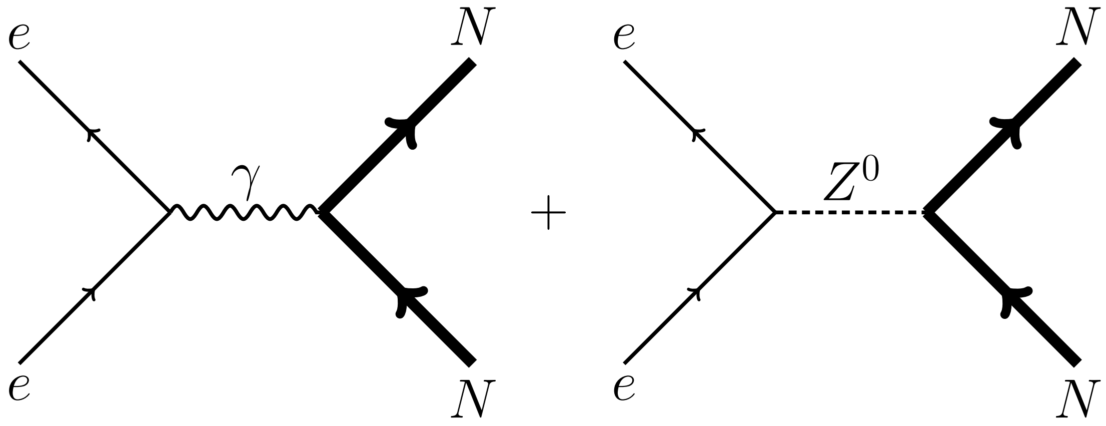

Figure 5.1: Lowest order amplitudes contributing to electron-nucleon scattering. Leading order electromagnetic (γ-exchanged) and neutral (Z^0-exchanged) current amplitudes.

5.1 Nucleon Form Factors

From the fundamental coupling of an elementary fermion to the photon or to the Z^0, one can write the general form of electromagnetic and weak invariant amplitudes as [10]

$$\begin{aligned}\mathcal{M}^\gamma &= -\frac{4\pi\alpha}{q^2} Q_f l^\mu J^\gamma_\mu,\\ \mathcal{M}^Z &= -\frac{4\pi\alpha}{M_Z^2 - q^2}\frac{1}{(4\sin\theta_W\cos\theta_W)^2}(g_V^f l^\mu + g_A^f l^{\mu 5})(J^Z_\mu + J^Z_{\mu 5}),\end{aligned} \tag{5.3}$$

where $\alpha = e^2/(4\pi)$ is the fine structure constant, and l^μ and $l^{\mu 5}$ are leptonic vector and axial vector currents, respectively. In the case of electron scattering, these currents are Dirac currents and they can be defined as

$$\begin{aligned}l^\mu &= \overline{\psi}_e \gamma^\mu \psi_e,\\ l^{\mu 5} &= \overline{\psi}_e \gamma^\mu \gamma^5 \psi_e.\end{aligned} \tag{5.4}$$

J^μ and $J^{\mu 5}$ are hadronic vector and axial vector currents, respectively, and they are related to the hadronic matrix elements of the electromagnetic, vector and axial-vector quark current operators as

$$\begin{aligned} J_\mu^\gamma &= \langle N|\hat{J}_\mu^\gamma|N\rangle;\ \text{with } \hat{J}_\mu^\gamma = \sum_q Q_q \overline{\psi}_q \gamma^\mu \psi_q, \\ J_\mu^Z &= \langle N|\hat{J}_\mu^Z|N\rangle;\ \text{with } \hat{J}_\mu^Z = \sum_q g_V^q \overline{\psi}_q \gamma^\mu \psi_q, \\ J_{\mu 5}^Z &= \langle N|\hat{J}_{\mu 5}^Z|N\rangle;\ \text{with } \hat{J}_{\mu 5}^Z = \sum_q g_A^q \overline{\psi}_q \gamma^\mu \gamma^5 \psi_q. \end{aligned} \tag{5.5}$$

Q_f is the electromagnetic charge of the fermion, f, and g_V^f and g_A^f are the vector and axial-vector weak couplings defined in Chapter 2 and given explicitly in Table 2.2.

The q^2-dependence in $\mathcal{M}^Z$, which stems from the Z^0 boson propagator, can be safely neglected since $|q^2| \ll M_Z^2$ for the kinematics considered in this work. Therefore, the weak interaction is commonly considered as a contact interaction that has a strength characterised by the Fermi constant measured in muon decay G_F [10]. This constant can be expressed as

$$G_F = \frac{\pi\alpha}{\sqrt{2} M_W^2 \sin^2\theta_W}, \tag{5.6}$$

where θ_W is the weak mixing angle and M_W is the mass of the W boson. This definition, along with the weak mixing angle defined in Eq. (2.20), which implies that $\cos^2\theta_W = M_W^2/M_Z^2$, yields

$$\mathcal{M}^Z = -\frac{G_F}{2\sqrt{2}}(g_V^f l^\mu + g_A^f l^{\mu 5})(J_\mu^Z + J_{\mu 5}^Z). \tag{5.7}$$

The PV term of $\mathcal{M}^Z$ is

$$\mathcal{M}_{PV}^Z = -\frac{G_F}{2\sqrt{2}}(g_V^f l^\mu J_{\mu 5}^Z + g_A^f l^{\mu 5} J_\mu^Z). \tag{5.8}$$

Back to the hadronic matrix elements in Eq. (5.5), from Lorentz invariance, the matrix element for the electromagnetic interaction can be written as [67]

$$\langle N(p')|J_\mu^\gamma|N(p)\rangle = \overline{U}(p')\left[\gamma^\mu F_1^\gamma(Q^2) + \frac{i\sigma^{\mu\nu}q_\nu}{2M}F_2^\gamma(Q^2)\right]U(p), \tag{5.9}$$

where $\overline{U}(p')$ and $U(p)$ are the nucleon spinors for the final and initial momenta p' and p respectively, and $\sigma^{\mu\nu} = \frac{i}{2}[\gamma^\mu, \gamma^\nu]$. The form factors F_1^γ and F_2^γ are the Dirac and Pauli form factors, respectively. These form factors are normalised at limit

$Q^2 = 0$ as

$$\begin{aligned} F_1^\gamma(0) &= Q_N, \\ F_2^\gamma(0) &= \kappa_N, \end{aligned} \tag{5.10}$$

where Q_N is the electric charge of the nucleon and κ_N is the anomalous magnetic moment of the nucleon in units of the nuclear magneton (μ_N). Similarly, the hadronic matrix element for the neutral weak vector current can be expressed as

$$\langle N(p')|J_\mu^Z|N(p)\rangle = \overline{U}(p')\left[\gamma^\mu F_1^Z(Q^2) + \frac{i\sigma^{\mu\nu}q_\nu}{2M}F_2^Z(Q^2)\right]U(p). \tag{5.11}$$

5.1.1 Sachs Form Factors

Linear combinations of Dirac and Pauli form factors, F_1 and F_2, are commonly used. These combinations are known as Sachs form factors and may be defined as [152]

$$\begin{aligned} G_E^N &= F_1(Q^2) - \frac{Q^2}{4M_N^2}F_2(Q^2), \\ G_M^N &= F_1(Q^2) + F_2(Q^2), \end{aligned} \tag{5.12}$$

where G_E^N and G_M^N are the electric and magnetic form factors of the nucleon, respectively.

A characteristic of the Sachs form factors is that, in the center of mass frame (Breit frame), they are the Fourier transforms of the nucleon magnetic moment and charge distributions [152]. As an illustration, expanding $G_E^N(Q^2)$ at small Q^2:

$$\begin{aligned} \int e^{i\vec{q}\cdot\vec{r}}\ \rho(r)\ d^3r &= \int\ (1 - i\vec{q}\cdot\vec{r} - \frac{1}{2}(\vec{q}\cdot\vec{r})^2 + \ldots)\rho(r)\ d^3r \\ &= Q_N - \frac{1}{6}q^2\int\ r^2\ \rho(r)\ dr\ + \ldots \\ &= Q_N - \frac{1}{6}q^2\langle r^2\rangle\ + \ldots\ . \end{aligned} \tag{5.13}$$

Then,

$$G_E^N(Q^2) = Q_N - \frac{1}{6}Q^2\langle r^2\rangle\ + \ldots\ . \tag{5.14}$$

In general, therefore, the Sachs charge radius can be defined as

$$\langle r^2\rangle = -6\frac{dG(Q^2)}{dQ^2}\bigg|_{Q^2=0}. \tag{5.15}$$

In the Breit frame, for elastic electron scattering, the incoming electron has momentum $\vec{k} = +\vec{q}/2$ and scatters from a nucleon which has momentum equal in magnitude but opposite in sign, $\vec{p} = -\vec{q}/2$. The recoiled electron has momentum $\vec{k}' = -\vec{q}/2$ and the nucleon scatters with momentum $\vec{p}' = +\vec{q}/2$ [67]. The dependence of the Sachs form factors on Q^2 leads to a variation of the Breit frame with Q^2.

The physical interpretation of the Sachs EM form factors of the nucleon is that the Fourier transforms of these form factors give the static charge and magnetisation densities for the nucleon in the Breit frame. However, the momenta of the initial and final nucleons are differ, i.e., the final wave function is boosted from the initial state nucleon wave function. This means that a relativistic treatment is required.

5.1.2 Flavour Decomposition

The quark current operators defined in Eq. (5.5) allow one to express the hadronic matrix elements in terms of the quark flavour decomposition as

$$\begin{aligned}
\langle N(p')|J_\mu^\gamma|N(p)\rangle &= \overline{U}(p')\sum_q Q_q\left[\gamma^\mu F_1^q(Q^2) + \frac{i\sigma^{\mu\nu}q_\nu}{2M_q}F_2^q(Q^2)\right]U(p),\\
\langle N(p')|J_\mu^Z|N(p)\rangle &= \overline{U}(p')\sum_q g_V^q\left[\gamma^\mu F_1^q(Q^2) + \frac{i\sigma^{\mu\nu}q_\nu}{2M_q}F_2^q(Q^2)\right]U(p),
\end{aligned} \tag{5.16}$$

where F_1^q and F_2^q are the Dirac and Pauli, respectively, for the quark flavour q. It is worth mentioning that F_1^q and F_2^q are identical for the electromagnetic and weak interactions since the charges have been factored out.

From Eqs. (5.5), (5.9), (5.11) and (5.16), the Dirac, Pauli and axial form factors of the nucleon can be written in terms of the quark flavour form factors as

$$\begin{aligned}
F_{1,2}^{\gamma N} &= \sum_q Q_q F_{1,2}^q,\\
F_{1,2}^{ZN} &= \sum_q g_V^q F_{1,2}^q,\\
G_A^{eN} &= \sum_q g_A^q G_A^{eq}.
\end{aligned} \tag{5.17}$$

Analogously, the electromagnetic and neutral weak Sachs form factors can be written as

$$\begin{aligned} G_{E,M}^{\gamma N} &= \sum_q Q_q G_{E,M}^q, \\ G_{E,M}^{ZN} &= \sum_q g_V^q G_{E,M}^q. \end{aligned} \tag{5.18}$$

5.1.2.1 Flavour Decomposition of the Vector Form Factors

The contributions of the heavy quarks (c, b and t) to the nucleon properties are strongly suppressed. Therefore, from Eq. (5.18), the proton and neutron Sachs form factors are reduced to

$$\begin{aligned} G_{E,M}^{\gamma p} &= Q_u G_{E,M}^{u,p} + Q_d G_{E,M}^{d,p} + Q_s G_{E,M}^{s}, \\ G_{E,M}^{\gamma n} &= Q_u G_{E,M}^{u,n} + Q_d G_{E,M}^{d,n} + Q_s G_{E,M}^{s}, \end{aligned} \tag{5.19}$$

where $Q_{u,d,s}$ are the electric charges of the respective quarks. Here, the strange quark contribution to the proton and neutron electromagnetic form factors have been treated on an equal footing. Likewise, the neutral weak Sachs form factors can be defined as

$$\begin{aligned} G_{E,M}^{Zp} &= g_V^u G_{E,M}^{u,p} + g_V^d G_{E,M}^{d,p} + g_V^s G_{E,M}^{s}, \\ G_{E,M}^{Zn} &= g_V^u G_{E,M}^{u,n} + g_V^d G_{E,M}^{d,n} + g_V^s G_{E,M}^{s}, \end{aligned} \tag{5.20}$$

where $g_V^{u,d,s}$ are the vector charges of the considered quarks.

Under the assumption of charge symmetry, the individual quark contributions to the proton and neutron form factors can be related to each other, i.e.,

$$G_{E,M}^{u} \equiv G_{E,M}^{u,p} = G_{E,M}^{d,n} \text{ and } G_{E,M}^{d} \equiv G_{E,M}^{d,p} = G_{E,M}^{u,n}. \tag{5.21}$$

This assumption allows for a further reduction of the number of the parameters existing in the system of the four preceding equations. Therefore, one can simply define the electromagnetic and neutral weak Sachs form factors for both nucleons as

$$\begin{aligned} G_{E,M}^{\gamma p} &= Q_u G_{E,M}^{u} + Q_d G_{E,M}^{d} + Q_s G_{E,M}^{s}, \\ G_{E,M}^{\gamma n} &= Q_u G_{E,M}^{d} + Q_d G_{E,M}^{u} + Q_s G_{E,M}^{s}, \\ G_{E,M}^{Zp} &= g_V^u G_{E,M}^{u} + g_V^d G_{E,M}^{d} + g_V^s G_{E,M}^{s}, \\ G_{E,M}^{Zn} &= g_V^u G_{E,M}^{d} + g_V^d G_{E,M}^{u} + g_V^s G_{E,M}^{s}. \end{aligned} \tag{5.22}$$

This highlights the importance of the interference of electromagnetic and weak interactions. Purely electromagnetic electron scattering deals with solely two linear combinations of the form factors mentioned above, i.e., $G^{\gamma p}_{E,M}$ and $G^{\gamma n}_{E,M}$. It is clear that additional information is required in order to determine the strangeness form factors $G^{s}_{E,M}$ contribution. This information is given by parity violation in electron-nucleon scattering which measures $G^{Zp}_{E,M}$.

Rearranging $G^{\gamma p}_{E,M}$, $G^{\gamma n}_{E,M}$ and $G^{Zp}_{E,M}$ in Eq. (5.22) using the electric charges of the quarks $Q_u = 2/3$, $Q_d = -1/3$ and $Q_s = -1/3$ leads to an expression for the proton's neutral weak form factor in terms of the well-known electromagnetic form factors of the proton and neutron [10]:

$$\begin{aligned} G^{Zp}_{E,M} &= (2g^u_V + g^d_V)G^{\gamma p}_{E,M} + (g^u_V + 2g^d_V)G^{\gamma n}_{E,M} + (g^u_V + g^d_V + g^s_V)G^{s}_{E,M} \\ &= g^p_V G^{\gamma p}_{E,M} + g^n_V G^{\gamma n}_{E,M} + g^{(0)}_V G^{s}_{E,M}. \end{aligned} \tag{5.23}$$

This equation contains only one significant unknown quantity, the strangeness form factors $G^{s}_{E,M}$.

At tree level, the SM values of vector charges are

$$g^p_V = 1 - 4\sin^2\theta_W,\ g^n_V = -1 \text{ and } g^{(0)}_V = -1. \tag{5.24}$$

Thus, at tree level, the proton's neutral weak form factor becomes

$$G^{Zp}_{E,M} = (1 - 4\sin^2\theta_W)G^{\gamma p}_{E,M} - G^{\gamma n}_{E,M} - G^{s}_{E,M}. \tag{5.25}$$

A similar procedure can be followed to express the neutron's neutral weak form factor as

$$G^{Zn}_{E,M} = (1 - 4\sin^2\theta_W)G^{\gamma n}_{E,M} - G^{\gamma p}_{E,M} - G^{s}_{E,M}. \tag{5.26}$$

5.1.2.2 Flavour Decomposition of the Axial Form Factors

From Eq. (5.17), one can define the neutral weak axial form factors of the proton and neutron, with assuming charge symmetry, as

$$\begin{aligned} G^{ep}_A &= g^u_A G^u_A + g^d_A G^d_A + g^s_A G^s_A, \\ G^{en}_A &= g^u_A G^d_A + g^d_A G^u_A + g^s_A G^s_A. \end{aligned} \tag{5.27}$$

Usually, with using $SU(3)$ symmetry, the quark axial-vector form factors are written in terms of the isovector $G^{(3)}_A$, isoscalar $G^{(8)}_A$ and strange axial-vector G^s_A

form factors as

$$G_A^{(3)} = G_A^u - G_A^d,$$
$$G_A^{(8)} = \frac{1}{2\sqrt{3}}(G_A^u + G_A^d - 2G_A^s). \tag{5.28}$$

Consequently, G_A^{eN} becomes [10]

$$\begin{aligned} G_A^{eN} &= \frac{1}{2}(g_A^u - g_A^d)\tau_3 G_A^{(3)} + \sqrt{3}(g_A^u + g_A^d)G_A^{(8)} + (g_A^u + g_A^d + g_A^s)G_A^s, \\ &= g_A^{T=1}\tau_3 G_A^{(3)} + g_A^{T=0}G_A^{(8)} + g_A^{(0)}G_A^s, \end{aligned} \tag{5.29}$$

where the Q^2-dependence has been dropped for clarity, and $\tau_3 = +1(-1)$ for the proton(neutron).

At tree level, the SM values of the axial-vector charges are

$$g_A^{T=1} = -1,\ g_A^{T=0} = 0 \text{ and } g_A^{(0)} = 1, \tag{5.30}$$

where, from the middle equality, the $SU(3)$ octet form factor $G_A^{(8)}$ is absent at tree level, but will emerge when radiative corrections are taken into account as will be discussed later.

The Q^2-dependence of $G_A^{(3)}$ is parameterised with a dipole form $G_A^D(Q^2)$ [153, 154] as

$$G_A^{(3)}(Q^2) = G_A^{(3)}(0)G_A^D(Q^2). \tag{5.31}$$

The Q^2-dependence of $G_A^{(8)}$ and G_A^s are unknown. However, it is assumed to have the same dipole form description. The dipole form $G_A^D(Q^2)$ is defined as

$$G_A^D(Q^2) = \frac{1}{\left(1 + \frac{Q^2}{M_A^2}\right)^2}. \tag{5.32}$$

The axial-vector dipole mass M_A is usually extracted from charged-current quasielastic neutrino-nucleus scattering.

At $Q^2 = 0$, the axial-vector form factors are normalised as the spin contributions of the net nucleon spin, and they can be defined as

$$\begin{aligned} G_A^{(3)}(0) &= \Delta u - \Delta d, \\ G_A^{(8)}(0) &= \frac{1}{2\sqrt{3}}(\Delta u + \Delta d - 2\Delta s), \\ G_A^s(0) &= \Delta s, \end{aligned} \tag{5.33}$$

where Δq is the net contribution of quark q to the nucleon spin. $G_A^{(3)}(0)$ is well known from β-decay. The $SU(3)$ octet form factor $G_A^{(8)}(0)$ is estimated by combining nucleon and hyperon β-decay assuming $SU(3)$ flavour symmetry. Δs has been indirectly determined from deep inelastic scattering (DIS)[154]. Other estimations of this quantity have been undertaken through the quasielastic neutrino scattering [74], lattice QCD [155] and global fits of parity-violating elastic electron-proton scattering data combined with ν–p and $\overline{\nu}$–p scattering data [76, 77].

5.2 Parity Violation in Electron Scattering

As mentioned at the beginning of this chapter, the total invariant amplitude for e–p elastic or quasielastic scattering is simply a sum of the scattering amplitudes $\mathcal{M}^\gamma$ and $\mathcal{M}^Z$, as shown in Eq. (5.2)

$$\sigma = |\mathcal{M}^\gamma + \mathcal{M}^Z|^2 = |\mathcal{M}^\gamma|^2 + 2\Re e(\mathcal{M}^{\gamma^*}\mathcal{M}^Z) + |\mathcal{M}^Z|^2. \tag{5.34}$$

The electromagnetic scattering amplitude $\mathcal{M}^\gamma$ is the dominant part of the total amplitude. The weak neutral scattering amplitude $\mathcal{M}^Z$ interference with $\mathcal{M}^\gamma$, $\Re e(\mathcal{M}^{\gamma^*}\mathcal{M}^Z)$, is suppressed at low Q^2 by the Fermi constant G_F. Within the range of low Q^2, the pure weak neutral scattering amplitude can be safely neglected since it is suppressed by G_F^2. The interference term is most relevant for this study because it causes parity violation, where the PV term is encoded in $\mathcal{M}^Z$, Eq. (5.8), i.e., the sign of the axial-vector parts of the $\mathcal{M}^Z$ changes with the electron's helicity.

Excluding the parity-conserving terms from $\mathcal{M}^Z$ leads to

$$A_{PV} = \frac{2\Re e(\mathcal{M}^{\gamma^*}\mathcal{M}^Z_{PV})}{|\mathcal{M}^\gamma|^2}, \tag{5.35}$$

where $|\mathcal{M}^\gamma|^2$ is cancelled in the numerator and dominates in the denominator of Eq. (5.1). Utilising Eqs. (5.3, 5.8, 5.9, 5.11 and 5.12), one finds that the PV asymmetry in polarised e–N scattering at tree level is given by [10]

$$A^N_{PV} = \left[\frac{-G_F Q^2}{4\sqrt{2}\pi\alpha}\right].(A_E + A_M + A_A), \tag{5.36}$$

with the electric A_E, magnetic A_M and axial A_A components of the asymmetry defined as

$$A_E = \frac{\epsilon G_E^{\gamma,N} G_E^{Z,N}}{\epsilon (G_E^{\gamma,N})^2 + \tau (G_M^{\gamma,N})^2}, \tag{5.37}$$

$$A_M = \frac{\tau G_M^{\gamma,N} G_M^{Z,N}}{\epsilon(G_E^{\gamma,N})^2 + \tau(G_M^{\gamma,N})^2} \tag{5.38}$$

and

$$A_A = \frac{-\epsilon'(1 - 4\sin^2\hat{\theta}_W) G_M^{\gamma,N} G_A^{e,N}}{\epsilon(G_E^{\gamma,N})^2 + \tau(G_M^{\gamma,N})^2}, \tag{5.39}$$

where the Q^2-dependence of the nucleon form factors has been omitted for clarity. The kinematic variables, which depend on the four-momentum transfer $Q^2 = -q^2$ and the electron lab scattering angle θ, can be expressed as

$$\tau = \frac{Q^2}{4M_N^2}, \tag{5.40}$$

$$\epsilon = \frac{1}{1 + 2(1+\tau)\tan^2\frac{\theta}{2}} \tag{5.41}$$

and

$$\epsilon' = \sqrt{\tau(1+\tau)(1-\epsilon^2)}, \tag{5.42}$$

where M_N, ϵ and ϵ' are the nucleon mass, the longitudinal polarisation of the virtual photon and the scattered energy, respectively.

The values of the Standard Model parameters for the Fermi coupling $G_F = 1.16638 \times 10^{-5}$ GeV^{-2}, the fine structure constant $\alpha = 1/137.036$ and the weak mixing angle in the $\overline{\mathrm{MS}}$ renormalisation scheme at Z boson's mass $\sin^2\hat{\theta}_W = 0.23129$ are taken from the PDG [15] and will be used in the present work.

The A_{PV} defined in Eq. (5.36) has been written as a function of the squared momentum transfer and scattering angle, $A_{PV}(Q^2, \theta)$. The multiplicative factor, $-G_F Q^2/(4\sqrt{2}\pi\alpha)$, which stems from the electromagnetic and neutral weak couplings and propagators, gives an order of magnitude of $10^{-6} - 10^{-4}$. This means that the asymmetries are usually measured in parts per million (ppm).

Since A_{PV} depends on the kinematic conditions, Q^2 and θ, the PV measurements are sensitive to the A_E and A_M components at forward scattering angles ($\theta \to 0; \epsilon \to 1$), while these measurements are sensitive to the A_M and A_A components at backward scattering angles ($\theta \to \pi; \epsilon \to 0$).

5.2.1 Strangeness Vector from A_{PV}

Using Eq. (5.25) allows one to isolate the strangeness vector, A_s^p, and the PV asymmetry can be rewritten as

$$A_{PV}^p = \left[\frac{-G_F Q^2}{4\sqrt{2}\pi\alpha}\right].(A_V^p + A_s^p + A_A^p), \tag{5.43}$$

where A_V^p contains the proton's vector form factor excluding strangeness, A_s^p contains the proton's strangeness vector form factor and A_A^p contains the interference of the proton's magnetic vector and the axial-vector form factors. Explicitly, these components are written as

$$A_V^p = (1 - 4\sin^2\hat{\theta}_W) - \frac{\epsilon G_E^{\gamma,p} G_E^{\gamma,n} + \tau G_M^{\gamma,p} G_M^{\gamma,n}}{\epsilon (G_E^{\gamma,p})^2 + \tau (G_M^{\gamma,p})^2}, \tag{5.44}$$

$$A_s^p = -\frac{\epsilon G_E^{\gamma,p} G_E^s + \tau G_M^{\gamma,p} G_M^s}{\epsilon (G_E^{\gamma,p})^2 + \tau (G_M^{\gamma,p})^2} \tag{5.45}$$

and

$$A_A^p = \frac{-\epsilon'(1 - 4\sin^2\hat{\theta}_W) G_M^{\gamma,p} G_A^{e,p}}{\epsilon (G_E^{\gamma,p})^2 + \tau (G_M^{\gamma,p})^2}. \tag{5.46}$$

Analogously, A_{PV}^n can be obtained through the replacement of $G_{E,M}^{\gamma p}$ and G_A^{ep} by $G_{E,M}^{\gamma n}$ and G_A^{en}, respectively.

As mentioned previously, A_{PV}^p depends on both Q^2 and θ. For fixed Q^2, at a very forward scattering angles limit ($\theta \to 0; \epsilon \to 1$) the axial A_A component disappears ($\epsilon' \to 0$) and A_{PV}^p can be reduced to

$$A_{PV}^p = \left[\frac{-G_F Q^2}{4\sqrt{2}\pi\alpha}\right] . \Big((1 - 4\sin^2\hat{\theta}_W) - \frac{G_E^{\gamma,p} G_E^{\gamma,n} + \tau G_M^{\gamma,p} G_M^{\gamma,n}}{(G_E^{\gamma,p})^2 + \tau (G_M^{\gamma,p})^2} - \frac{G_E^{\gamma,p} G_E^s + \tau G_M^{\gamma,p} G_M^s}{(G_E^{\gamma,p})^2 + \tau (G_M^{\gamma,p})^2}\Big). \tag{5.47}$$

At very backward scattering angles limit ($\theta \to \pi; \epsilon \to 0$ and $\epsilon' \to \sqrt{\tau(1+\tau)}$) A_{PV}^p becomes

$$A_{PV}^p = \left[\frac{-G_F Q^2}{4\sqrt{2}\pi\alpha}\right] . \Big((1 - 4\sin^2\hat{\theta}_W) - \frac{G_M^{\gamma,n}}{G_M^{\gamma,p}} - \frac{G_M^s}{G_M^{\gamma,p}} - \frac{\sqrt{\tau(1+\tau)}(1 - 4\sin^2\hat{\theta}_W) G_A^{e,p}}{\tau G_M^{\gamma,p}}\Big). \tag{5.48}$$

In a case where the squared momentum transfer Q^2 is small, nucleon structure is suppressed and the parity-violating asymmetry is sensitive to the proton's weak charge. Therefore, A_{PV}^p is significantly simplified as

$$A_{PV}^p = \left[\frac{-G_F Q^2}{4\sqrt{2}\pi\alpha}\right] .(1 - 4\sin^2\hat{\theta}_W). \tag{5.49}$$

The Q_{weak} experiment has been conducted at the value of $Q^2 = 0.025$ GeV^2 to determine the weak charge of the proton, the world's first determination of the proton's weak charge [4]. The level of precision required by this experiment necessitates the inclusion of the electroweak radiative corrections.

These corrections, which generate from higher-order electroweak interactions, are also required for precision strangeness determinations.

5.2.2 Electroweak Radiative Corrections to the Neutral Current

Thus far, the tree-level contributions (one boson exchange, γ or Z^0) in e–N scattering have been considered. However, the neutral weak vector and axial vector form factors derived at this level require corrections due to higher order electroweak processes to precisely extract contributions from $G^s_{E,M}$ to A_{PV}. These higher-order corrections (radiative corrections) alter the weak vector and axial charges, g_V and g_A, that appear, for example, in Eqs. (5.25) and (5.29) and, consequently, in the expression of A_{PV}.

In the e–N scattering event, the radiative corrections arise because of the exchange of two vector bosons (γ, Z^0 and $W^{\pm}$) in the same scattering channel, for example, γZ box ($\Box_{\gamma Z}$) diagram shown in Fig. 5.2. These corrections can be categorised into one-quark processes, which reflect scattering involving only a single quark at a time, and many-quark processes, which involve electroweak interactions between target quarks (anapole correction). The radiative corrections also stem from ignoring the heavy quark (c, b and t) contributions to the decomposition of neutral weak form factors into quark form factors, where the three lightest quark flavours were considered.

Following the SM notation, these corrections are usually encoded in the R-factor [10]

$$R = R_{\text{one-quark}} + R_{\text{anapole}} + R_{\text{heavy quarks}}. \tag{5.50}$$

The heavy quark corrections have been calculated and were found to be $\sim 10^{-4}$ for the vector term and $\sim 10^{-2}$ for the axial term, and are therefore neglected in the radiative corrections [1].

The most widely used definition of the weak mixing angle $\sin^2\theta_W(\mu)$ is derived from the $\overline{\text{MS}}$ renormalisation scheme [27]. In this scheme, the weak mixing angle has a dependence on a renormalisation mass or energy μ. The weak mixing angle in the $\overline{\text{MS}}$ renormalisation scheme at Z boson's mass, $\sin^2\hat{\theta}_W$, which appears in the expression of A_{PV}, is used in this work and its value is taken from [15]. Electroweak calculations within different renormalisation schemes will differ slightly since these calculations are only accomplished up to finite order of perturbation theory.

The vector and axial-vector charges at tree level and with radiative correction R-factors in the SM are provided explicitly in Table 5.1 [10]. After including the radiative corrections, the proton's neutral weak and axial-vector form factors, Eq. (5.25) and (5.29), become

$$\begin{aligned} G_{E,M}^{Zp} &= (1-4\sin^2\hat{\theta}_W)(1+R_V^p)G_{E,M}^{\gamma p} - (1+R_V^n)G_{E,M}^{\gamma n} - (1+R_V^{(0)})G_{E,M}^s, \\ G_A^{ep} &= \Big[-(1+R_A^{T=1})G_A^{(3)} + \sqrt{3}R_A^{T=0}G_A^{(8)} + (1+R_A^{(0)})G_A^s\Big]G_A^D(Q^2), \end{aligned} \tag{5.51}$$

where the factors R_V^p, R_V^n and $R_V^{(0)}$ reflect the electroweak radiative corrections for vector proton, neutron and $SU(3)$-singlet amplitudes, respectively. $R_A^{T=1}$, $R_A^{T=0}$ and $R_A^{(0)}$ describe the axial-vector electroweak radiative corrections for the isovector, isoscalar, and $SU(3)$-singlet amplitudes. Note that the ratio $R_A^{T=0}$ vanishes at tree level as was discussed above.

5.2.2.1 One-Quark Corrections

As indicated previously, the one-quark corrections to the leading order e–N scattering arise from the scattering that proceeds via the exchange of two vector bosons and only a single quark is involved in the process.

The box radiative corrections involving only weak bosons, i.e., $\Box_{ZZ}$ and $\Box_{WW}$ diagrams, can be perturbatively calculated. For low-energy regions, where the theory is nonperturbative, these two corrections are suppressed [30]. These two diagrams render corrections to the weak charge of the proton (Eq. (7.3)) and are encoded in R_V^p as will be discussed latter.

Recently, $\Box_{\gamma Z}$ corrections have been considered and has been shown that these corrections have a significant energy dependence [6, 7, 156–159]. Focusing on the vector component of γZ box corrections, $\Re e\Box_{\gamma Z}^V$, the most accurate method to calculate these corrections is a dispersion relation [6]. The dispersion relation calculations of these corrections have been improved at forward scattering angles, whereas these corrections are unknown at backward scattering angles where the dispersion relation is not valid. Estimates for the Q^2-dependence of the $\Box_{\gamma Z}$ correction will be discussed in Section 6.1.

Two Feynman diagrams of one-quark processes that cause corrections to the tree-level weak couplings are depicted in Fig. 5.2. Here, the process on the left γZ mixing diagram represents corrections to the propagators, and the process on the right γZ box diagram indicates the exchange of the two bosons γ and Z^0 with an

Table 5.1: The vector (upper half) and axial-vector (lower half) charges at tree level and with the radiative correction R-factors in the Standard Model.

	Tree Level	Radiative Corrections Included
g_V^p	$1-4\sin^2\hat{\theta}_W$	$(1-4\sin^2\hat{\theta}_W)(1+R_V^p)$
g_V^n	-1	$-(1+R_V^n)$
$g_V^{(0)}$	-1	$-(1+R_V^{(0)})$
$g_A^{T=1}$	-1	$-(1+R_A^{T=1})$
$g_A^{T=0}$	0	$\sqrt{3}R_A^{T=0}$
$g_A^{(0)}$	1	$1+R_A^{(0)}$

excitation of intermediate hadronic states. The effective coupling constants C_{1q} and C_{2q} that describe the weak interaction are given at tree level as

$$C_{1q}=\frac{g_V^q g_A^e}{-2}, \quad C_{2q}=\frac{g_A^q g_V^e}{-2}, \tag{5.52}$$

where the expressions of $g_V^{q,e}$ and $g_A^{q,e}$ have been provided in Table 2.2.

The SM predictions for these effective coupling constants [15] are presented in Table 5.2. These predictions consider several vertex and box corrections.

To obtain the estimated values of R_V and R_A, as shown in Table 5.3, one can write explicitly

$$\begin{aligned}
g_V^p &= -2(2C_{1u}+C_{1d}) = (1-4\sin^2\theta_W)(1+R_V^p),\\
g_V^n &= -2(C_{1u}+2C_{1d}) = -(1+R_V^n),\\
g_V^{(0)} &= -2(C_{1u}+2C_{1d}) = -(1+R_V^{(0)}),\\
g_A^{T=1} &= \frac{C_{2u}-C_{2d}}{1-4\sin^2\theta_W} = -(1+R_A^{T=1}),\\
g_A^{T=0} &= \frac{2\sqrt{3}(C_{2u}+C_{2d})}{1-4\sin^2\theta_W} = \sqrt{3}R_A^{T=0},\\
g_A^{(0)} &= \frac{2(C_{2u}+2C_{2d})}{1-4\sin^2\theta_W} = 1+R_A^{(0)},
\end{aligned} \tag{5.53}$$

and make use of the SM predictions presented in Table 5.2.

At low momentum transfers, the one-quark corrections for the vector weak form factors have a weak Q^2-dependence and are considered to be constant [10].

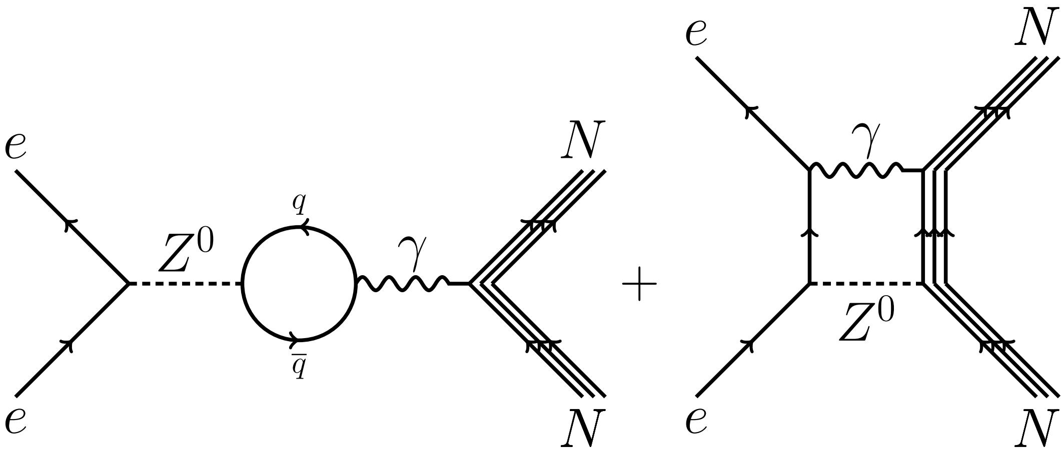

Figure 5.2: Two Feynman diagrams of one-quark processes that cause corrections to the tree-level weak couplings. The process on the left γZ^0 mixing diagram with $q\overline{q}$ loop represents corrections to the propagators. The process on the right γZ^0 box diagram indicates the exchange of the two bosons γ and Z^0.

Table 5.2: The SM predictions for the effective couplings C_{1q} and C_{2q} and their values at tree level [15].

	Tree Level	SM Predictions
C_{1u}	−0.1916	−0.1887
C_{1d}	0.3458	0.3419
C_{2u}	−0.0374	−0.0351
C_{2d}	0.0374	0.0247

5.2.2.2 Axial Form Factor and the Anapole Moment

Electroweak radiative corrections associated with the anapole moment are referred to as many-quark corrections. The anapole corrections occur because of the axial-vector coupling of the photon to the nucleon [160]. Here, the photon couples to currents of two or more quarks inside the nucleon via weak bosons exchange. A representative Feynman diagram for many-quark corrections is presented in Fig. 5.3.

The renowned calculations of the anapole corrections achieved by Zhu *et al.* in [160] have been performed in the on-shell renormalisation (OSR) scheme using BChPT. Since the radiative corrections in the previous section are estimated in the $\overline{\text{MS}}$ scheme, these anapole radiative corrections must be transformed to $\overline{\text{MS}}$ via

$$\frac{R_{\overline{\text{MS}}}}{R_{\text{OSR}}} = \frac{1 - 4\sin^2\theta_W}{1 - 4\sin^2\hat{\theta}_W} = 1.44, \tag{5.54}$$

Table 5.3: The values of the ratios R_V and R_A (one-quark corrections).

	Value
R_V^p	$-0.0513(40)$
R_V^n	$-0.0098(3)$
$R_V^{(0)}$	$-0.0098(3)$
$R_A^{T=1}$	-0.201
$R_A^{T=0}$	-0.278
$R_A^{(0)}$	-0.618

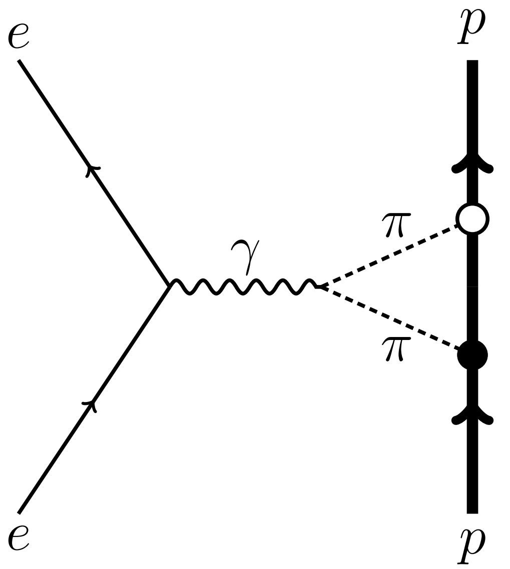

Figure 5.3: A Feynman diagram for many-quark electroweak radiative corrections (anapole corrections) to e–p scattering. The filled and opened circles indicate the parity-violating and parity-conserving pion-nucleon vertex, respectively.

where $\sin^2\theta_W = 0.2230$ in OSR [160] and $\sin^2\hat{\theta}_W = 0.23129$ in $\overline{\text{MS}}$ [15]. Therefore, the transformation of the anapole correction between the two renormalisation schemes reads as

$$R^{T=1,0}_{A(\text{ana}),\overline{\text{MS}}} = 1.44 R^{T=1,0}_{A(\text{ana}),\text{OSR}}. \tag{5.55}$$

The anapole corrections in the OSR [160] and $\overline{\text{MS}}$ schemes using Eq. (5.55) are given explicitly in Table 5.4. In regards to the large uncertainties in Table 5.4, the authors of [160] considered only the dominant virtual hadronic states that cause anapole corrections, and hence they assigned significant theoretical uncertainties to reflect the contributions from a large number of virtual hadronic states that can also give rise to the anapole effects.

The anapole corrections of $R_A^{(0)}$ have not been calculated. As treated in the

Table 5.4: The anapole corrections in the OSR [160] and $\overline{\text{MS}}$ schemes using Eq. (5.55).

	OSR scheme	$\overline{\text{MS}}$ scheme
$R^{T=1}_{A(\text{ana})}$	-0.06 ± 0.24	-0.0865 ± 0.3463
$R^{T=0}_{A(\text{ana})}$	0.01 ± 0.14	0.0144 ± 0.2020

literature, the anapole corrections for $R_A^{(0)}$ have been set to zero and the value of the one-quark correction for $R_A^{(0)}$ has been assigned as its uncertainty.

The axial form factor, including anapole corrections, can be given by [161]

$$G_A^{e,N} = \Big[-(1+R_A^{T=1})G_A^{(3)}\tau_3 + \sqrt{3}R_A^{T=0}G_A^{(8)} + (1+R_A^{(0)})G_A^s + A^N_{\text{ana}}\Big] G_A^D(Q^2), \quad (5.56)$$

where the anapole contribution term A^N_{ana} can be written as

$$A^N_{\text{ana}} = (R^{T=1}_{A(\text{ana})}\tau_3 + R^{T=0}_{A(\text{ana})})G_A^{(3)}. \quad (5.57)$$

The axial term A_A^p (defined in Eq. (5.46)) is suppressed by $(1-4\sin^2\hat{\theta}_W)$ and it is further suppressed by ϵ' at forward angles.

The present work considers that the axial-vector form factor implicitly incorporates the axial radiative and hadronic anapole corrections, where this entire contribution is to be fit to data. Therefore, this analysis uses the effective axial form factor $\tilde{G}_A^N$ and the axial-vector component A_A^p becomes

$$A_A^p = \frac{-\epsilon'(1-4\sin^2\hat{\theta}_W)G_M^{\gamma,p}\tilde{G}_A^p}{\epsilon(G_E^{\gamma,p})^2 + \tau(G_M^{\gamma,p})^2}, \quad (5.58)$$

where $\tilde{G}_A^{p,n}$ is defined as

$$\tilde{G}_A^{p,n} = \frac{\tilde{g}_A^{p,n}}{\left(1+\frac{Q^2}{M_A^2}\right)^2}, \quad (5.59)$$

The normalisation $\tilde{g}_A^{p,n}$ represent the entire axial radiative and anapole corrections that will be fit to the data, however since the isoscalar combination is poorly determined, the theoretical estimate based on an effective field theory with VMD models [160] is employed in the present work to constrain this combination as will be discussed in Chapter 6. The momentum dependence of the isoscalar $R_A^{T=0}$ and isovector $R_A^{T=1}$ one-quark and anapole radiative corrections is assumed to be described by Eq. 5.59 where the axial dipole mass is selected to be that estimated from neutrino scattering, $M_A = 1.026$ GeV [162].

5.2.3 A^p_{PV} and A^n_{PV} with Electroweak Radiative Corrections

At this point of the discussion, it is appropriate to explicitly write the PV asymmetry for both the proton and neutron including the electroweak radiative corrections:

$$A^p_{PV} = \left[\frac{-G_F Q^2}{4\sqrt{2}\pi\alpha}\right].(A^p_V + A^p_s + A^p_A), \tag{5.60}$$

where

$$A^p_V = (1 - 4\sin^2\hat{\theta}_W)(1 + R^p_V) - (1 + R^n_V)\frac{\epsilon G^{\gamma,p}_E G^{\gamma,n}_E + \tau G^{\gamma,p}_M G^{\gamma,n}_M}{\epsilon (G^{\gamma,p}_E)^2 + \tau (G^{\gamma,p}_M)^2}, \tag{5.61}$$

$$A^p_s = -(1 + R^{(0)}_V)\frac{\epsilon G^{\gamma,p}_E G^s_E + \tau G^{\gamma,p}_M G^s_M}{\epsilon (G^{\gamma,p}_E)^2 + \tau (G^{\gamma,p}_M)^2} \tag{5.62}$$

and

$$A^p_A = \frac{-\epsilon'(1 - 4\sin^2\hat{\theta}_W) G^{\gamma,p}_M \tilde{G}^p_A}{\epsilon (G^{\gamma,p}_E)^2 + \tau (G^{\gamma,p}_M)^2}. \tag{5.63}$$

A^n_{PV} can be obtained by using $G^{\gamma n}_{E,M}$ and $\tilde{G}^n_A$ instead of $G^{\gamma p}_{E,M}$ and $\tilde{G}^p_A$, respectively.

5.3 Helium-4 and Deuteron PV Asymmetries

This work aims to perform a global analysis of the full set of PV asymmetries from elastic e–helium-4 scattering and quasielastic e–deuteron scattering at low Q^2 in addition to elastic e–p scattering,. In this section, the PV asymmetry structure for helium-4 (^{4}He) and deuteron (d) will be briefly highlighted.

The ^{4}He nucleus is spin-0, parity even and isoscalar. Elastic electron scattering from ^{4}He is a pure isoscalar, $0^+ \rightarrow 0^+$, transition and therefore allows no contributions from magnetic or axial-vector currents. Thus, the elastic e-^{4}He scattering has been utilised to directly extract the strange electric form factor.

For ^{4}He, the PV asymmetry based on the assumption that isospin mixing can be neglected is written as [10]

$$A^{He}_{PV} = -\left[\frac{G_F Q^2}{4\sqrt{2}\pi\alpha}\right].\left[(1 - 4\sin^2\theta_{\rm w})(1 + R^p_V) - (1 + R^n_V) \right. \tag{5.64}$$
$$\left. + 2\frac{-(1 + R^{(0)}_V)G^s_E}{G^{\gamma,p}_E + G^{\gamma,n}_E}\right].$$

The isospin correction will be taken into account in Chapter 6.

The quasielastic interaction with the constituents of nucleon dominates the scattering from the deuteron. The situation for quasielastic scattering from a nuclear target is intricate because of the nuclear structure, final state interactions, off-shell effects, etc. [10]. These impacts are considered in the analysis presented in Chapter 6.

The PV asymmetry in electron-deuteron quasielastic scattering in the static approximation, where the proton and neutron in the deuteron are assumed to be noninteracting particles, is given by [10]

$$A_{PV}^d = \frac{\Big(\epsilon(G_E^{\gamma,p})^2 + \tau(G_M^{\gamma,p})^2\Big)A_{PV}^p + \Big(\epsilon(G_E^{\gamma,n})^2 + \tau(G_M^{\gamma,n})^2\Big)A_{PV}^n}{\epsilon\Big((G_E^{\gamma,p})^2 + (G_E^{\gamma,n})^2\Big) + \tau\Big((G_M^{\gamma,p})^2 + (G_M^{\gamma,n})^2\Big)}. \tag{5.65}$$

Note that, in this approximation, the quasielastic cross section is presented as a non-coherent sum over the nucleons. It is instructive to write A_{PV}^d explicitly using the A_{PV}^p and A_{PV}^n expressions:

$$A_{PV}^d = \left[\frac{-G_F Q^2}{4\sqrt{2}\pi\alpha}\right].(A_V^d + A_s^d + A_A^d), \tag{5.66}$$

where

$$A_V^d = (1-4\sin^2\hat{\theta}_W)(1+R_V^p) - \frac{2(1+R_V^n)(\epsilon G_E^{\gamma,p}G_E^{\gamma,n} + \tau G_M^{\gamma,p}G_M^{\gamma,n})}{\epsilon\Big((G_E^{\gamma,p})^2 + (G_E^{\gamma,n})^2\Big) + \tau\Big((G_M^{\gamma,p})^2 + (G_M^{\gamma,n})^2\Big)}, \tag{5.67}$$

$$A_s^d = -(1+R_V^{(0)})\frac{\epsilon(G_E^{\gamma,p} + G_E^{\gamma,n})G_E^s + \tau(G_M^{\gamma,p} + G_M^{\gamma,n})G_M^s}{\epsilon\Big((G_E^{\gamma,p})^2 + (G_E^{\gamma,n})^2\Big) + \tau\Big((G_M^{\gamma,p})^2 + (G_M^{\gamma,n})^2\Big)} \tag{5.68}$$

and

$$A_A^d = \frac{-\epsilon'(1-4\sin^2\hat{\theta}_W)(G_M^{\gamma,p}\tilde{G}_A^p + G_M^{\gamma,n}\tilde{G}_A^n)}{\epsilon\Big((G_E^{\gamma,p})^2 + (G_E^{\gamma,n})^2\Big) + \tau\Big((G_M^{\gamma,p})^2 + (G_M^{\gamma,n})^2\Big)}. \tag{5.69}$$

As can be noted, combining proton and deuteron data renders two independent anapole form factors. The present analysis aims to extract all four form factors, i.e., two strange form factors and two anapole form factors, by performing a global analysis of all experimental data from elastic PV electron scattering up to $Q^2 \sim 1$ GeV^2.

5.4 Experimental Measurements of G_M^s and G_E^s

The first measurement of A_{PV} from scattering polarised electrons from deuterium and hydrogen was conducted in 1978 at SLAC [163]. This measurement played an important role in establishing and understanding the nature of electroweak unification. Although the authors of [163] measured A_{PV} in deep inelastic scattering, this experimental study established experimental techniques that allowed for many asymmetry measurements involving scattered polarised electrons from various polarised and unpolarised targets at different kinematic conditions.

Table 5.5 summarises the world data of PV elastic electron scattering within the range of Q^2 considered in the present work, including the targets, kinematics and measured asymmetry. The targets p, ^{4}He and d indicate electron scattering from the proton, helium-4 and deuteron, respectively. The measured asymmetry is represented by A^{phys} and its associated uncertainty is shown by δA, where the statistic and systematic errors have been added in quadrature. The correlated systematic error in the G0 experiment is shown by δA_{cor}. The measured asymmetry A^{phys} and the corresponding uncertainty are in units of ppm.

Based on the kinematic conditions, the experiments are sensitive to G_M^s, G_E^s and $G_A^{e(T=1)}$. The Singlet Anomalous Moment of the Proton using Longitudinally Polarized Electrons (SAMPLE) measurements are sensitive to G_M^s and $G_A^{e(T=1)}$ since they were conducted at large scattering angles. For forward-angle scattering from the proton, the Hall A proton parity experiment (HAPPEx), PVA4, G0 and Qweak measurements are sensitive to linear combinations of the electric and magnetic strange form factors. The HAPPEx measurements from elastic scattering from ^{4}He are sensitive to G_E^s.

Table 5.5: A summary of the measured PV asymmetries data considered in this work from different experiments with varying kinematics, where Q^2, θ and E are the squared four-momentum transfer, scattering angle and beam energy, respectively. A^{phys} and δA are the measured asymmetry and the corresponding uncertainty, respectively, where the statistic and systematic errors have been added in quadrature. δA_{cor} is the correlated error in the G0 experiment [164, 165].

Experiment	Target	Q^2	θ	E	A^{phys}	δA	δA_{cor}	Ref.
Qweak	p	0.025	7.90	1.16	-0.2265	0.0093	0	[4]
SAMPLE	d	0.038	144	0.11	-3.51	0.81	0	[166]
HAPPEx	^{4}He	0.077	6.0	2.67	6.40	0.26	0	[167]
SAMPLE	d	0.091	144	0.18	-7.77	1.03	0	[166]
HAPPEx	^{4}He	0.091	6.0	2.91	6.72	0.87	0	[168]
HAPPEx	p	0.099	6.0	3.03	-1.14	0.25	0	[169]
SAMPLE	p	0.1	144	0.2	-5.61	1.11	0	[170]
PVA4	p	0.108	35.4	0.57	-1.36	0.32	0	[171]
HAPPEx	p	0.109	6.0	3.18	-1.58	0.13	0	[167]
G0	p	0.122	6.68	3.03	-1.51	0.49	0.18	[164]
G0	p	0.128	6.84	3.03	-0.97	0.46	0.17	[164]
G0	p	0.136	7.06	3.03	-1.30	0.45	0.17	[164]
G0	p	0.144	7.27	3.03	-2.71	0.47	0.18	[164]
G0	p	0.153	7.5	3.03	-2.22	0.51	0.21	[164]
G0	p	0.164	7.77	3.03	-2.88	0.54	0.23	[164]
G0	p	0.177	8.09	3.03	-3.95	0.50	0.20	[164]
G0	p	0.192	8.43	3.03	-3.85	0.53	0.19	[164]
G0	p	0.210	8.84	3.03	-4.68	0.54	0.21	[164]
PVA4	p	0.22	144.5	0.31	-17.23	1.21	0	[172]
G0	p	0.221	110	0.35	-11.25	0.9	0.43	[165]
G0	d	0.221	110	0.35	-16.93	0.91	0.21	[165]
PVA4	d	0.224	145.0	0.31	-20.11	1.35	0	[173]
PVA4	p	0.230	35.3	0.85	-5.44	0.60	0	[174]
G0	p	0.232	9.31	3.03	-5.27	0.59	0.23	[164]
G0	p	0.262	9.92	3.03	-5.26	0.53	0.17	[164]
G0	p	0.299	10.63	3.03	-7.72	0.80	0.35	[164]
G0	p	0.344	11.45	3.03	-8.40	1.09	0.52	[164]
G0	p	0.410	12.59	3.03	-10.25	1.11	0.55	[164]
HAPPEx	p	0.477	12.3	3.35	-15.05	1.13	0	[175]
G0	p	0.511	14.2	3.03	-16.81	1.73	1.50	[164]
HAPPEx	p	0.624	13.7	3.48	-23.8	0.86	0	[176]
G0	p	0.628	110	0.68	-45.9	2.53	1.0	[165]
G0	d	0.628	110	0.68	-55.5	3.86	0.7	[165]
G0	p	0.631	15.98	3.03	-19.96	1.69	1.31	[164]
G0	p	0.788	18.16	3.03	-30.80	3.22	2.59	[164]
G0	p	0.997	20.9	3.03	-37.90	11.53	0.52	[164]

Chapter 6

Determination of Strangeness Form Factor

The strangeness content of the proton acts as a background role in the interpretation of the precision of the Q_{weak} collaboration measurement. The Q_{weak} collaboration favoured the determination of Q_W^p from a PVES fit over using the theoretical strangeness determination from lattice QCD or using the Q_{weak} datum by itself [4].

Having highlighted the formalism of the PV asymmetries of the nucleon, helium-4 and deuteron in Chapter 5, this chapter serves to illustrate the process of the analysis of the set of all available PVES data, up to the currently available limit of $Q^2 \sim 1\text{GeV}^2$ to determine the form factor strange quark content.

In general, the strangeness contributions to the EM form factors of the proton are ideal quantities to study the role of hidden flavour in the properties of the proton. This has motivated intense experimental measurements of these form factors. A major remaining source of systematic uncertainty in these determinations is the assumption that charge symmetry violation (CSV) is negligible. In the present work, a recent determination of the CSV form factors from LQCD, as well as estimates provided by chiral perturbation theory with resonance saturation, are used and the set of PVES data considered here are reanalysed.

Leading electroweak corrections play a significant role in precision measurements of the strangeness contribution to the nucleon form factors. An energy-dependent correction arising from the γZ box diagram was highlighted by Gorchtein and Horowitz [6]. The size of this correction is particularly significant to the Standard Model test by the Q_{weak} Experiment. Fortunately, the uncertainties arising from the underlying γZ interference structure functions can be reliably constrained [7]. The corrections reported by the constrained Adelaide-Jefferson Lab-Manitoba (AJM) [7], which will be closely revisited in Chapter 7, updated with the improved constraints of quark-hadron duality [177] and a momentum dependence as proposed in [158] have been incorporated.

This chapter begins with $\Box_{\gamma Z}(E)$ corrections with the aim of correcting the measured PV proton asymmetry A^{phys} at forward angles. The remainder of this chapter is devoted to the extraction of strangeness form factors from a global analysis of the PV asymmetry data with and without the constraint of CSV form factors.

6.1 The $\Box_{\gamma Z}$ Correction

As indicated above, the corrections due to higher-order electroweak processes are necessary for a precise interpretation of the measured PV asymmetry. The measured PV asymmetry A^{phys} for the proton at forward angles shown in Table 5.5 needs to be corrected for the energy-dependent part of the $\Box_{\gamma Z}$ and its uncertainty.

The $\Box_{\gamma Z}$ corrections arise from the interference γZ box diagram. Incorporating these corrections leads to a modification of the first term in Eq. (5.61) as

$$\left(1 - 4\sin^2\hat{\theta}_W\right)\left(1 + R_V^p\right) \to \left(1 - 4\sin^2\hat{\theta}_W\right)\left(1 + R_V^p\right) + \Box_{\gamma Z}(E). \tag{6.1}$$

The last term of Eq. (6.1) will be defined formally in Chapter 7.

The correction $\Box_{\gamma Z}$ is decomposed into an axial-vector electron, vector hadron component $\Box_{\gamma Z}^V$ and a vector electron, axial-vector hadron component $\Box_{\gamma Z}^A$:

$$\Box_{\gamma Z}(E) = \Box_{\gamma Z}^A(E) + \Box_{\gamma Z}^V(E). \tag{6.2}$$

As the electron energy E goes to 0, the hadronic vector correction $\Box_{\gamma Z}^V(E = 0)$ vanishes, and the hadronic axial-vector correction $\Box_{\gamma Z}^A(E = 0)$ dominates. The latter correction is encoded in R_V^p.

Blunden *et al.* [159] presented a formulation based on dispersion relations to calculate $\Box_{\gamma Z}^A(E)$ and they found, by considering all intermediate states, that $\Re e\Box_{\gamma Z}^A(E = 0) = 0.0044(4)$ and $\Re e\Box_{\gamma Z}^A(E = 1.165) = 0.0037(4)$, where $E = 1.165$ GeV is the Q_{weak} beam energy. The former value is connected to the pioneering work of Marciano and Sirlin who obtained $\Re e\Box_{\gamma Z}^A(E = 0) = 0.0052(5)$ [178, 179], where the low-energy part of loop is approximated by the elastic proton contribution, and the dominant high-energy part by the interaction with free quarks.

The calculations of Blunden *et al.* show that $\Box_{\gamma Z}^A(E)$ has a weak E-dependence. Therefore, the value of $\Box_{\gamma Z}^A = 0.0037(4)$ is adopted for the E range that is considered in the present work.

The dominant E-dependent radiative correction to A^{phys} is due to $\Box_{\gamma Z}^V(E)$. This correction has received considerable attention among the theory community. Recently Hall *et al.* [7] utilised the parton distribution functions to constrain the model-dependence of the interference structure functions and they obtained the most precise calculation of $\Box^V_{\gamma Z}(E)$. The update of that calculation with the improved constraints of quark-hadron duality [177] has been adopted here with the most recent input values.

In order to apply the γZ box corrections, the $\delta\Box_{\gamma Z}$ correction is defined as

$$\begin{aligned}\delta\Box_{\gamma Z} =& \Box_{\gamma Z}(E) - \Box_{\gamma Z}(0)\\ =& \Box^A_{\gamma Z}(E) + \Box^V_{\gamma Z}(E) - \Box_{\gamma Z}(0)\end{aligned} \tag{6.3}$$

where, as stated previously, $\Box^A_{\gamma Z}(E) = 0.0037(4)$ and $\Box_{\gamma Z}(0) = 0.0044(4)$. Thus, Eq. (6.1) becomes

$$\left(1 - 4\sin^2\hat{\theta}_W\right)\left(1 + R^p_V\right) \rightarrow \left(1 - 4\sin^2\hat{\theta}_W\right)\left(1 + R^p_V\right) + \delta\Box_{\gamma Z}. \tag{6.4}$$

With the updated $\Box^V_{\gamma Z}(E)$, the results of $\delta\Box_{\gamma Z}$ are presented in Table 6.1. The $\delta\Box_{\gamma Z}$ includes an additional correction for the Q^2-dependence, where the parameterisation of this dependence described in [158] has been used with the EM form factor parameterisations from [180]. Highlighting these form factor parameterisations will be presented in the next section.

With this modification, and from Eqs. (5.60) and (5.61), the measured PV asymmetries are corrected as

$$A^{phys}_{corr} = A^{phys} - \left[\frac{-G_F Q^2}{4\sqrt{2}\pi\alpha}\right]\delta\Box_{\gamma Z}. \tag{6.5}$$

The significance of the γZ box is somewhat less pronounced in the determination of strangeness. Nevertheless, for example, from Eq. 6.5, the correction makes about $\sim\frac{1}{2}$-sigma shift to the central value of the precise HAPPEX proton point at $Q^2 \sim 0.1$ GeV^2.

6.2 Parameterisation

A combined analysis of the world PV data from the proton, helium-4 and the deuteron requires a consistent treatment of the vector and axial form factors and radiative corrections. The theoretical asymmetry used in this analysis is written as

$$A_{Theory} = \eta_0 + \eta^p_A \tilde{G}^p_A + \eta^n_A \tilde{G}^n_A + \eta_E G^s_E + \eta_M G^s_M, \tag{6.6}$$

Table 6.1: The $\Re e\Box_{\gamma Z}^{V}(E)$ and $\delta\Box_{\gamma Z}$ corrections evaluated for the measured proton PV asymmetry A^{phys} at forward angles.

Experiment	Q^2 (GeV^2)	E (GeV)	$\Re e\Box_{\gamma Z}^{V}(E)$ ($\times10^{-3}$)	$\delta\Box_{\gamma Z}$ ($\times10^{-3}$)
Qweak	0.025	1.165	5.934 ± 0.382	5.120 ± 0.671
HAPPEx	0.099	3.030	8.780 ± 0.372	7.205 ± 0.701
PVA4	0.108	0.570	3.929 ± 0.289	2.843 ± 0.580
HAPPEx	0.109	3.180	8.947 ± 0.368	7.250 ± 0.713
G0	0.122	3.030	8.780 ± 0.372	6.969 ± 0.722
G0	0.128	3.030	8.780 ± 0.372	6.907 ± 0.728
G0	0.136	3.030	8.780 ± 0.372	6.825 ± 0.737
G0	0.144	3.030	8.780 ± 0.372	6.742 ± 0.745
G0	0.153	3.030	8.780 ± 0.372	6.648 ± 0.754
G0	0.164	3.030	8.780 ± 0.372	6.534 ± 0.766
G0	0.177	3.030	8.780 ± 0.372	6.398 ± 0.780
G0	0.192	3.030	8.780 ± 0.372	6.243 ± 0.795
G0	0.210	3.030	8.780 ± 0.372	6.056 ± 0.814
PVA4	0.230	0.850	5.198 ± 0.350	3.257 ± 0.610
G0	0.232	3.030	8.780 ± 0.372	5.831 ± 0.834
G0	0.262	3.030	8.780 ± 0.372	5.527 ± 0.859
G0	0.299	3.030	8.780 ± 0.372	5.161 ± 0.885
G0	0.344	3.030	8.780 ± 0.372	4.733 ± 0.905
G0	0.410	3.030	8.780 ± 0.372	4.143 ± 0.917
HAPPEx	0.477	3.350	9.123 ± 0.365	3.749 ± 0.943
G0	0.511	3.030	8.780 ± 0.372	3.340 ± 0.898
HAPPEx	0.624	3.480	9.251 ± 0.362	2.740 ± 0.881
G0	0.631	3.030	8.780 ± 0.372	2.547 ± 0.831
G0	0.788	3.030	8.780 ± 0.372	1.753 ± 0.706
G0	0.997	3.030	8.780 ± 0.372	1.038 ± 0.525

where for the proton

$$\eta_0^p = \left[\frac{-G_F Q^2}{4\sqrt{2}\pi\alpha}\right]\cdot\left[(1-4\sin^2\hat{\theta}_W)(1+R_V^p) - (1+R_V^n)\frac{\epsilon G_E^{\gamma,p}G_E^{\gamma,n} + \tau G_M^{\gamma,p}G_M^{\gamma,n}}{\epsilon(G_E^{\gamma,p})^2 + \tau(G_M^{\gamma,p})^2}\right], \tag{6.7}$$

$$\eta_E^p = \left[\frac{G_F Q^2}{4\sqrt{2}\pi\alpha}\right]\cdot\left[\frac{(1+R_V^{(0)})\epsilon G_E^{\gamma,p}}{\epsilon(G_E^{\gamma,p})^2 + \tau(G_M^{\gamma,p})^2}\right], \tag{6.8}$$

$$\eta_M^p = \left[\frac{G_F Q^2}{4\sqrt{2}\pi\alpha}\right]\cdot\left[\frac{(1+R_V^{(0)})\tau G_M^{\gamma,p}}{\epsilon(G_E^{\gamma,p})^2 + \tau(G_M^{\gamma,p})^2}\right], \tag{6.9}$$

$$\eta_A^p = \left[\frac{-G_F Q^2}{4\sqrt{2}\pi\alpha}\right]\cdot\left[\frac{(-1+4\sin^2\hat{\theta}_W)\epsilon' G_M^{\gamma,p}}{\epsilon(G_E^{\gamma,p})^2 + \tau(G_M^{\gamma,p})^2}\right], \tag{6.10}$$

while for ^{4}He

$$\eta_0^{He} = -\Big[\frac{G_F Q^2}{4\sqrt{2}\pi\alpha}\Big].\Big[(1-4\sin^2\hat{\theta}_W)(1+R_V^p) - (1+R_V^n)\Big], \tag{6.11}$$

$$\eta_E^{He} = -\Big[\frac{G_F Q^2}{4\sqrt{2}\pi\alpha}\Big].\Big[2\frac{-(1+R_V^{(0)})}{G_E^{\gamma,p}+G_E^{\gamma,n}}\Big], \tag{6.12}$$

and η_M^{He} and η_A^{He} are zero. In the case of the deuteron target, these coefficients (assuming static approximation) can be written as

$$\begin{aligned}\eta_0^d = \Big[\frac{-G_F Q^2}{4\sqrt{2}\pi\alpha}\Big]\Big[&(1-4\sin^2\hat{\theta}_W)(1+R_V^p) \\ &- \frac{2(1+R_V^n)(\epsilon G_E^{\gamma,p}G_E^{\gamma,n}+\tau G_M^{\gamma,p}G_M^{\gamma,n})}{\epsilon\Big((G_E^{\gamma,p})^2+(G_E^{\gamma,n})^2\Big)+\tau\Big((G_M^{\gamma,p})^2+(G_M^{\gamma,n})^2\Big)}\Big],\end{aligned} \tag{6.13}$$

$$\eta_E^d = \Big[\frac{G_F Q^2}{4\sqrt{2}\pi\alpha}\Big].\Big[\frac{(1+R_V^{(0)})\epsilon(G_E^{\gamma,p}+G_E^{\gamma,n})}{\epsilon\Big((G_E^{\gamma,p})^2+(G_E^{\gamma,n})^2\Big)+\tau\Big((G_M^{\gamma,p})^2+(G_M^{\gamma,n})^2\Big)}\Big], \tag{6.14}$$

$$\eta_M^d = \Big[\frac{G_F Q^2}{4\sqrt{2}\pi\alpha}\Big].\Big[\frac{(1+R_V^{(0)})\tau(G_M^{\gamma,p}+G_M^{\gamma,n})}{\epsilon\Big((G_E^{\gamma,p})^2+(G_E^{\gamma,n})^2\Big)+\tau\Big((G_M^{\gamma,p})^2+(G_M^{\gamma,n})^2\Big)}\Big], \tag{6.15}$$

$$\eta_A^{d,p} = \Big[\frac{-G_F Q^2}{4\sqrt{2}\pi\alpha}\Big].\Big[\frac{\epsilon'(-1+4\sin^2\hat{\theta}_W)G_M^{\gamma,p}}{\epsilon\Big((G_E^{\gamma,p})^2+(G_E^{\gamma,n})^2\Big)+\tau\Big((G_M^{\gamma,p})^2+(G_M^{\gamma,n})^2\Big)}\Big], \tag{6.16}$$

$$\eta_A^{d,n} = \Big[\frac{-G_F Q^2}{4\sqrt{2}\pi\alpha}\Big].\Big[\frac{\epsilon'(-1+4\sin^2\hat{\theta}_W)G_M^{\gamma,n}}{\epsilon\Big((G_E^{\gamma,p})^2+(G_E^{\gamma,n})^2\Big)+\tau\Big((G_M^{\gamma,p})^2+(G_M^{\gamma,n})^2\Big)}\Big], \tag{6.17}$$

where τ, ϵ and ϵ' have been defined in Eqs. (5.40), (5.41) and (5.42).

It has been noted that the strange form factors show a weak sensitivity to the selection of nucleon electromagnetic form factor parameterisations. Within the Q^2 range considered in this work, the central values of the nucleon EM form factor parameterisations presented by Ye *et al.* in [180] are used. In their analysis, the two-photon exchange has been incorporated. They performed a global fit within the z-expansion framework and the nucleon form factors' central values are presented as coefficients in the systematic z-expansion[1].

Table 6.2 represents the calculated coefficients η, presented in Eq. (6.6), which characterise the theoretical asymmetry for the experiments (in ppm). The nucleon form factor parameterisations provided in [180] and the values for the Standard Model radiative corrections in Table 5.3 have been used.

---

[1] The fit parameters of the nucleon form factors are provided in Appendix C.

In the case of the deuteron, it is essential that the nuclear effects on the parity-violating asymmetry and their impact on the accuracy of the extraction of the single nucleon form factors are quantified. The SAMPLE analysis of the deuteron measurements [154] has considered nuclear effects. Therefore, for these measurements, the η_0, η_M and η_E are taken from [154, 162, 166]. However, no such response functions are considered in the deuterium quasi-elastic results obtained from G0 [165] and PVA4 [173] measurements. Therefore, their coefficients η are calculated in the static approximation, i.e., Eqs. (6.13)-(6.17).

The uncertainties associated with the kinematical factors η are no more than 2% and hence have negligible effects on the current analysis and thus have been disregarded.

In order to extract the four form factors ($\tilde{G}_A^p$, $\tilde{G}_A^n$, G_E^s and G_M^s) that appear in Eq. (6.6) using the data set considered here, the Q^2-dependence of the strangeness form factors is parameterised by a Taylor expansion as will be highlighted in the next section. In this analysis, since the entire contribution is to be fit to data, the effective axial form factors $\tilde{G}_A^N$, which implicitly include both the axial radiative and anapole corrections, have been employed. For these form factors, the dipole form

$$\tilde{G}_A^N = \tilde{g}_A^N \left(1 + \frac{Q^2}{M_A^2}\right)^{-2} \tag{6.18}$$

has been used with the axial dipole mass $M_A = 1.026$ GeV determined from neutrino scattering [181], common to both proton and neutron form factors. The normalisations $\tilde{g}_A^{p,n}$ are fit to the data, however since the isoscalar combination is very poorly determined, theoretical esimates based on an effective field theory with vector-meson dominance models have been imposed to constrain this combination, ($\tilde{g}_A^p$ + $\tilde{g}_A^n$)/2= -0.08 ± 0.26 [160].

Sections 6.2.1 and 6.2.2 will describe the analysis under the assumption of exact charge symmetry. This provides a baseline with which one can explore the implications of charge symmetry violation in Section 6.3.

6.2.1 Taylor Expansion

At low momentum transfers, a Taylor series expansion in squared momentum transfer Q^2 is sufficient and minimises the model-dependence of the determined form factors [162]. The model-dependence of this expansion will be examined when z-expansion fit is considered in Section 6.2.2. In this analysis, the strange electric and magnetic form factors Q^2-dependence can be parameterised by a Taylor series expansion in Q^2 as

Table 6.2: The calculated coefficients η, presented in Eq. (6.6), which characterise the theoretical asymmetry for the experiments (in ppm). The squared four-momentum transfers Q^2 are in GeV^2, and the scattering angles are in degree.

Experiment	Target	Q^2	θ	η_0	η_E	η_M	η_A^p	η_A^n
Qweak	p	0.025	7.90	-0.216	2.279	0.046	0.006	0.000
SAMPLE	d	0.038	144.00	-2.130	1.160	0.280	0.460	-0.300
HAPPEx	^{4}He	0.077	6.00	6.366	16.582	0.000	0.000	0.000
SAMPLE	d	0.091	144.00	-7.020	1.630	0.770	1.040	-0.650
HAPPEx	^{4}He	0.091	6.00	7.523	20.223	0.000	0.000	0.000
HAPPEx	p	0.099	6.00	-1.412	9.539	0.758	0.037	0.000
SAMPLE	p	0.100	144.00	-5.495	2.113	3.453	1.569	0.000
PVA4	p	0.108	35.40	-1.820	10.070	1.050	0.259	0.000
HAPPEx	p	0.109	6.00	-1.629	10.575	0.925	0.043	0.000
G0	p	0.122	6.68	-1.931	11.939	1.172	0.057	0.000
G0	p	0.128	6.84	-2.076	12.575	1.296	0.063	0.000
G0	p	0.136	7.06	-2.276	13.431	1.473	0.072	0.000
G0	p	0.144	7.27	-2.484	14.294	1.662	0.082	0.000
G0	p	0.153	7.50	-2.725	15.275	1.889	0.093	0.000
G0	p	0.164	7.77	-3.033	16.485	2.190	0.108	0.000
G0	p	0.177	8.09	-3.412	17.933	2.577	0.128	0.000
G0	p	0.192	8.43	-3.871	19.626	3.068	0.153	0.000
G0	p	0.210	8.84	-4.450	21.688	3.722	0.187	0.000
PVA4	p	0.220	144.50	-13.315	2.880	11.133	3.466	0.000
G0	p	0.221	110.00	-10.615	9.372	8.933	2.729	0.000
G0	d	0.221	110.00	-15.246	7.630	2.211	2.051	-1.376
PVA4	d	0.224	145.00	-18.651	2.168	2.672	2.505	-1.680
PVA4	p	0.230	35.30	-5.785	22.455	5.082	0.882	0.000
G0	p	0.232	9.31	-5.199	24.252	4.620	0.234	0.000
G0	p	0.262	9.92	-6.288	27.822	6.026	0.308	0.000
G0	p	0.299	10.63	-7.729	32.333	8.062	0.416	0.000
G0	p	0.344	11.45	-9.614	37.967	11.012	0.577	0.000
G0	p	0.410	12.59	-12.605	46.499	16.342	0.874	0.000
HAPPEx	p	0.477	12.30	-15.820	55.646	23.000	1.133	0.000
G0	p	0.511	14.20	-17.606	60.111	27.011	1.489	0.000
HAPPEx	p	0.624	13.70	-23.540	76.587	42.758	2.118	0.000
G0	p	0.628	110.00	-36.914	19.714	62.247	11.913	0.000
G0	d	0.628	110.00	-50.722	16.632	14.624	8.456	-5.657
G0	p	0.631	15.98	-24.054	77.049	44.074	2.518	0.000
G0	p	0.788	18.16	-33.078	100.263	74.553	4.453	0.000
G0	p	0.997	20.90	-45.776	132.553	131.722	8.321	0.000

$$G_E^s(Q^2) = \rho_s Q^2 + \rho_s' Q^4, \tag{6.19}$$

$$G_M^s(Q^2) = \mu_s + \mu_s' Q^2. \tag{6.20}$$

In the language of chiral perturbation theory, the strange magnetic moment $\mu_s = G_M^s(Q^2 = 0)$ appears at chiral order p^2. The first Q^2-dependence in $G_M^s(Q^2)$, strange magnetic radius ($\mathcal{O}(p^4)$), can be evaluated by chiral loop contributions associated with the corresponding low-energy constant. However, the first Q^2-dependence in $G_E^s(Q^2)$, the electric strange radius, appears at order $\mathcal{O}(p^3)$, and the second Q^2-dependence arises at chiral order p^5.

Based on these considerations, this work performs a global fit at leading order (LO) terms of the strangeness form factor (Eqs. 6.19 and 6.20) with four parameters, $\tilde{g}_A^p$, $\tilde{g}_A^n$, μ_s and ρ_s, and at next-to-leading order (NLO) terms of the strangeness form factor with six parameters, i.e., μ_s' and ρ_s' in addition to the previous four parameters.

The χ^2 is calculated as

$$\chi^2 = \sum_i \sum_j (A_i^{phys} - A_i^{Theory})(V)_{ij}^{-1}(A_j^{phys} - A_j^{Theory}), \tag{6.21}$$

where A^{phys} represents the measured asymmetries in Table 5.5. Recall that the corrected measured PV asymmetries A_{corr}^{phys} for $\Box_{\gamma Z}$, Eq. (6.5), replace the measured PV asymmetries A^{phys} for proton at forward angles. A^{Theory} refers to the theoretical predictions obtained from the fit parameters. The indicies i and j run over the data ensemble. The matrix V represents the covariance error matrix defined as

$$(V)_{ij} = (\sigma_i^{uncor})^2 \delta_{ij} + \sigma_i^{cor} \sigma_j^{cor}, \tag{6.22}$$

where σ_i^{uncor} and $\sigma_{i,j}^{cor}$ are uncorrelated and correlated uncertainties of the i, j^{th}-measurement respectively (Table. 5.5). Note that the correlated uncertainties are only relevant for the G0 experiment, where the forward and backward data are treated as mutually independent.

The goodness of the fit is estimated from the reduced χ^2 as

$$\chi_{red}^2 = \chi^2/\text{d.o.f}, \tag{6.23}$$

with 33 and 31 degrees of freedom (d.o.f) for the LO and NLO fits, respectively. Note that with the isoscalar axial charge constrained, as described above, there are effectively 3 (5) fit parameters in the LO (NLO) fits.

In Fig. 6.1, the behaviour of evolution of μ_s and ρ_s with increasing the upper limit of Q^2 (increasing the number of data) for the LO and NLO fits is displayed. As can been seen, including the HAPPEX data point at $Q^2 = 0.624$ GeV^2 [176] has a significant effect. In particular, we note that the LO fit strangeness parameters' uncertainties have reduced significantly and the signs of the central values for the NLO fit have changed. Additionally, including the G0 data point at $Q^2 \sim 1$ GeV^2 [164] leads to a notable reduction in the uncertainties of the strangeness parameters from the NLO fit.

The leading order fit results for the Taylor expansion form factor fit without constraints from CSV are presented in Table 6.3, with comparisons against previous PVES global fits [29, 162, 182, 183]. The results are compatible with earlier work, though with significantly reduced uncertainty.

While the fit quality is reasonable, these simple leading order fits are certainly anticipated to be too simple to describe these form factors over the full range $0 \leq Q^2 \lesssim 1.0$ GeV^2. As a result, the statistical uncertainties displayed are not representative of the current knowledge of the strange form factors. Hence, more variation in the Q^2-dependence by extending the fits to next-leading order is considered, i.e., Eqs. (6.19) and (6.20). Results are shown in Table 6.4. Curiously, the additional fit parameters are unable to make significant improvement to the χ^2 and the reduced χ^2 very marginally increases for the NLO fit.

Although the data do not support any structure offered by the NLO fits, the results at this order are treated as being better representative of the uncertainties of the strangeness form factors, while offering some degree of smoothing of the underlying data. With noting that given the clustering of the underlying data set, the separation of the electric and magnetic strange form factors are most reliable only at the discrete momentum transfers near $Q^2 \sim 0.1$, 0.2 and 0.6 GeV^2. As such, the NLO fits are roughly fitting 3 data points with 2 parameters for each form factor. Attempting fits at even higher order will just amount to over-fitting the statistical fluctuations of the data set.

The extraction of the strange form factors over the current Q^2 domain is shown in Fig. 6.2, which displays a notable constraint on G_M^s around $Q^2 \sim 0.65$ GeV^2. Furthermore, a comparison with recent theoretical lattice QCD results is shown in Fig. 6.2, where the green square corresponds to the result of $G_M^s(Q^2 = 0.1 \text{ GeV}^2)$ from [151] and the magenta squares represent the G_M^s and G_E^s at different values of $Q^2 = 0.17,\ 0.62$ and 0.88 GeV^2 from [148]. The authors of [151] report a direct determination of the strange electromagnetic form factors including at the physical pion mass. In addition, they performed a model-independent extraction of the strange magnetic moment and strange electric radius. Here, an excellent agreement between strangeness determinations based on PVES data and lattice QCD results over the full Q^2 range is observed. These determinations are also compatible with

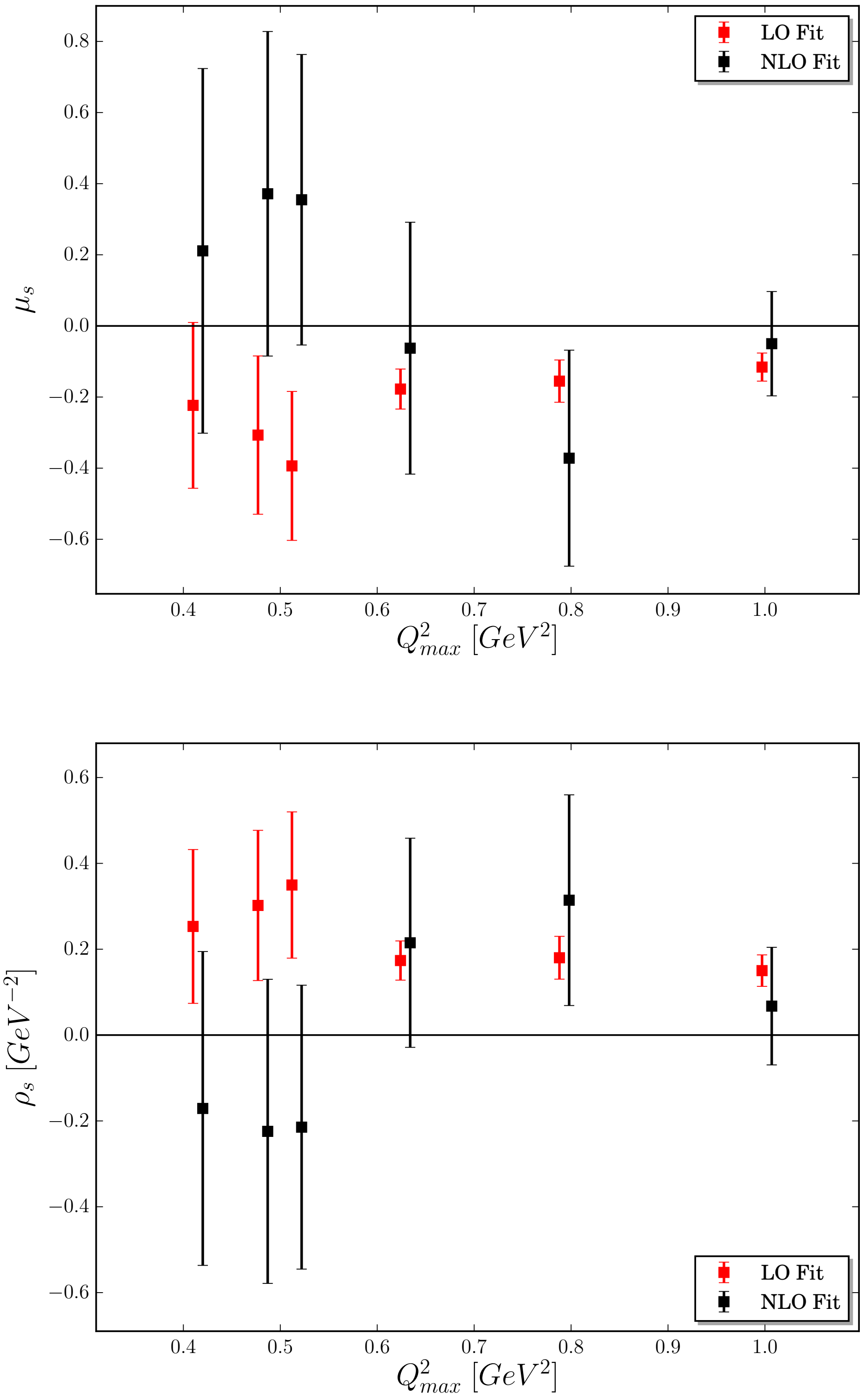

Figure 6.1: Shown are μ_s and ρ_s parameters values obtained from the LO (red square) and NLO (black square) fits at different maximum values of Q^2. The error bars are only statistical. The points have been slightly offset for clarity.

Table 6.3: The parameter values and χ^2_{red} obtained from previous PVES global fits [29, 162, 182, 183] and the current global analysis at LO for the Taylor expansion form factor fit without constraints from CSV.

	ρ_s[GeV$^-2$]	μ_s	χ^2_{red}
YRCT(2006) [162]	-0.06±0.41	0.12±0.55	1.3
YRCT(2007) [29]	0.02±0.18	-0.01±0.25	-
LMR(2007) [182]	-0.08±0.16	0.29±0.21	1.3
GCD(2014) [183]	0.26±0.16	-0.26±0.26	1.3
Taylor	0.15±0.04	-0.12±0.04	1.1

Table 6.4: The NLO strangeness parameters values obtained from the previous global fit [162], where $Q^2 < 0.3$ GeV^2, and from the current global analysis for the Taylor expansion form factor fit. The errors are statistical only. The χ^2 for each fit is displayed.

Parameter	YRCT(2006) [162]	Taylor
ρ_s [GeV^{-2}]	-0.03±0.63	0.07±0.14
ρ'_s [GeV^{-4}]	-1.5±5.8	0.14±0.22
μ_s	0.37±0.79	-0.05±0.15
μ'_s [GeV^{-2}]	0.7±6.8	-0.11±0.23
χ^2_{red}	1.4	1.23

earlier lattice [149] and lattice-constrained [147, 184, 185] results.

Fig. 6.3 displays the 95% and 68% confidence level ellipses in the (G^s_M, G^s_E) plane at $Q^2 = 0.1$ GeV^2 for the LO and NLO fits. This work seems to favour positive values for the strange electric form factor and negative values for the strange magnetic form factor. The strangeness form factors are compatible with zero at 95% and 68% confidence level ellipses using the NLO Taylor expansion.

The linear combination of strange electromagnetic form factors, G^s_E and G^s_M, can be written as

$$G^s_E + \eta G^s_M = \frac{A_{phys} - A_{NVS}}{\eta_E}, \tag{6.24}$$

where

$$\eta = \frac{\eta_M}{\eta_E}, \tag{6.25}$$

and A_{NVS} is the theoretical asymmetry assuming no vector strange quark contribution, i.e., $G^s_E = 0 = G^s_M$. The η's have been defined for each target at the beginning of Section 6.2. Table 6.5 presents the constraints on the net strange quark electromagnetic form factor contribution from each measurement as a linear combination. The calculated net strangeness signal $G^s_E + \eta G^s_M$ is shown in Fig. 6.4

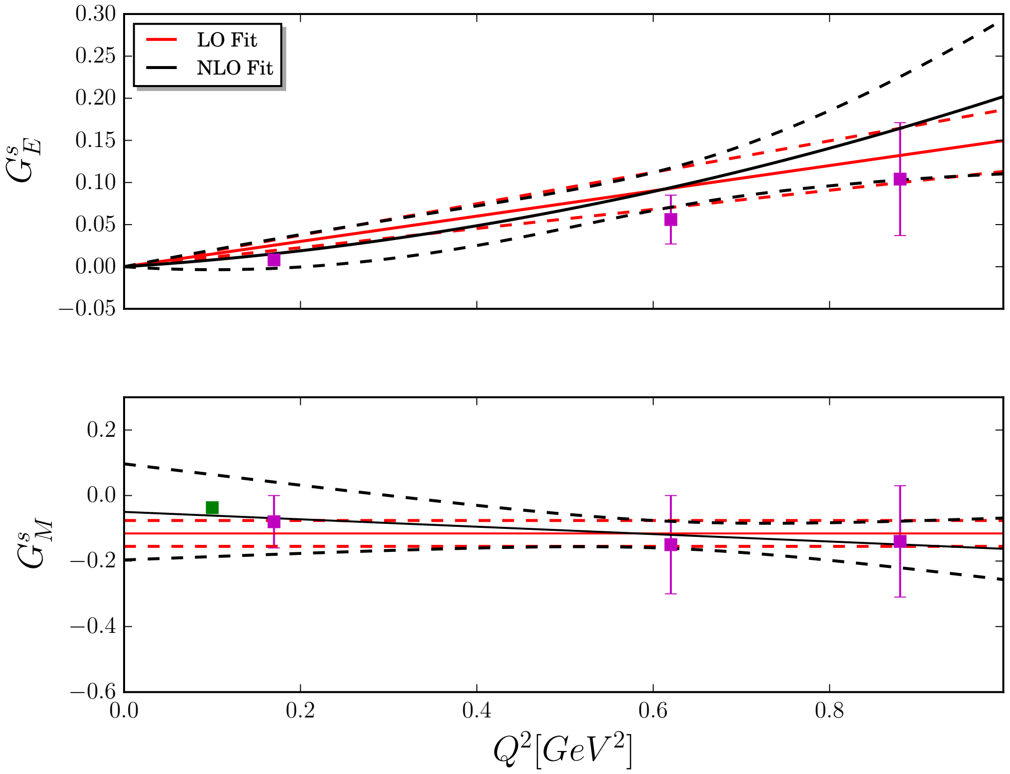

Figure 6.2: The extracted strange electric and magnetic form factors from a global fit up to $Q^2 \sim 1$ GeV^2 using the Taylor expansion. The red (black) solid curve shows the LO fit (NLO fit), and the bounds are shown by the dotted curves. A comparison with recent lattice QCD results is shown where the green square (errors bars are smaller than the symbol) corresponds to the result of $G_M^s(Q^2 = 0.1$ GeV^2) [151] and the magenta squares represent the G_M^s and G_E^s at $Q^2 = 0.17,\ 0.62$ and 0.88 GeV^2 [148].

for the forward-angle e–p scattering measurements. In contrast to the large angle scattering data, these measurements exhibit insensitivity to the axial component, A_A, of the PV asymmetry, as discussed in Chapter 5. Thus, in Fig. 6.4, using the value of $\tilde{g}_A^p$ obtained from the NLO global analysis instead of that extracted from the LO global analysis does not lead to a significant difference. Note that the precise HAPPEx data point appears to disagree with the forward-angle G0 data around $Q^2 = 0.6$ GeV^2, even though these two measurements have been performed under similar kinematic conditions.

To test the model-dependence of the Taylor expansion, the present work considers performing a global analysis using the so called z-expansion [186, 187] as well. This is the topic of the next section.

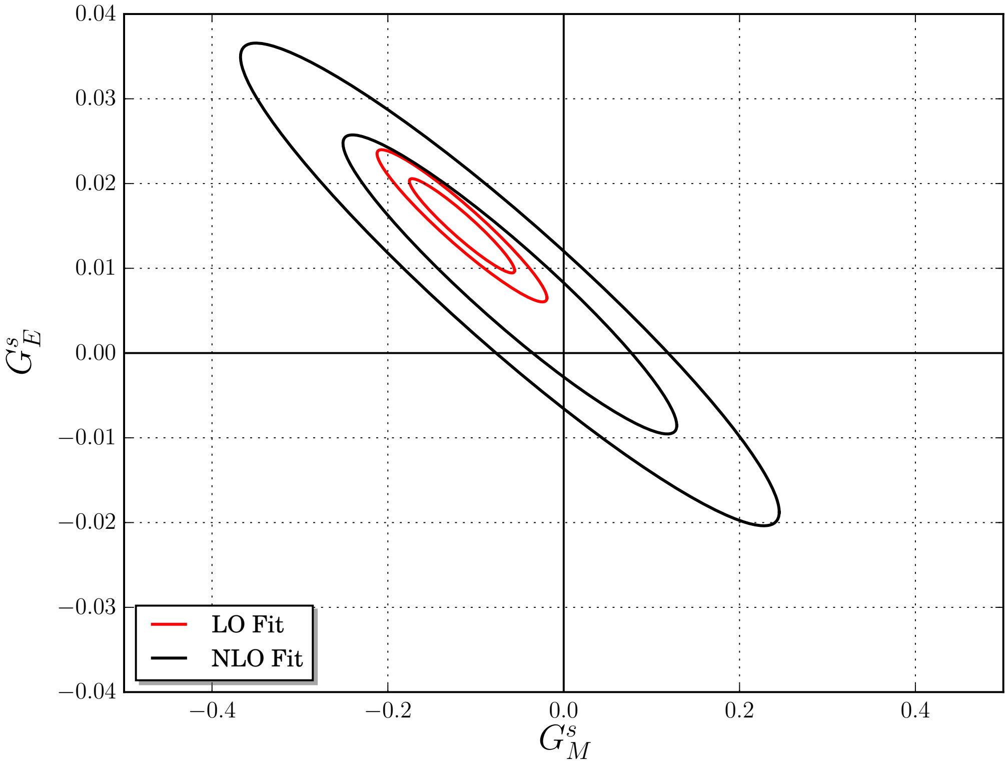

Figure 6.3: The 95% and 68% confidence level ellipses in the (G_M^s, G_E^s) plane at $Q^2 = 0.1$ GeV^2 for LO and NLO fit.

6.2.2 z-expansion

One might not expect a Taylor expansion up to ~ 1 GeV^2 to be satisfactory. To provide an alternative functional form to the Taylor expansion, the z-expansion, which offers improved convergence based on the analytic properties of the form factors [186–188], will be considered.

The z-expansion is a method of extraction that provides a model independent description of the shape of the form factors given by

$$G(Q^2) = \sum_{k=0}^{k_{\max}} a_k z^k. \tag{6.26}$$

The Q^2-dependence of the strange form factors using the z-expansion can be described, also to second (nontrivial) order, as

$$G_E^s = \rho_{s,z} z + \rho'_{s,z} z^2 \tag{6.27}$$

Table 6.5: The linear combination $G_E^s + \eta G_M^s$ for the measurements. $G_E^s + \eta G_M^s$ LO (NLO) indicates that the A_{NVS} has been calculated using the $\tilde{g}_A^N$ extracted from the LO (NLO) global fit.

Experiment	Target	Q^2	θ	$G_E^s + \eta G_M^s$ (LO)	$G_E^s + \eta G_M^s$ (NLO)
Qweak	p	0.025	7.9	0.002 ± 0.004	0.002 ± 0.004
SAMPLE	d	0.038	144.0	-0.818 ± 0.716	-0.802 ± 0.718
HAPPEx	^{4}He	0.077	6.0	0.002 ± 0.016	0.002 ± 0.016
SAMPLE	d	0.091	144.0	0.077 ± 0.670	0.100 ± 0.675
HAPPEx	^{4}He	0.091	6.0	-0.040 ± 0.043	-0.040 ± 0.043
HAPPEx	p	0.099	6.0	0.037 ± 0.026	0.037 ± 0.026
SAMPLE	p	0.100	144.0	0.362 ± 0.542	0.378 ± 0.547
PVA4	p	0.108	35.4	0.063 ± 0.032	0.063 ± 0.032
HAPPEx	p	0.109	6.0	0.014 ± 0.012	0.014 ± 0.012
G0	p	0.122	6.7	0.044 ± 0.044	0.044 ± 0.044
G0	p	0.128	6.8	0.097 ± 0.039	0.097 ± 0.039
G0	p	0.136	7.1	0.082 ± 0.036	0.082 ± 0.036
G0	p	0.144	7.3	-0.007 ± 0.035	-0.007 ± 0.035
G0	p	0.153	7.5	0.042 ± 0.036	0.042 ± 0.036
G0	p	0.164	7.8	0.018 ± 0.036	0.019 ± 0.036
G0	p	0.177	8.1	-0.021 ± 0.030	-0.021 ± 0.030
G0	p	0.192	8.4	0.010 ± 0.029	0.010 ± 0.029
G0	p	0.210	8.8	-0.001 ± 0.027	-0.001 ± 0.027
PVA4	p	0.220	144.5	-0.805 ± 0.455	-0.784 ± 0.467
G0	p	0.221	110.0	0.066 ± 0.115	0.071 ± 0.117
G0	d	0.221	110.0	-0.034 ± 0.146	-0.026 ± 0.149
PVA4	d	0.224	145.0	0.126 ± 0.710	0.160 ± 0.720
PVA4	p	0.230	35.3	0.036 ± 0.027	0.037 ± 0.028
G0	p	0.232	9.3	0.006 ± 0.026	0.007 ± 0.026
G0	p	0.262	9.9	0.046 ± 0.020	0.047 ± 0.020
G0	p	0.299	10.6	0.010 ± 0.027	0.010 ± 0.027
G0	p	0.344	11.4	0.042 ± 0.032	0.042 ± 0.032
G0	p	0.410	12.6	0.060 ± 0.027	0.061 ± 0.027
HAPPEx	p	0.477	12.3	0.023 ± 0.020	0.023 ± 0.020
G0	p	0.511	14.2	0.023 ± 0.038	0.024 ± 0.038
HAPPEx	p	0.624	13.7	0.006 ± 0.011	0.006 ± 0.012
G0	p	0.628	110.0	-0.296 ± 0.147	-0.290 ± 0.150
G0	d	0.628	110.0	-0.085 ± 0.251	-0.076 ± 0.253
G0	p	0.631	16.0	0.064 ± 0.028	0.064 ± 0.028
G0	p	0.788	18.2	0.034 ± 0.041	0.034 ± 0.041
G0	p	0.997	20.9	0.071 ± 0.087	0.072 ± 0.087

and

$$G_M^s = \mu_s + \mu'_{s,z} z, \tag{6.28}$$

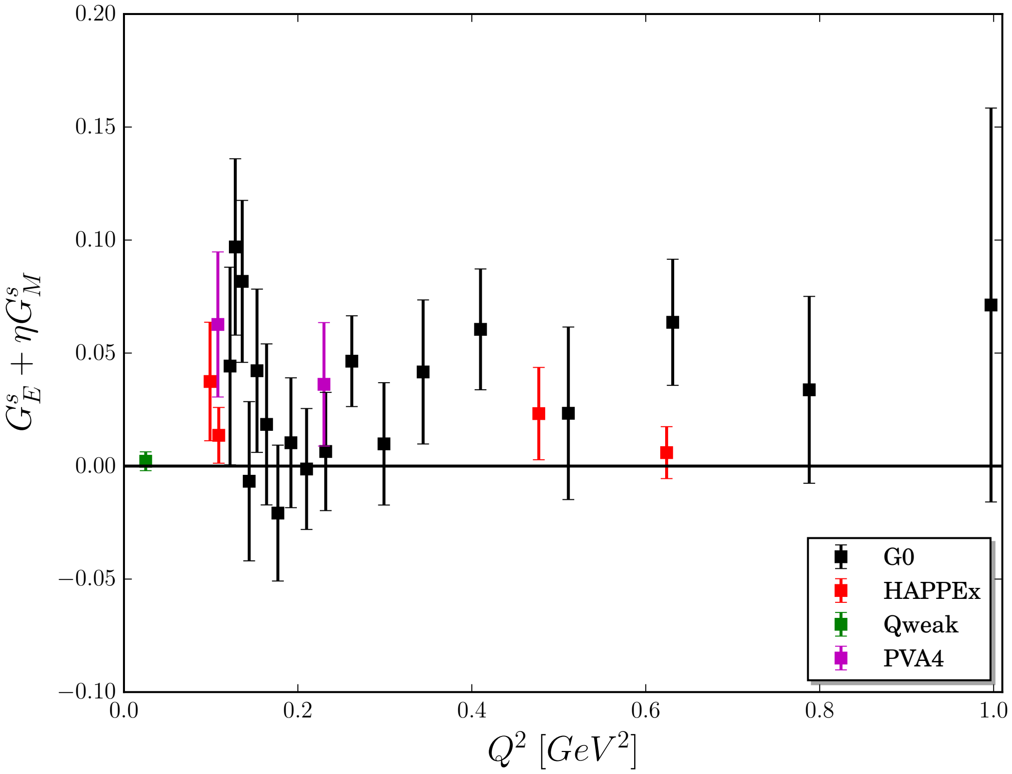

Figure 6.4: The net strangeness $G_E^s + \eta G_M^s$ contribution to the form factors constrained by the forward elastic asymmetry from different e-p scattering measurements.

where

$$z = \frac{\sqrt{t_{cut} + Q^2} - \sqrt{t_{cut}}}{\sqrt{t_{cut} + Q^2} + \sqrt{t_{cut}}}, \tag{6.29}$$

and $t_{cut} = (2m_K)^2$ with the kaon mass $m_K = 0.494$ GeV. In the absence of isospin violation, the cut formally starts at $9m_\pi^2$. However, the assumption that the strangeness contribution to the 3-pion state can be neglected has been employed in this analysis. Furthermore, with the current experimental precision, there is not any significant sensitivity to the value of t_{cut}. To more easily facilitate the comparison with the two expansion forms, for the z-expansion fits, the expansions have been translated back in the leading Taylor form, e.g., the strange charge radius is calculated from the fitted slope $\rho_{s,z}$ using $\rho_s = dG_E^s/dQ^2|_{Q^2=0}$.

Table 6.6 represents the parameter values and χ^2 obtained from previous PVES global fits [29, 162, 182, 183] and from the current global analysis at LO for both Taylor and z-expansion form factor fits. These results are consistent with each other, with significantly reduced uncertainty. In Table 6.7 the parameter values and χ^2 obtained from the global analysis at NLO for both Taylor and z-expansion form factor fits are reported with a comparison with the previous work [162]. It is clear that the strangeness parameters obtained from the global analysis with either Taylor and z-expansion show remarkable agreement with each other.

The extraction of the strange form factors over the current Q^2 domain is shown in Fig. 6.5. Based on Figs. 6.2 and 6.5, it is clear that the strange electric and magnetic form factors have identical behaviours in both the Taylor expansion and z-expansion fit.

Fig. 6.6 displays the 95% confidence level ellipses in the (G_M^s, G_E^s) plane at $Q^2 = 0.1$ GeV^2 for the NLO fit for both Taylor and z-expansion strangeness parameterisations. As can be seen, the prediction for the z-expansion global fit agrees very well with the Taylor expansion global fit.

Given the high degree of correlation in the measurements, it is instructive to display the joint confidence intervals. Fig. 6.7 displays the 95% confidence level ellipses for the different values of $Q^2 = 0.1$, 0.23 and 0.63 GeV^2 for the NLO z-expansion fit. At the low-Q^2 values, the strangeness form factors are compatible with zero at the 95% CL, with a marginal preference for positive values of the strange electric form factor and negative values of the magnetisation, as seen previously in [29, 189]. At $Q^2 = 0.63$ GeV^2, there appears a clear signal for non-zero strangeness, with a negative G_M^s and positive G_E^s. In contrast to earlier work that has suggested vanishing strangeness at this Q^2 [165, 176], the dominant difference in the present work is the treatment of the axial/anapole form factor. As described, the isoscalar combination is constrained by the effective field theory with vector-meson dominance models estimate of Zhu *et al.* [160], while the isovector combination is determined by the data. The best fit—for the z-expansion at NLO—results in $\tilde{g}_A^p = -0.67 \pm 0.25$, which is less negative than the zero-anapole approximation. As a consequence, the data-driven fit drives the back-angle G0 results to be more consistent with a negative G_M^s. Under these assumptions for the effective axial form factor, one can see G_E^s ~ 0.1, which—with the strange charge factor included—is in the order of 10% of the proton electric form factor at this momentum transfer. To investigate the effect of the uncertainty related to the axial form factor, a conservative variation of the axial mass M_A has been considered to be $M_A = 1.026 \pm 0.500$ GeV. It is found that some of the strangeness form factor results have differed as shown in Table 6.8. The most significant shift is seen for G_M^s at the larger Q^2 point, yet still within 1-sigma uncertainty and the conclusion derived from Fig. 6.7 still holds.

Fig. 6.8 compares the extracted $\mu_s \equiv G_M^s(Q^2 = 0)$ from this work with some previous PVES global analyses, in addition to some theoretical lattice results. As can be seen, there is a good agreement among the PVES global analysis results

Table 6.6: The parameter values and χ^2_{red} obtained from previous PVES global fits [29, 162, 182, 183] and the current global analysis at LO for both Taylor and z-expansion form factor fits without constraints from CSV.

	ρ_s[GeV$^-2$]	μ_s	χ^2_{red}
YRCT(2006) [162]	-0.06±0.41	0.12±0.55	1.3
YRCT(2007) [29]	0.02±0.18	-0.01±0.25	-
LMR(2007) [182]	-0.08±0.16	0.29±0.21	1.3
GCD(2014) [183]	0.26±0.16	-0.26±0.26	1.3
Taylor	0.15±0.04	-0.12±0.04	1.1
z-exp.	0.18±0.05	-0.10±0.04	1.1

Table 6.7: The NLO strangeness parameters values obtained from the previous global fit [162], where $Q^2 < 0.3$ GeV^2, and from the current global analysis for both Taylor and z-expansion form factor fits. The errors are statistical only. The χ^2 for each fit is displayed.

Parameter	YRCT(2006) [162]	Taylor	z-exp.
ρ_s [GeV^{-2}]	-0.03±0.63	0.07±0.14	0.08±0.17
ρ'_s [GeV^{-4}]	-1.5±5.8	0.14±0.22	0.19±0.37
μ_s	0.37±0.79	-0.05±0.15	-0.09±0.14
μ'_s [GeV^{-2}]	0.7±6.8	-0.11±0.23	-0.06±0.29
χ^2_{red}	1.4	1.23	1.26

Table 6.8: Strangeness form factor results at different values of $Q^2 \sim 0.1$, 0.23 and 0.63 GeV^2 against the variation of the axial dipole mass $M_A = 1.026 \pm 0.500$ GeV. Correlation coefficients between the G^s_M and G^s_E are represented by ρ.

		$Q^2 \sim 0.1$ GeV^2	$Q^2 \sim 0.23$ GeV^2	$Q^2 \sim 0.63$ GeV^2
$M_A = 1.026$	G^s_M	$-0.09(12)$	$-0.10(8)$	$-0.12(4)$
	G^s_E	$0.01(1)$	$0.03(2)$	$0.10(2)$
	ρ	-0.90	-0.90	-0.93
$M_A = 1.526$	G^s_M	$-0.10(11)$	$-0.10(9)$	$-0.10(4)$
	G^s_E	$0.01(1)$	$0.03(2)$	$0.09(2)$
	ρ	-0.90	-0.90	-0.93
$M_A = 0.526$	G^s_M	$-0.13(12)$	$-0.14(9)$	$-0.16(4)$
	G^s_E	$0.01(1)$	$0.03(2)$	$0.11(2)$
	ρ	-0.91	-0.90	-0.93

within the error bars. However, the current extracted results from LO fits show smaller uncertainties. Furthermore, μ_s from LO fits are compatible with a recent lattice result obtained by Shanahan *et al.* [148], Sufian *et al.* [151] and Leinweber

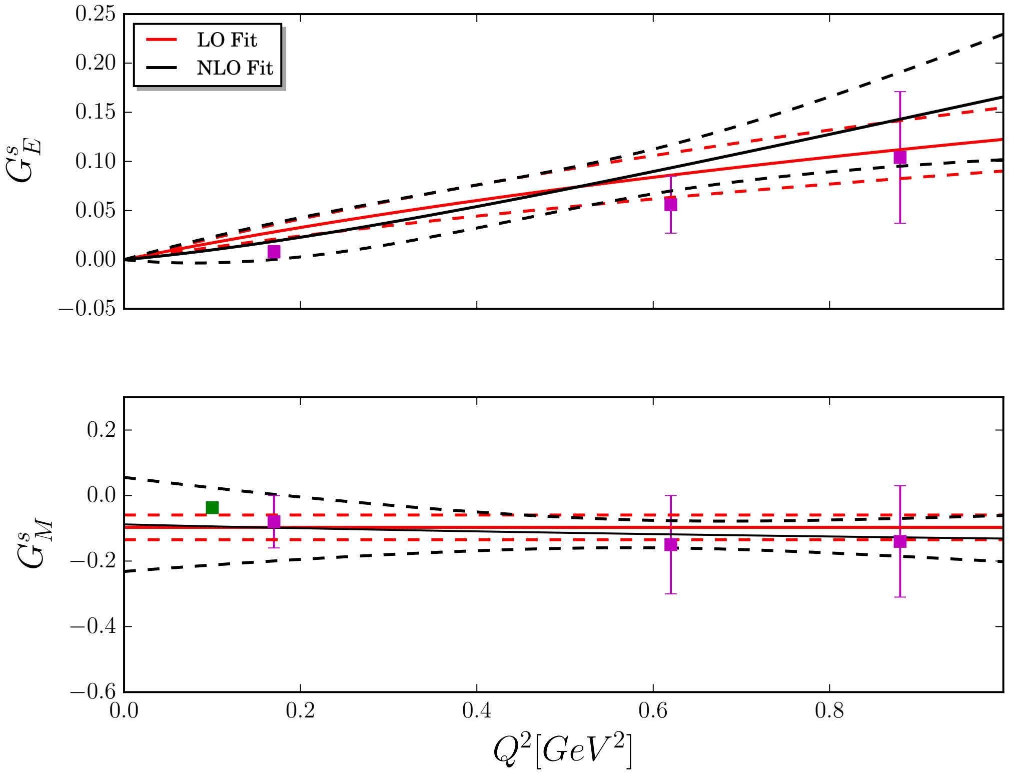

Figure 6.5: The extracted strange electric and magnetic form factors from a global fit up to $Q^2 \sim 1$ GeV^2 using the z-expansion. The red (black) solid curve shows the LO fit (NLO fit) and bound shown by the dotted curves. A comparison with recent lattice QCD results is shown where the green square (error bars are smaller than the symbol) corresponds to the result of $G_M^s(Q^2 = 0.1 \text{ GeV}^2)$ [151] and the magenta squares represent the G_M^s and G_E^s at a different value of $Q^2 = 0.17,\ 0.62$ and 0.88 GeV^2 [148].

et al. [147] within uncertainties. Note that, as discussed previously, the statistical uncertainties displayed by LO fits are not representative of the current knowledge of the strange form factors over the full range $0 \leq Q^2 \lesssim 1.0$ GeV^2.

It would be interesting to compare the behaviour of the evolution of μ_s and ρ_s in the Taylor and z-expansion fits with increasing Q^2 (increasing the number of data) at LO and NLO, and this has been done in Fig. 6.9. As can be noted, to the level of truncation of the data set at a maximum Q^2, the results of μ_s and ρ_s obtained from the LO fit for the Taylor expansion are similar to the corresponding results obtained from the LO fit for the z-expansion. A similar conclusion applies to the NLO for both Taylor and z-expansion form factor fits.

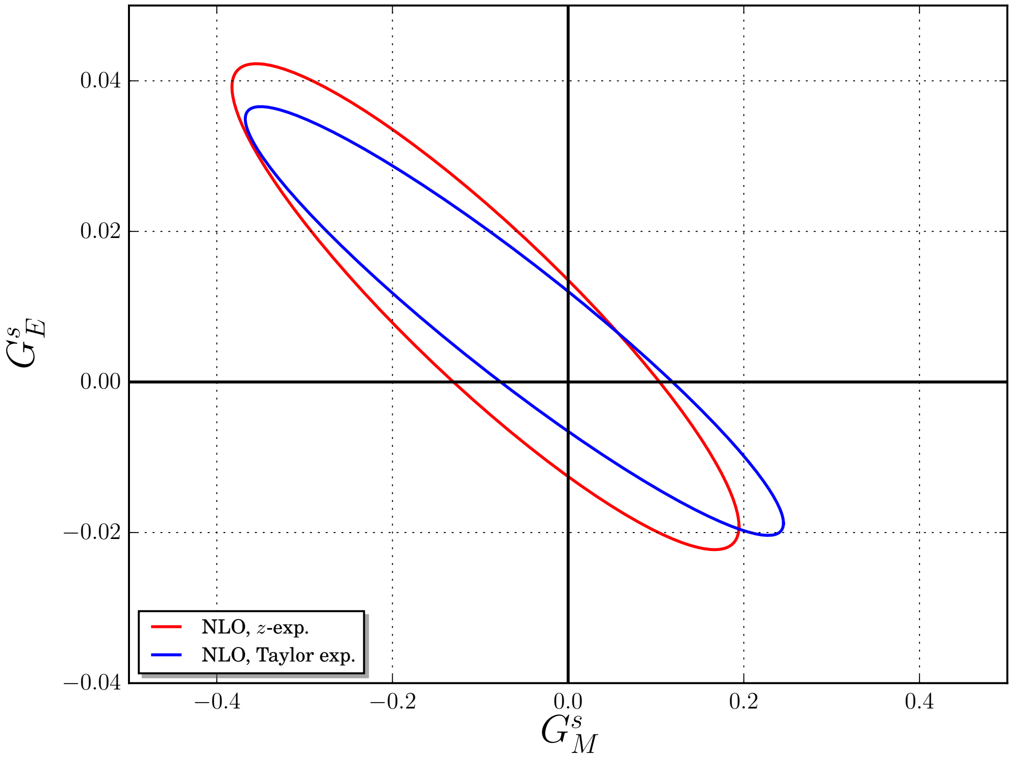

Figure 6.6: The 95% confidence level ellipses in the (G_M^s, G_E^s) plane at $Q^2 = 0.1$ GeV^2 for the NLO fit for both Taylor and z-expansions strangeness parameterisations.

6.3 Sensitivity to the Charge Symmetry Violation (CSV)

As mentioned previously, a limiting factor in the precision of experimental measurements of the strangeness form factors of the proton has been the uncertainty surrounding the degree to which charge symmetry violation (CSV) affects their determination from PVES experiments. In this section, the impact of CSV on the extracted strangeness from the PVES global analysis is investigated.

While earlier theoretical predictions of CSV in the proton's EM form factors varied through several orders of magnitude [31–34], a recent lattice QCD calculation [35] has determined that CSV in the proton's EM form factors is significantly smaller than earlier expectations. Despite its importance for future measurements of parity-violating electron-proton scattering and their subsequent interpretation of proton strangeness, the precise influence of this recent CSV constraint has not been thoroughly quantified. Hence, in this section, a global analysis of the full set of parity-violating asymmetry data with non-vanishing CSV form factors is performed.

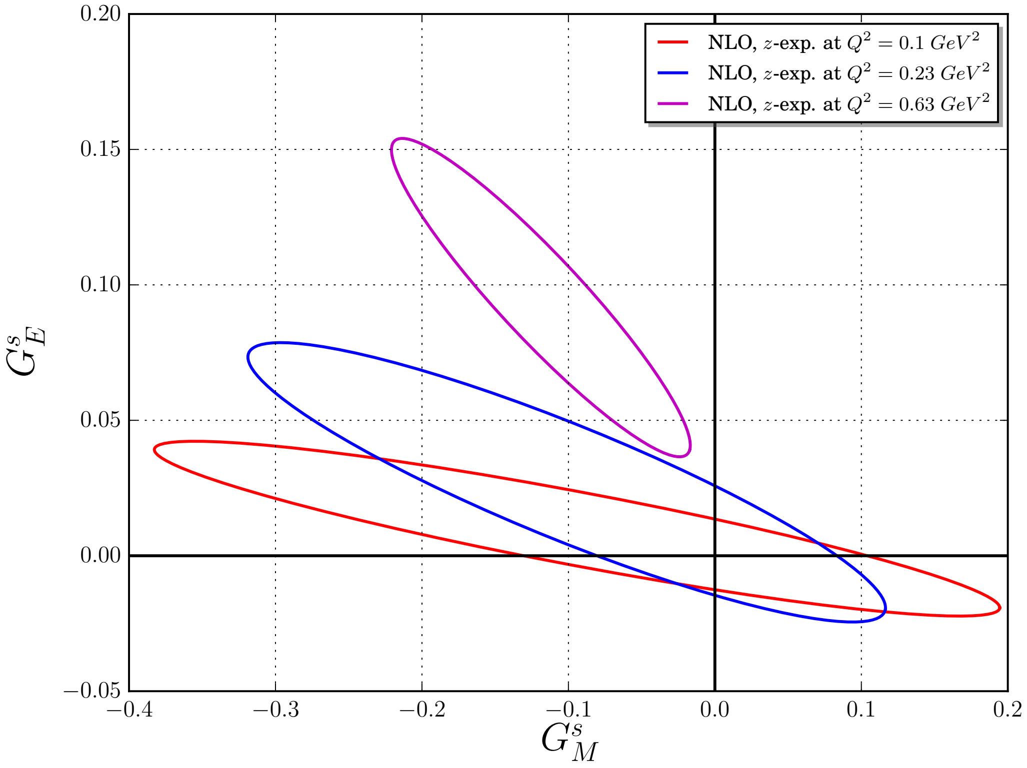

Figure 6.7: 95% confidence level ellipses for the electric and magnetic strangeness form factors using the NLO z-expansion in Eqs. (6.27) and (6.28) for three Q^2 values 0.1, 0.23 and 0.63 GeV^2.

6.3.1 Neutral Weak Form Factor and CSV

The CSV effects characterise the breaking of the approximate $SU(2)$-flavour symmetry of the u and d quarks.

Charge symmetry, physically, refers to the invariance of the strong interaction under a rotation by 180° about the 2-axis in isospace. Under this rotation u-quarks turn into d-quarks and vice-versa, i.e., exchanging the proton and neutron. If the charge symmetry is violated, the u quark in the proton is no longer the same as the d quark in the neutron and the d quark in the proton is not the same as the u quark in the neutron:

$$\begin{aligned} G_{E,M}^{p,u} &\neq G_{E,M}^{n,d}, \\ G_{E,M}^{p,d} &\neq G_{E,M}^{n,u}. \end{aligned} \tag{6.30}$$

The CSV form factor relevant to PVES can be defined as a combination of those

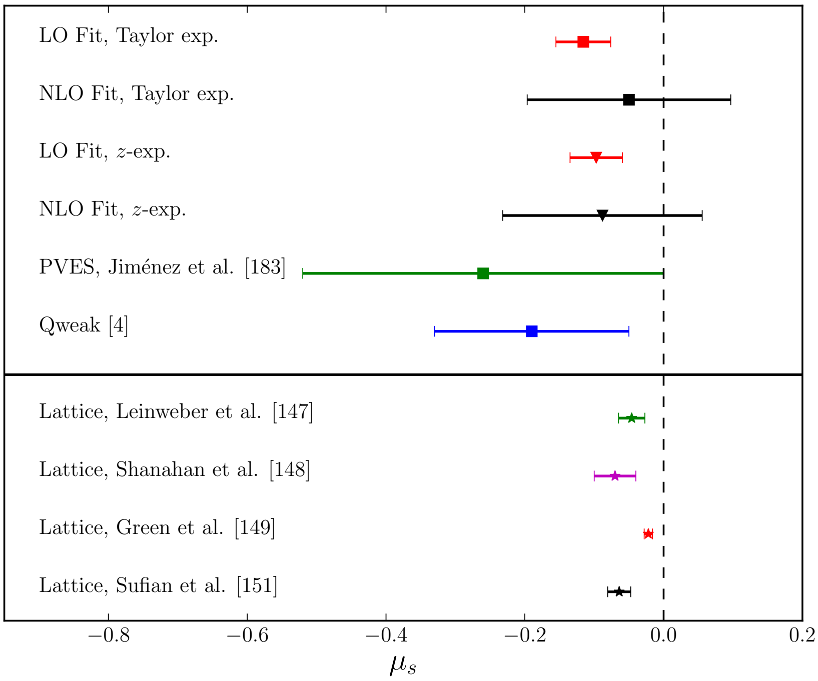

Figure 6.8: Comparison of the extracted $\mu_s \equiv G^s_M(Q^2 = 0)$ from this work with some previous PVES global analyses, as well as some theoretical lattice results.

terms:

$$G^{CSV}_{E,M} = \frac{2}{3}(G^{p,d}_{E,M} - G^{n,u}_{E,M}) - \frac{1}{3}(G^{p,u}_{E,M} - G^{n,d}_{E,M}). \tag{6.31}$$

In order to explore the CSV's effect, one needs to modify the neutral form factor in Eq. 5.51 to explicitly include a CSV term:

$$\begin{aligned} G^{Z,p}_{E,M} =&(1 - 4\sin^2\hat{\theta}_W)(1 + R^p_V)G^{\gamma,p}_{E,M}(Q^2) \\ &- (1 + R^n_V)G^{\gamma,n}_{E,M}(Q^2) - (1 + R^{(0)}_V)G^s_{E,M}(Q^2) \\ &- (1 + R^n_V)G^{CSV}_{E,M}(Q^2). \end{aligned} \tag{6.32}$$

The leading moments of the $G^{CSV}_{E,M}$ form factors can be expressed as [31, 32]

$$G^{CSV}_{E,M}(Q^2) = G^{CSV}_{E,M}(0) - \rho^{CSV}_{E,M}Q^2 + \mathcal{O}(Q^4), \tag{6.33}$$

with $G^{CSV}_E(0)$ set to zero due to charge conservation.

Based on the discussion presented above, the term η_0 in the theoretical asymmetry, i.e., Eq. 6.6, receives a correction from the CSV form factors and therefore

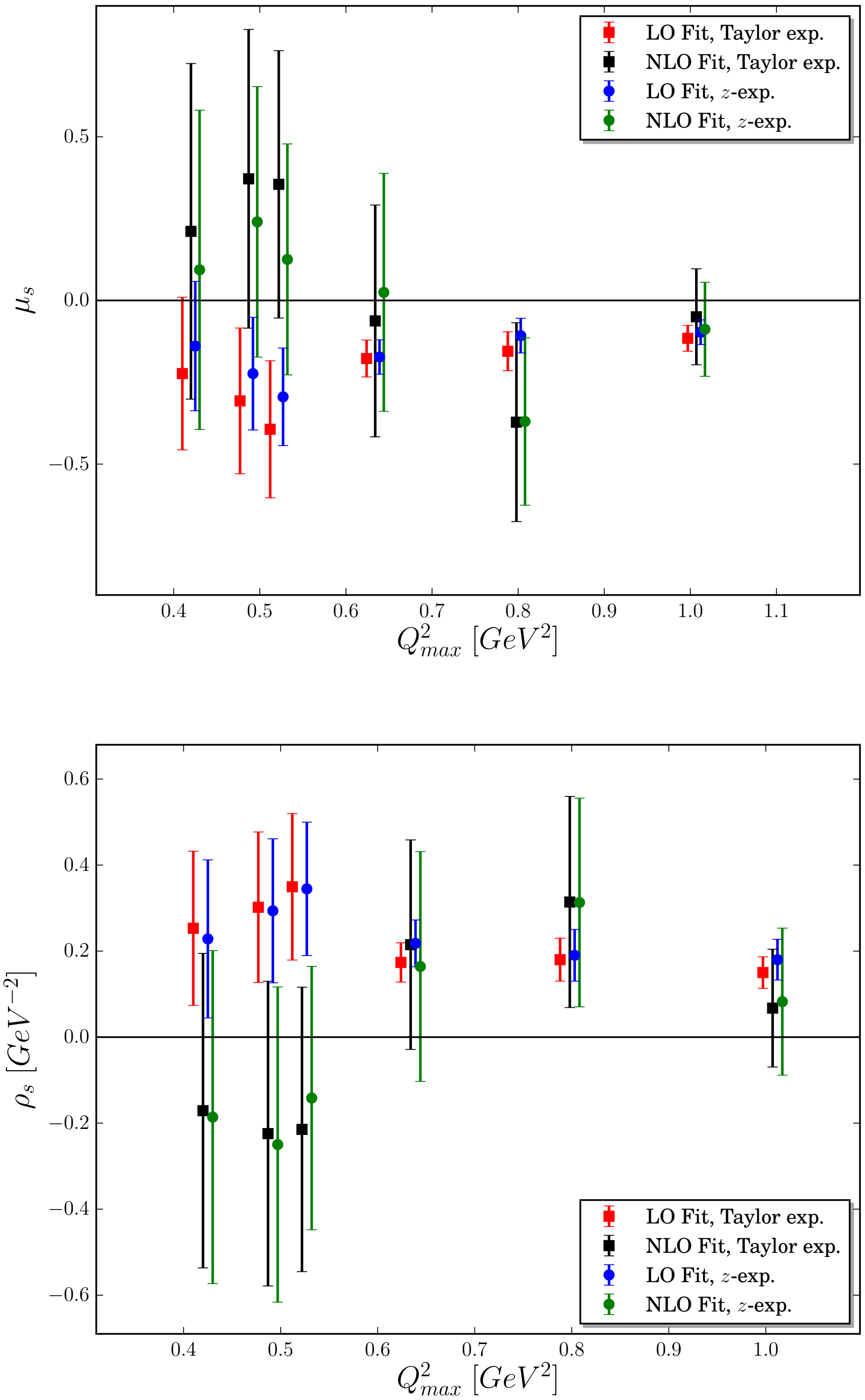

Figure 6.9: Shown are μ_s and ρ_s parameters values obtained from the LO and NLO for both Taylor and z-expansion fits at different maximum values of Q^2. The error bars are only statistical. The data points have been offset for clarity.

A_{Theory} is rewritten as

$$A_{Theory} = \eta_0^{CSV} + \eta_A^p \tilde{G}_A^p + \eta_A^n \tilde{G}_A^n + \eta_E G_E^s + \eta_M G_M^s, \tag{6.34}$$

where $\eta_0^{CSV} = \eta_0 + \eta_E^{CSV} G_E^{CSV} + \eta_M^{CSV} G_M^{CSV}$, with

$$\eta_{CSV,E}^{N} = \Big[\frac{G_F Q^2}{4\sqrt{2}\pi\alpha}\Big] \cdot \Big[\frac{(1+R_V^n)\epsilon G_E^{\gamma,N}}{\epsilon(G_E^{\gamma,N})^2 + \tau(G_M^{\gamma,N})^2}\Big], \tag{6.35}$$

$$\eta_{CSV,M}^{N} = \Big[\frac{G_F Q^2}{4\sqrt{2}\pi\alpha}\Big] \cdot \Big[\frac{(1+R_V^n)\tau G_M^{\gamma,N}}{\epsilon(G_E^{\gamma,N})^2 + \tau(G_M^{\gamma,N})^2}\Big]. \tag{6.36}$$

In the case of the PV asymmetry of ^{4}He, in addition to the CSV at nucleon level G_E^{CSV}, the CSV at nuclear level F^{CSV} should be considered. Thus, in this case η_0^{CSV} can be written as

$$\eta_0^{CSV} = \eta_0^{He} + \Big[\frac{G_F Q^2}{4\sqrt{2}\pi\alpha}\Big] \cdot \Big[-2F^{CSV} - 4\frac{(1+R_V^n)G_E^{CSV}}{G_E^p + G_E^n}\Big], \tag{6.37}$$

where η_0^{He} has been defined in Eq. (6.11) and F^{CSV} corresponds the ratio $F^{(1)}(q)/F^{(0)}(q)$ in [190]. The value of that ratio, $F^{(1)}(q)/F^{(0)}(q) \equiv F^{CSV} = -0.00157$ given in [190] is adopted to calculate η_0^{CSV} for the theoretical PV asymmetry of ^{4}He at $Q^2 = 0.077$ and 0.091 GeV^2.

6.3.2 CSV Theoretical Effects

In order to investigate the effect of CSV on the strangeness parameter values obtained from the analysis above, three different calculations of the CSV form factors will be considered.

The first work considered here was completed by Kubis and Lewis [31], denoted by 'K&L CSV'. They used an effective field theory, supplemented with resonance saturation to estimate the relevant contact term—where the CSV is largely driven by ρ—ω mixing. To accomplish this, they employed a large ω-nucleon coupling constant $g_\omega \sim 42$ taken from dispersion analysis. Combining this estimate with calculations in BChPT and infrared regularised baryon chiral perturbation theory, Kubis and Lewis predicted a CSV magnetic moment contribution $G_M^{CSV}(0) \equiv k^{u,d} = 0.025 \pm 0.020$, which includes an uncertainty arising from the resonance parameter. For the CSV slope parameters, they found $\rho_M^{CSV} = -0.08 \pm 0.06$ GeV^{-2} and $\rho_E^{CSV} = -0.055 \pm 0.015$ GeV^{-2}.

The second theoretical calculation of CSV considered is from Wagman and Miller [32], and denoted by 'W&M CSV'. In their work, they used relativistic chiral perturbation theory with a more realistic ω-nucleon coupling, i.e., $g_\omega \sim 10$. That study reported values of $G_M^{CSV}(0) = 0.012 \pm 0.003$, $\rho_M^{CSV} = 0.015 \pm 0.010$ GeV^{-2} and $\rho_E^{CSV} = -0.018 \pm 0.003$ GeV^{-2}.

The third determination of the CSV form factor that is employed here is based on an analysis of lattice QCD results [35], denoted by 'Lattice CSV'. The lattice study found significantly smaller values of the magnetic and electric CSV form factors compared to the previous two estimates. To study the effect of the CSV form factors obtained from lattice QCD, with a simple interpolation, the value of $G_M^{CSV} = 0.0 \pm 0.001$ and $\rho_E^{CSV} = 0.0 \pm 0.001$ GeV^{-2} have been employed.

The first two CSV calculations were accomplished for $Q^2 < 0.3$ GeV^2. For the considered Q^2 range, these calculations need to be extended. To do so, the following expression is used:

$$G_{\text{ext.}}^{CSV} = G^{CSV}(Q^2 = 0.299)\left(1 + \left(\frac{Q^2 - 0.299}{\Lambda^2}\right)^2\right)^{-2}, \tag{6.38}$$

where $\Lambda^2 = 1$ GeV^2 was chosen to be the order of ϕ meson mass. The value $Q^2 = 0.299$ GeV^2 is the maximum Q^2 in the data set where the original K&L and W&M calculations of G^{CSV} can be applied, and Q^2 runs over the 0.299 GeV$^2 < Q^2 < 1$ GeV^2.

The uncertainties of the CSV form factors are the source of the uncertainty that propagates into the theoretical asymmetry as systematic errors. In order to propagate the uncertainties, the covariance matrix above, Eq. (6.22), is extended to include a correlated uncertainty associated with the theoretical estimates of CSV. For each theoretical description, the entire data set has been reanalysed, and the determination of the strange magnetic moment μ_s (top panel) and strange electric radius ρ_s (bottom panel) are presented in Fig. 6.10. Since the lattice CSV form factors are zero with a negligible uncertainty, they are consistent with the 'No CSV' results. No visible impact on μ_s and ρ_s from the inclusion of the 'W&M CSV' form factors was found, except small shifts in the central values of μ_s obtained from the NLO fits. Finally, when estimating the CSV form factors by the K&L parameters, shifts in the central value of the strangeness magnetic moment were observed. Nevertheless, even the 'worst case' scenario of K&L does not appreciably affect the NLO fits.

For completeness, in Fig. 6.11 the 95% confidence level ellipses at $Q^2 = 0.1$ GeV^2 in (G_M^s, G_E^s) plane for the NLO z-expansion fit with and without including K&L CSV calculations are presented. As can be noted, the zero strangeness is inside the ellipses, and the differences between the two ellipses are not significant.

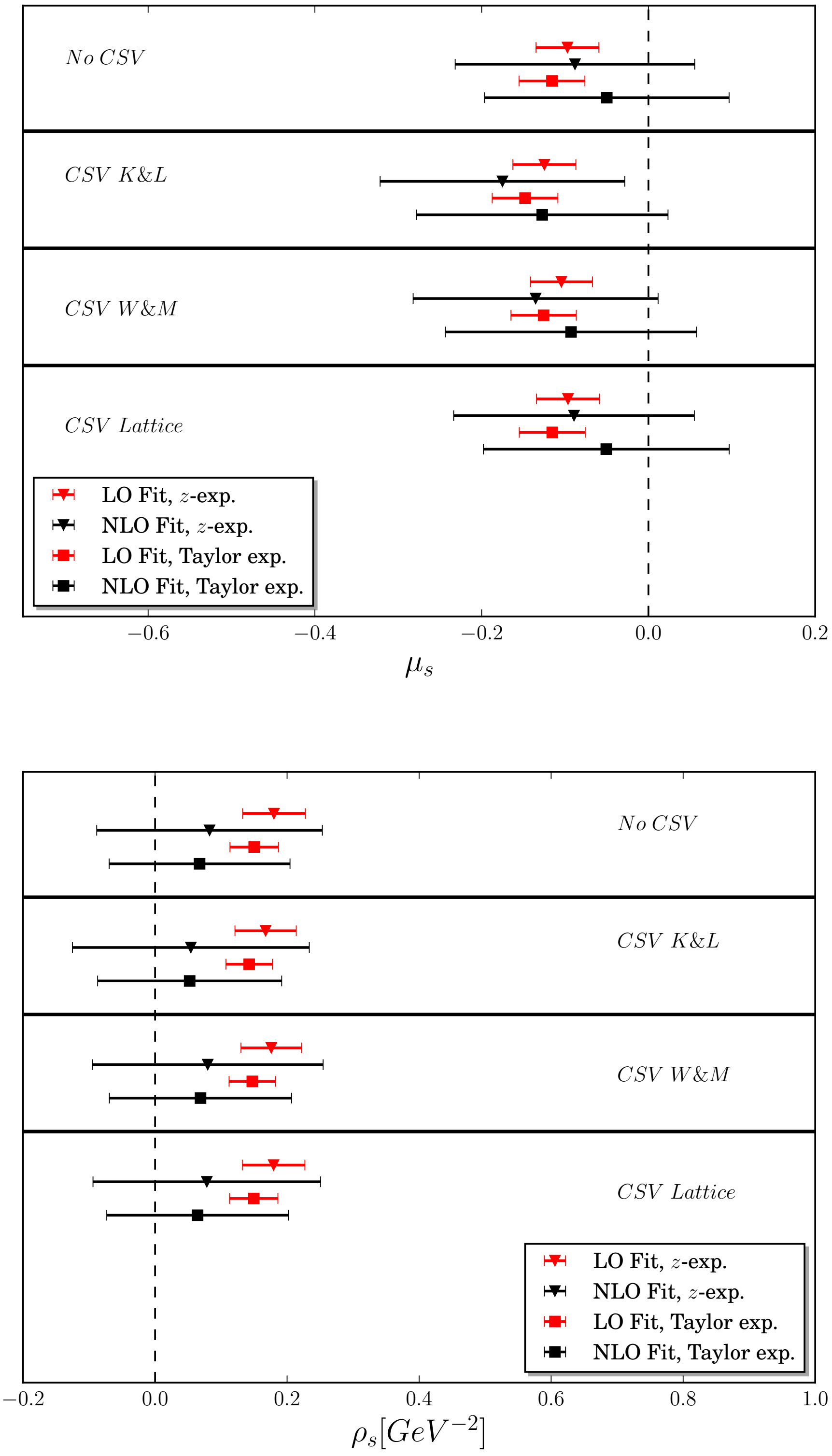

Figure 6.10: Comparison of determinations obtained from the present work with and without CSV for the strange magnetic moment μ_s (top panel) and strange electric radius ρ_s (bottom panel).

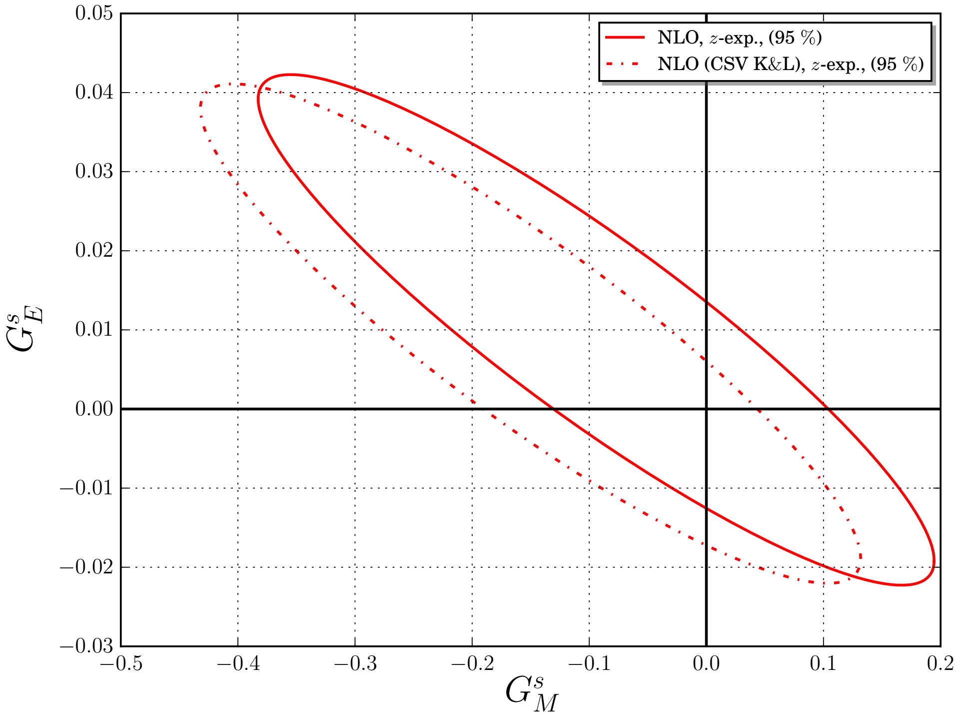

Figure 6.11: The 95% confidence level ellipses in the (G_M^s, G_E^s) plane at $Q^2 = 0.1$ GeV^2 for the NLO z-expansion fit with and without including K&L CSV calculations.

This analysis reveals that the CSV's effects are negligible and paves the way for future measurements of parity-violating electron-proton scattering to extract strangeness in the nucleon.

6.3.3 Summary and Discussion

In this chapter, a complete global analysis of all PVES asymmetry data, up to the currently available limit of $Q^2 \sim 1\text{GeV}^2$, for the proton, ^{4}He and deuteron, has been presented.

In order to extract information on the strange quark form factor using this data set, their Q^2-dependence has been parameterised by a Taylor expansion in Q^2. In regard to the axial form factors, the dipole form factor was employed to describe the axial form factor's Q^2-dependence.

In the current study, the isovector contribution from the axial radiative and anapole corrections were fit to data, whereas model estimates were used for the isoscalar.

This work took into account performing the model-independent z-expansion fit to assess the model-dependence of the Taylor expansion fit and found that both fits produced consistent values.

The γZ exchange correction and the effect that CSV form factors have on the extraction of strange quark contribution have been investigated. Including γZ box contribution in the analysis led to small increases in the magnitude of the central values of μ_s and ρ_s when compared to results obtained without constraints from the γZ-exchange. CSV results considered in this work have small effects on the central values of the strangeness parameters, with the largest effect, while still small, coming from the inclusion of the CSV form factors as provided by Kubis and Lewis [31].

The latest theory estimates on CSV are small — indeed small enough that they would not cloud the interpretation of future precision strangeness measurements. However, one can note that the back-angle measurements do exhibit sensitivity to the effective axial form factor, presenting an opportunity for future investigation. The combined efforts to improve the resolution of strangeness, and reveal the structure of the anapole form factor offer the potential to establish a precision era of QCD and the nucleon. While further advancing the understanding of the mechanisms underlying nonperturbative QCD, such work will serve to gain further confidence in the use of lattice QCD for precision constraints in tests of the Standard Model.

Chapter 7

Interference Electroweak Structure Functions

The interpretation of experimental results from low-energy tests of the SM highlights the importance of the precision of theoretical predictions. For example, the interpretation of the Q_{weak} result is sensitive to radiative corrections. Since most of the radiative corrections have been calculated to the level of the precision necessary for the Q_{weak} experiment, the γZ box correction is usually subject to considerable debate.

Thus far, the γZ box correction is understood within phenomenological models such as the Adelaide-Jefferson Lab-Manitoba (AJM) [7], Gorchtein *et al.* (GHRM) [158] and, Carlson and Rislow models [157].

At large Q^2, the parton model provides the link between the deep-inelastic structure functions and the quark structure of the nucleon. At low Q^2, the parton model is incomplete and cannot describe the rich structure of the inelastic scattering data.

A recent new method has been developed to compute the electromagnetic Compton amplitude $T_1^{\gamma\gamma}$ directly from a lattice calculation [8]. A possible extension to this method involves studying the γZ interference Compton amplitude $T_1^{\gamma Z}$ at low Q^2. There is a question of what accuracy for $T_1^{\gamma Z}$ is required from the lattice to improve the AJM or GHRM models.

In the next section, the γZ box correction to the proton's weak charge Q_{W}^p is discussed. In Section 7.2, for a physical interpretation of the structure functions at low Q^2, AJM and GHRM phenomenological models and their construction of interference structure functions $F_{1,2}^{\gamma Z}$ from the corresponding electromagnetic structure functions $F_{1,2}^{\gamma\gamma}$ will be highlighted. In Section 7.3, a brief discussion on the recently proposed method to calculate the structure functions directly from a lattice calculation of the Compton amplitude utilising the operator product expansion is presented [8]. As this method can be extended to consider $T_1^{\gamma Z}$, Section 7.4 deals with the question about the necessary accuracy of $T_1^{\gamma Z}$ on the lattice to constrain the phenomenological models.

7.1 The γZ Box Correction to Q_{W}^{p}

In the Q_{weak} experiment, a beam of longitudinally polarised electrons accelerated to energy $E = 1.165$ GeV are elastically scattered from a stationary proton target. The resulting average Q^2 of this experiment is $Q^2 = 0.025$ GeV^2.

As indicated in Eq. (5.49), at this small Q^2, the proton's structure is suppressed and the parity-violating asymmetry is dominated by the proton's weak charge:

$$A_{PV}^{p} = \left[\frac{-G_F Q^2}{4\sqrt{2}\pi\alpha}\right] Q_W^p. \tag{7.1}$$

At tree level, the proton's weak charge is given by

$$Q_W^p = 1 - 4\sin^2\theta_W. \tag{7.2}$$

However, at the Q_{weak} experiment precision level, radiative corrections must be taken into account [30]:

$$Q_W^p = (1 + \Delta\rho + \Delta_e)(1 - 4\sin^2\theta_W(0) + \Delta_e') + \Box_{WW} + \Box_{ZZ} + \Box_{\gamma Z}(0), \tag{7.3}$$

where $\Box_{\gamma Z}(0)$ is the γZ box diagram calculated at $E = 0$.

The $\Box_{\gamma Z}$ corrections arise from the interference γZ diagrams illustrated in Fig. 7.1, where the $\Box_{\gamma Z}$ can be defined as [191]

$$\Box_{\gamma Z} = (1 - 4\sin^2\hat{\theta}_W)\frac{\Re e\Big(\mathcal{M}_\gamma^* \mathcal{M}_{\gamma Z}^{(\mathrm{PV})}\Big)}{\Re e\Big(\mathcal{M}_\gamma^* \mathcal{M}_{Z}^{(\mathrm{PV})}\Big)}, \tag{7.4}$$

where $\mathcal{M}_Z^{(\mathrm{PV})}$ and $\mathcal{M}_{\gamma Z}^{(\mathrm{PV})}$ are the vector-axial vector (parity-violating) parts of the Z and γZ interference amplitudes. The correction $\Box_{\gamma Z}$ has an axial-vector electron, vector hadron component $\Box_{\gamma Z}^{V}$ and a vector electron, axial-vector hadron component $\Box_{\gamma Z}^{A}$, i.e., Eq. (6.2).

The most accurate method to calculate the $\Box_{\gamma Z}^{V}$ contributions is the dispersion relation [6]. The dispersion relation calculations of these contributions have been

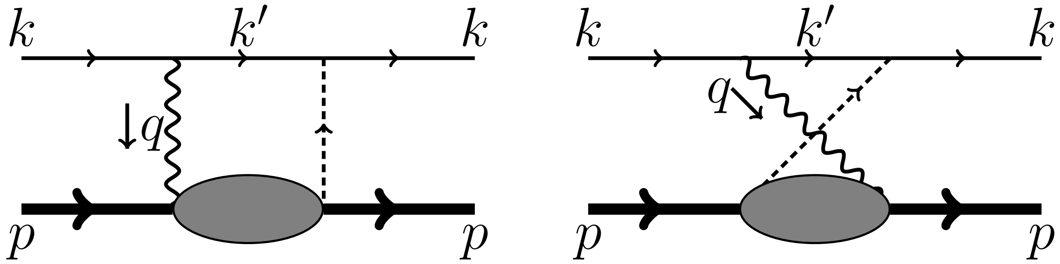

Figure 7.1: γZ box (left) and crossed box (right) diagrams. The wavy and dashed lines indicate the exchanged γ and Z bosons. p, k, q and k' are the hadron, electron, virtual photon and outgoing electron momenta, respectively.

improved at forward scattering angles, whereas these contributions are unknown at large scattering angles where the dispersion relation is not valid.

At forward angles, $\square^{V}_{\gamma Z}$ can be computed from its imaginary part using the dispersion relations:

$$\Re e \square^{V}_{\gamma Z}(E) = \frac{2E}{\pi} \int_{\nu_\pi}^{\infty} dE' \frac{1}{E'^2 - E^2} \, \Im m \square^{V}_{\gamma Z}(E'), \tag{7.5}$$

where $\nu_\pi = (W_\pi^2 - M^2)/2M$. The invariant mass at the pion-production threshold is $W_\pi^2 = (M + m_\pi)^2$, where m_π is the pion mass. From the optical theorem, the imaginary part of the PV interference amplitude can be written in terms of the product of leptonic $L_{\mu\nu}$ and hadronic $W_{\mu\nu}$ tensors as [156]

$$2\, \Im m \mathcal{M}^{(PV)}_{\gamma Z} = 4\pi M \int \frac{d^3k'}{(2\pi)^3 2E_{k'}} \left(\frac{4\pi\alpha}{Q^2} \right) \left(\frac{-2G_F}{\sqrt{2}} \right) \frac{1}{1 + Q^2/M_Z^2} L^{\gamma Z}_{\mu\nu} W^{\mu\nu}_{\gamma Z}, \tag{7.6}$$

where $q = k - k'$ is the virtual photon momentum transfer with $Q^2 = -q^2$. Using $L^{\gamma Z}_{\mu\nu}$ and $W^{\mu\nu}_{\gamma Z}$, as defined in [156, 191], and changing variable using

$$\frac{d^3k'}{(2\pi)^3 2E_{k'}} \to \frac{1}{32\pi^2 k.p} dW^2 dQ^2, \tag{7.7}$$

$\Im m \square^{V}_{\gamma Z}$ becomes

$$\begin{aligned} \Im m \square^{V}_{\gamma Z}(E) = & \frac{\alpha}{(s - M^2)^2} \int_{W_\pi^2}^{s} dW^2 \int_0^{Q^2_{max}} \frac{dQ^2}{1 + Q^2/M_Z^2} \\ & \times \left[F_1^{\gamma Z} + F_2^{\gamma Z} \frac{s\big(Q^2_{max} - Q^2\big)}{Q^2\big(W^2 - M^2 + Q^2\big)} \right], \end{aligned} \tag{7.8}$$

where $k \cdot p = ME$ has been evaluated in the rest frame of the proton. The total c.m. energy squared is $s = M(M + 2E)$ and $Q^2_{max} = (s - M^2)(s - W^2)/s = 2ME(1 - W^2/s)$. The structure functions $F^{\gamma Z}_{1,2}$ are analogues of the electromagnetic structure functions $F^{\gamma\gamma}_{1,2}$. $F^{\gamma Z}_{1,2}$ are functions of Q^2 and of the invariant mass W (or of the Bjorken variable $x = Q^2/(W^2 - M^2 + Q^2)$ [156]).

The structure functions can be written in terms of the transverse cross section σ_T (the cross section for the proton to absorb a transversely polarised photon) and longitudinal cross section σ_L (the cross section for the proton to absorb a longitudinally polarised photon) [67]:

$$F_1(W^2, Q^2) = \left(\frac{W^2 - M^2}{8\pi^2\alpha}\right)\sigma_T(W^2, Q^2), \tag{7.9}$$

$$F_2(W^2, Q^2) = \left(\frac{W^2 - M^2}{8\pi^2\alpha}\right)\frac{\nu}{M(1 + \nu^2/Q^2)}[\sigma_T(W^2, Q^2) + \sigma_L(W^2, Q^2)], \tag{7.10}$$

where $\nu = E - E'$ is the energy transfer of the electron to the target, where E and E' are the energy of the incoming and outgoing electron, respectively. These expressions are used for both $F^{\gamma\gamma}_{1,2}$ and $F^{\gamma Z}_{1,2}$.

7.2 Phenomenological Models

The physical interpretation of the structure functions takes on different character dependent upon the kinematic region of the scattering event. At low Q^2, where the strong coupling constant α_s is large, perturbation theory becomes an invalid technique for describing the structure functions. Therefore, phenomenological models are employed instead. The low-Q^2 region, itself, can be divided into two parts, namely resonance and Regge parts.

To construct the interference structure functions, one should consider the models that describe the electromagnetic structure functions. Below is a list of the most commonly used models:

- Christy-Bosted parameterisation (CB) [192]
- Colour dipole model (CDP) [193]
- Regge models [194]
- Vector meson dominance model (VMD) [195]

For the cross section σ in Eqs. (7.9) and (7.10) , it is common to be divided into a resonance part and a non-resonant background:

$$\sigma_{T,L} = \sigma_{T,L}^{(res)} + \sigma_{T,L}^{(bgd)}. \tag{7.11}$$

As discussed in the literature, the models for the description of the interference γZ structure functions are distinguished by how the background contributions are incorporated. However, for the resonance contributions, all of the models, except Sibirtsev *et al.* (SBMT) [156], utilise the Christy-Bosted parameterisation [192] in describing the electromagnetic structure functions at low W^2; however, these models vary in transforming these structure functions into their counterpart γZ structure functions.

The discussions presented in the following sections will focus on the Adelaide-Jefferson Lab-Manitoba (AJM) model, as it obtained the most precise calculation of $\Box_{\gamma Z}^{V}(E)$, and the model II of Gorchtein *et al.* (GHRM) [158], henceforth referred to as the GHRM model, as it provided the largest uncertainty on the estimation of $\Box_{\gamma Z}^{V}$. The AJM and GHRM models agree well on their predicted central values for the $\Box_{\gamma Z}^{V}(E)$ contribution. Both models employ VMD to account for the background contributions to the structure functions.

7.2.1 AJM Model

Precise knowledge of the γZ structure functions, $F_{1,2}^{\gamma Z}$, play an important role in a precise evaluation of $\Re e\Box_{\gamma Z}^{V}$. However, the difficulty of accomplishing this task stems from the lack of experimental data for these structure functions. Their counterpart electromagnetic structure functions, $F_{1,2}^{\gamma\gamma}$, have been estimated accurately in low-Q^2 and low-W^2 regions by many experiments, and $F_{1,2}^{\gamma Z}$ that have been extracted at high-Q^2 and high-W^2 provide a small contribution to the $\Re e\Box_{\gamma Z}^{V}$ correction. Thus, one needs to consider modelling these structure functions.

In constructing the AJM model, the excellent understanding of PDFs has been utilised as additional constraints on γZ structure functions [7]. In fact, this is an important feature of this model. The AJM model, with an extension to also incorporate duality constraints [177], is considered in the following discussion.

In the AJM model, the integrals over W^2 and Q^2 in Eq. (7.8) are divided into three different kinematic areas [177], as illustrated in Fig. 7.2. Region I (low-Q^2 and low-W^2) itself is divided into two regions: $0 \leq Q^2 \leq 10$ GeV^2 with $W_\pi^2 \leq W^2 \leq 4$ GeV^2 and $0 \leq Q^2 \leq 1$ GeV^2 with $4 < W^2 \leq 9$ GeV^2. In this region, the structure functions are characterised by Christy and Bosted's (CB) parameterisation, including resonance and background components [192]. For Region II (low-Q^2 and

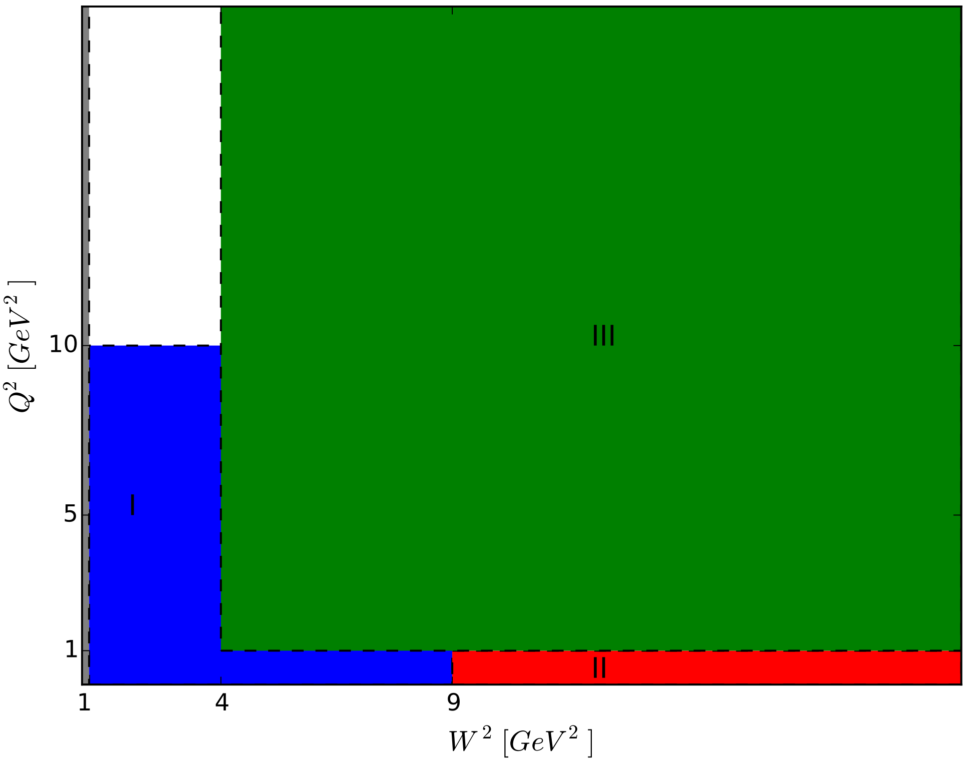

Figure 7.2: Divisions of kinematic regions in the AJM model. Region I (blue) at low W^2 and low Q^2 is described by the Christy and Bosted's (CB) parameterisation [192]; Region II (red) at low Q^2 and high W^2 is described by Regge theory and vector meson dominance (VMD) model [196]; and Region III (green) at high W^2 and high Q^2 is the deep-inelastic region characterised by global PDF fits to high-energy scattering data [197].

high-W^2), the Regge model combined with the vector meson dominance (VMD) model [196] is used over the range $0 \leq Q^2 \leq 1$ GeV^2 with $W^2 > 9$ GeV^2. In this region, the modified CB resonance contribution [158] has been taken into account. Here, VMD accounts for the background contribution to the structure functions in this region. Region III (high-Q^2 and high-W^2, deep-inelastic scattering region) $Q^2 > 1$ GeV^2 and $W^2 > 4$ GeV^2 is characterised by global PDF fits to high-energy scattering data [197]. These global fits are performed up to next-to-next-to-leading order in the fixed-flavour number scheme, and they include leading-twist (twist-2) and twist-4 contributions. Furthermore, the hadron mass effects (target mass corrections) are taken into account in these analyses.

7.2.2 AJM γZ Interference Structure Functions

At this stage, it is appropriate to discuss the construction of the interference structure functions from their corresponding electromagnetic structure functions in the AJM model.

For the resonance part, the γZ structure functions construction needs to modify the contribution from each resonance by the ratio ξ_R that considers the difference between the weak neutral and electromagnetic transition amplitudes. In the case of the transverse cross section, the ratio ξ_R, for the proton, has been defined as [158]

$$\xi_R = \frac{\sigma_{T,R}^{\gamma Z}}{\sigma_{T,R}^{\gamma\gamma}} = \Big(1 - 4\sin^2\theta_W(0)\Big) - y_R, \tag{7.12}$$

where

$$y_R = \frac{A^p_{R,\frac{1}{2}} A^{n*}_{R,\frac{1}{2}} + A^p_{R,\frac{3}{2}} A^{n*}_{R,\frac{3}{2}}}{|A^p_{R,\frac{1}{2}}|^2 + |A^p_{R,\frac{3}{2}}|^2}. \tag{7.13}$$

This ratio has also been used for the longitudinal cross section.

$A^N_{R,\lambda}$ is the transition amplitude from nucleon N to resonance R with helicity $\lambda = \frac{1}{2}, \frac{3}{2}$, and it is assumed to be Q^2 independent [158]. $A^N_{R,\lambda}$ values are estimated from electromagnetic decays at $Q^2 = 0$ [15].

In order to estimate the uncertainties to ξ_R for each resonance, the AJM model followed the standard Gaussian (normal) distribution approach [7]. For $P_{33}(1232)$ and $F_{37}(1950)$, according to the 2016 PDG [15], the uncertainties on their isospin structure should be zero. However, the AJM analysis adopted the conservative error assignment introduced in [158], where 10% and 100% errors have been assigned to y_R for the $P_{33}(1232)$ and $F_{37}(1950)$, respectively.

For the background part, the transverse and longitudinal electromagnetic cross sections can be transformed to their γZ counterparts by the ratio [7, 158]

$$\frac{\sigma_{T,L}^{\gamma Z}}{\sigma_{T,L}^{\gamma\gamma}} = \frac{k_\rho + k_\omega\ R_\omega^{T,L}(Q^2) + k_\phi\ R_\phi^{T,L}(Q^2) + k_C^{T,L}\ R_C^{T,L}(Q^2)}{1 + R_\omega^{T,L}(Q^2) + R_\phi^{T,L}(Q^2) + R_C^{T,L}(Q^2)}, \tag{7.14}$$

where the ratios $R_V^{T,L}$ are defined as the vector meson V cross sections normalised by the ρ meson cross section:

$$R_V^{T,L} = \frac{\sigma_{T,L}^{\gamma^* p \to V p}}{\sigma_{T,L}^{\gamma^* p \to \rho\ p}} = \frac{f_\rho^2}{f_V^2} \left(\frac{1 + Q^2/m_\rho^2}{1 + Q^2/m_V^2} \right)^2 , \tag{7.15}$$

with $V = \omega,\ \phi$. The vector meson V leptonic decay constant f_V, $f_V^2 \sim 1/r_V$, can be experimentally measured and hence $r_V = \{0.67, 0.062, 0.059\}$ for $V = \rho$, ω and ϕ [198]. The continuum part is represented by the ratios

$$R_C^T = \frac{r_C}{r_\rho} \left(\frac{1 + Q^2/m_\rho^2}{1 + Q^2/m_0^2} \right)^2 \tag{7.16}$$

and

$$R_C^L = \frac{r_C}{r_\rho} \left[\frac{m_0^2}{Q^2} \ln(1 + Q^2/m_0^2) - \frac{1}{1 + Q^2/m_0^2} \right] \Big/ \left[\frac{Q^2/m_\rho^2}{(1 + Q^2/m_\rho^2)^2} \right], \tag{7.17}$$

where $m_0 = 1.5$ GeV and $\frac{r_C}{r_\rho} = \frac{0.21}{0.67}$ [158]. r_C is the fraction from the continuous mass hadronic spectrum and is defined explicitly as

$$r_C = 1 - \sum_V r_V. \tag{7.18}$$

As can be seen, each term in the numerator of Eq. (7.14) is scaled by the ratio k_V. Here, a generalisation of the VMD model is adopted, assuming that the γZ cross section for vector meson V can be obtained from the purely electromagnetic cross section multiplied with the scaling ratio k_V:

$$\sigma_{T,L}^{\gamma Z(V)} = k_V\ \sigma_{T,L}^{\gamma\gamma(V)}, \tag{7.19}$$

where

$$\begin{aligned} k_\rho &= 2 - 4\sin^2\theta_W, \\ k_\omega &= \ -4\sin^2\theta_W, \\ k_\phi &= 3 - 4\sin^2\theta_W. \end{aligned} \tag{7.20}$$

The parameters $k_C^{T,L}$ represent the ratio of the γZ and $\gamma\gamma$ continuum contributions to the cross section. These parameters received considerable discussions in the literature as there is no simple approach to estimate their values. In the AJM model, the values of $k_C^{T,L}$ have been estimated by applying constraints from global QCD fits of PDFs. The AJM model introduced a significant reduction in the k_C^T uncertainty compared with that obtained in the GHRM model, which will be discussed in the next section. Conversely, the AJM model, obtained a large error on k_C^L. That error, however, has an insignificant impact on the estimation of $\Box_{\gamma Z}^V$.

An additional source for uncertainty on the background part stems from the ratios $R_\omega^{T,L}$ and $R_\phi^{T,L}$ in Eq. (7.14). The AJM model estimated this uncertainty by taking the discrepancy between these ratios determined in the VMD+Regge model at $Q^2 = 7$ GeV^2 and the measured vector meson production cross sections from HERA [199].

In the DIS region (Region III), the AJM model computed the γZ structure function from the ABM11 PDF parameterisation [197]. Due to the absence of interference structure functions at low Q^2, the authors of [197] have taken the values for the higher-twist contributions to $F_i^{\gamma Z}$ to be the same as for $F_i^{\gamma\gamma}$. Therefore, in the AJM model, a conservative 5% uncertainty on both $F_1^{\gamma Z}$ and $F_2^{\gamma Z}$ in the DIS region has been assigned.

7.2.3 GHRM Model

In the GHRM model, the VMD+Regge parameterisation has been extended to include the entire kinematic region of the dispersion integral.

In transforming the resonant part of the electromagnetic structure functions into their corresponding γZ structure functions, Gorchtein *et al.* [158] calculated the errors on the y_R, Eq. (7.12), parameters by taking into account the extreme values of the helicity amplitudes $A_{R,\lambda}^N$, where they assumed that the distribution is uniform. By adding the uncertainties linearly, the GHRM model produced very conservative errors on ξ_R.

In the GHRM model, the nonresonant background has been transformed by multiplying the VMD+Regge background with the ratio defined in Eq. (7.14). The main difference between the AJM and GHRM models is in the continuum term that contributes to the background error. Gorchtein *et al.* equated the purely electromagnetic and γZ interference continuum term and assigned a 100% uncertainty to this contribution.

7.3 Structure Functions from Lattice QCD

Beside the phenomenological models, the direct computation of structure functions via the hadronic tensor or Compton amplitude provide complementary methods. Therefore, in this section the structure functions within the lattice QCD framework will be highlighted.

The differential cross section for deep-inelastic scattering can be divided into leptonic and hadronic components. The hadronic tensor may be written in terms of the form factors $F_1(x, q^2)$ and $F_2(x, q^2)$ as

$$W_{\mu\nu}(p,q) = \Big(\delta_{\mu\nu} - \frac{q_\mu q_\nu}{q^2}\Big) F_1(x,q^2) + \frac{1}{p.q}\Big(p_\mu - \frac{p.q}{q^2} q_\mu\Big)\Big(p_\nu - \frac{p.q}{q^2} q_\nu\Big) F_2(x,q^2). \quad (7.21)$$

For unpolarised structure functions, the optical theorem relates the hadronic tensor to the forward Compton amplitude

$$T_{\mu\nu}(p,q) = \Big(\delta_{\mu\nu} - \frac{q_\mu q_\nu}{q^2}\Big) \mathcal{F}_1(\omega,q^2) + \frac{1}{p.q}\Big(p_\mu - \frac{p.q}{q^2} q_\mu\Big)\Big(p_\nu - \frac{p.q}{q^2} q_\nu\Big) \mathcal{F}_2(\omega,q^2), \quad (7.22)$$

where $\omega = 2p \cdot q/q^2$. By crossing symmetry, $T_{\mu\nu}(p,q) = T_{\mu\nu}(p,-q)$, hence $\mathcal{F}_1$ is an even function of ω and $\mathcal{F}_2$ an odd function, i.e., $\mathcal{F}_1(\omega,q^2) = \mathcal{F}_1(-\omega,q^2)$ and $-\mathcal{F}_2(\omega,q^2) = \mathcal{F}_2(-\omega,q^2)$. The discontinuity of the forward Compton amplitude through the cut starting at $\omega = 1$ in the complex ω plane gives the hadronic tensor for nucleon targets. In the physical range $1 \leq |\omega| \leq \infty$,

$$\Im m \mathcal{F}_{1,2}(\omega,q^2) = 2\pi F_{1,2}(\omega,q^2). \quad (7.23)$$

At large Q^2, the deep-inelastic structure functions can be described by the parton model. At low Q^2, however, the parton model cannot provide accurate descriptions of the rich structure of the inelastic scattering data.

A recent new lattice method to compute the structure functions directly from the product of electromagnetic currents was proposed in [8]. In that method, the direct calculation of the forward Compton amplitude via the Feynman-Hellmann technique has been performed. Applying the operator product expansion (OPE) to the forward Compton amplitude allows one to relate the structure functions $\mathcal{F}_{1,2}(\omega)$

to the Mellin moments of $F_{1,2}(\omega)$ as

$$\begin{aligned} T_{\mu\nu}(p,q) = \sum_{n=2,4,\ldots}^{\infty} \Big\{ &\Big(\delta_{\mu\nu} - \frac{q_\mu q_\nu}{q^2}\Big) 4\omega^n \int_0^1 dx x^{n-1} F_1(x,q^2) \\ &+ \Big(p_\mu - \frac{p.q}{q^2} q_\mu\Big)\Big(p_\nu - \frac{p.q}{q^2} q_\nu\Big) \frac{8}{2p.q} \omega^{n-1} \\ &\times \int_0^1 dx x^{n-2} F_2(x,q^2) \Big\}. \end{aligned} \tag{7.24}$$

Summing the geometric series in Eq. (7.24) enables the identification of specific components of the forward Compton amplitude. For example, choosing $\mu = \nu = 3$ and $P_3 = q_3 = q_4 = 0$ yields

$$T_{33}(p,q) = 4\omega^2 \int_0^1 dx \frac{x}{1-(\omega x)^2} F_1(x,q^2). \tag{7.25}$$

Fig. 7.3 represents lattice results for the proton Compton amplitude $T_{33}(p,q)$ for different momenta obtained in [8].

A possible extension to this method involves studying the γZ interference Compton amplitude $T_1^{\gamma Z}$. This leads to the question of what accuracy of $T_1^{\gamma Z}$ on lattice is necessary to improve the AJM or GHRM models. In the next section, Eq. (7.25) will be used to calculate $T_1^{\gamma Z}$, which in turn requires a brief discussion on $F_1^{\gamma Z}(x,Q^2)$.

7.4 Compton Amplitude $T_1^{\gamma Z}$ and Structure Function $F_1^{\gamma Z}$

The integral over x in Eq. (7.25) is divided into the pieces described in the AJM model. As the elastic piece is included, the elastic structure functions must also be considered. In elastic scattering, the response functions can be expressed in terms of combinations of squared electromagnetic form factors as [67]

$$\begin{aligned} W_1(\nu,Q^2) &= \frac{Q^2}{4M^2}(G_M^{\gamma p}(Q^2))^2 \delta\Big(\nu - \frac{Q^2}{2M}\Big), \\ W_2(\nu,Q^2) &= \frac{(G_E^{\gamma p}(Q^2))^2 + \frac{Q^2}{4M^2}(G_M^{\gamma p}(Q^2))^2}{1+\frac{Q^2}{4M^2}} \delta\Big(\nu - \frac{Q^2}{2M}\Big), \end{aligned} \tag{7.26}$$

where M is the nucleon mass, and $G_E^{\gamma p}(Q^2)$ and $G_M^{\gamma p}(Q^2)$ are the electric and magnetic form factors of the nucleon. The parameterisation of the nucleon EM form factors presented by Ye *et al.* in [180] is used in the current calculations. Similarly, in the case of the interference structure functions, these response functions can be defined

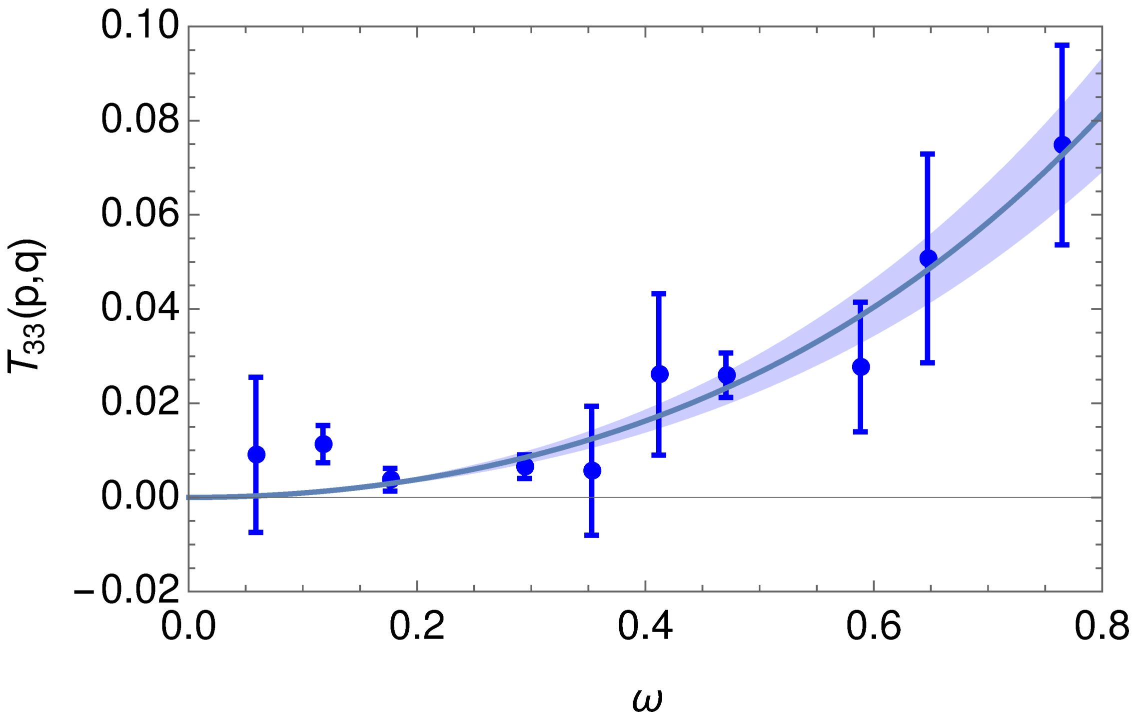

Figure 7.3: Lattice results for the proton Compton amplitude $T_{33}(p,q)$ [8].

as

$$W_1(\nu,Q^2) = \frac{Q^2}{4M^2}(G_M^{\gamma p}(Q^2)G_M^{Zp}(Q^2))\delta\Big(\nu - \frac{Q^2}{2M}\Big),$$
$$W_2(\nu,Q^2) = \frac{(G_E^{\gamma p}(Q^2)G_E^{Zp}(Q^2)) + \frac{Q^2}{4M^2}(G_M^{\gamma p}(Q^2)G_M^{Zp}(Q^2))}{1+\frac{Q^2}{4M^2}}\delta\Big(\nu - \frac{Q^2}{2M}\Big), \qquad (7.27)$$

where $G_{E,M}^{Zp}(Q^2)$ has been defined in Eq. (5.51), and the strangeness contribution is neglected and the assumption of charge symmetry is employed. From Eq. (7.26) or (Eq. (7.27) for γZ interference structure functions), $F_1(x,Q^2)$, which is relevant to the present study, can be defined as [67]

$$F_1(x,Q^2) = MW_1(\nu,Q^2). \qquad (7.28)$$

Following the AJM model, 5% uncertainty has been assigned to these elastic structure functions. From Eq. (7.25), $T_1^{\gamma Z}$ can be defined as

$$T_1^{\gamma Z} = 4\omega^2 \int_0^1 dx \frac{x}{1-(\omega x)^2} F_1^{\gamma Z}(x,q^2). \qquad (7.29)$$

Before proceeding to the calculations of the proton $T_1^{\gamma Z}$ at low Q^2, it is important to check the compatibility of the structure functions at the shared boundaries between the regions described in the AJM model. In Fig. 7.4, the structure function $F_1^{\gamma Z}(W^2, Q^2)$ has been plotted as a function of W^2 for various values of Q^2 running from Q^2= 0.05 to 10 GeV^2. It is obvious that the $F_1^{\gamma Z}$ shows good agreement at the common boundaries $W^2 = 4$, between the CB parameterisation (Region I, blue) and DIS structure function (Region III, green), and $W^2 = 9$ GeV^2 between the CB and VMD+Regge (Region II, red) parameterisations. The uncertainties on this structure function were included as described in the previous sections.

It is also instructive to show the behaviour of these regions as a function of Q^2 at fixed W^2. In Fig. 7.5, the $F_1^{\gamma Z}(W^2, Q^2)$ structure function has been plotted against Q^2 for multiple values of W^2 running from W^2= 4 to 12 GeV^2. $F_1^{\gamma Z}$ shows excellent matching at the boundaries between the regions. Furthermore, the DIS structure functions and the CB parameterisation are well-matched in the overlapping Q^2-W^2 plane.

In order to highlight the feature of the AJM model, where constraints from PDFs [197] were employed, a comparison with the proton $F_1^{\gamma Z}$ structure function in the GHRM model [158] is presented in Fig. 7.6 for fixed Q^2 (top panels) and fixed W^2 (bottom panels). As can be seen, the uncertainty on the resulting $F_1^{\gamma Z}$ structure function in the GHRM model is significantly overestimated compared to those obtained from the ABM11 parton distribution functions [197].

The structure functions presented in ABM11 [197] are given at kinematics that correspond to the squared momentum transferred greater than 0.6 GeV^2, i.e., overlap with the CB region. Using the fact that useful comparisons between several valid models in the same region are possible enables us to study the proton $T_1^{\gamma Z}$ for two different combinations of $F_1^{\gamma Z}$ for a common Q^2. As shown in Fig. 7.2, this common Q^2 can be chosen to be $Q^2 = 1$ GeV^2. Hence, in the current determination of $T_1^{\gamma Z}$, the two considered combinations are:

- combination I (comb. I): CB (blue, $W_\pi^2 \leq W^2 \leq 9$ GeV^2)+VMD+Regge (red, $W^2 > 9$ GeV^2)
- combination II (comb. II): CB (blue, $W_\pi^2 \leq W^2 \leq 4$ GeV^2)+PDF (green, $W^2 > 4$ GeV^2)

In Fig. 7.7, the determined $T_1^{\gamma Z}$ at $Q^2 = 1$ GeV^2 with comb. I (top panel) and comb. II (bottom panel) are depicted as a function of ω, which appears in Eq. (7.29), with their breakdowns into the contributions from the different regions. The total uncertainty is obtained by adding in quadrature the uncertainties from the relevant regions.

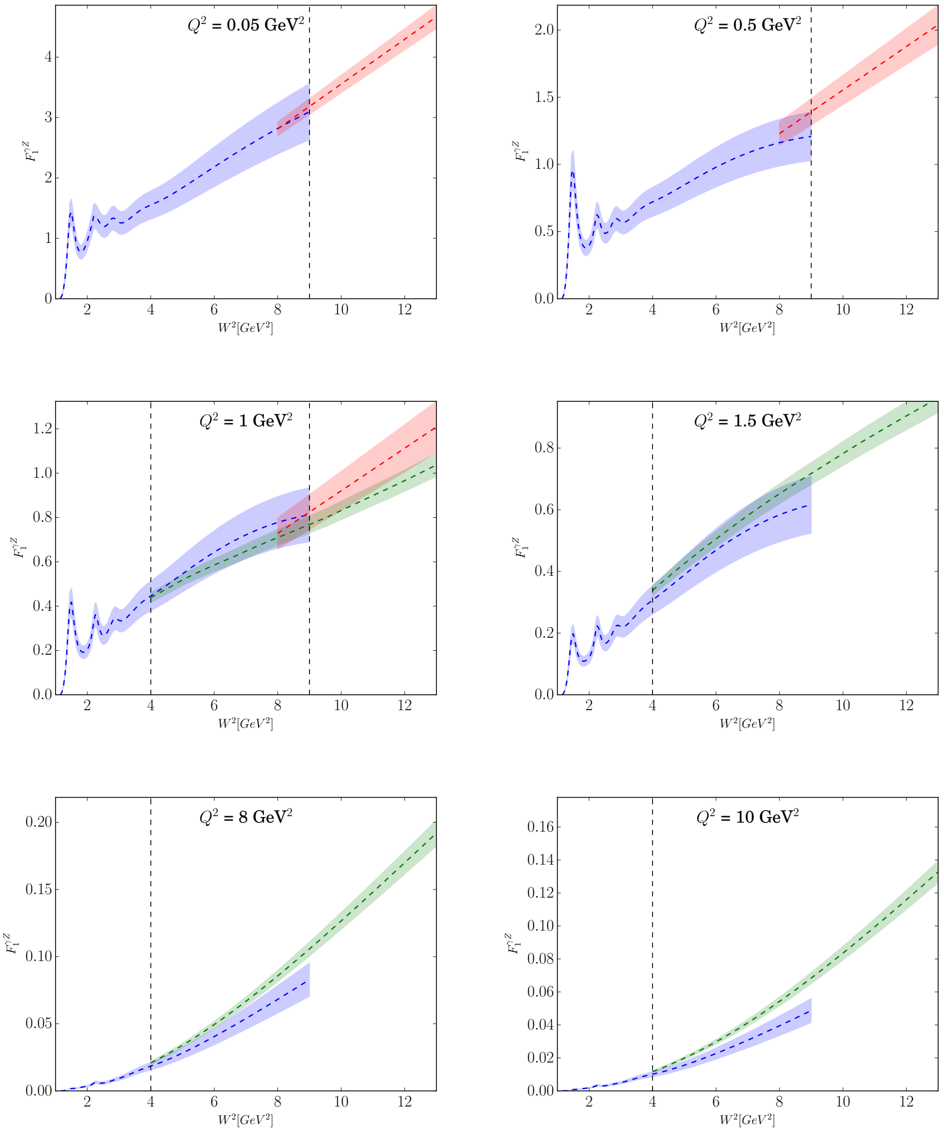

Figure 7.4: Proton $F_1^{\gamma Z}(W^2, Q^2)$ structure function against W^2 at fixed Q^2 = 0.05, 0.5, 1, 1.5, 8 and 10 GeV^2 for the CB parameterisation [192] (blue dashed), the VMD+Regge model [196] (red dashed) and the ABM11 PDF parameterisation [197](green dashed). The common borders between these regions are indicated by the vertical dashed lines at $W^2 = 4$ and 9 GeV^2.

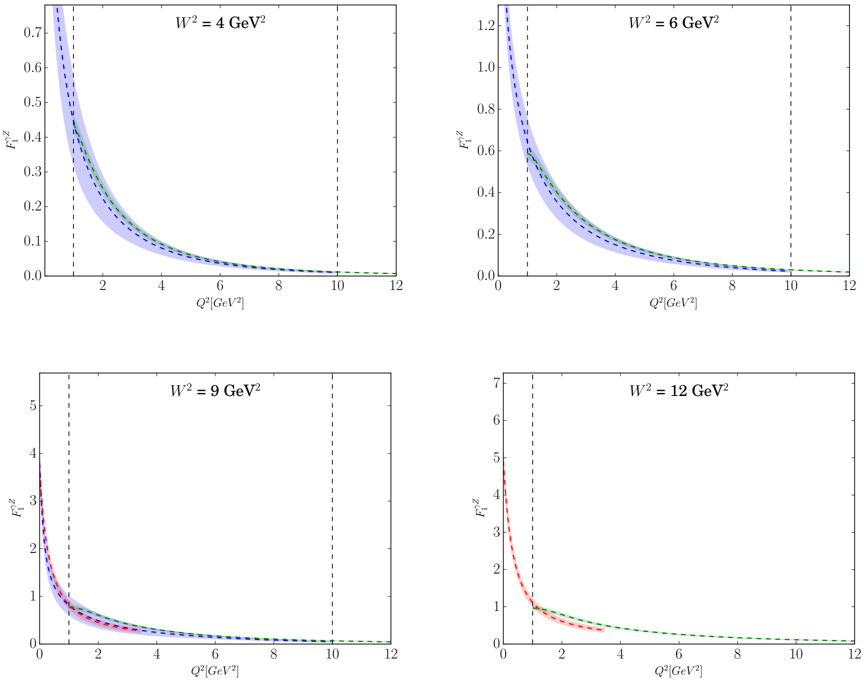

Figure 7.5: Proton $F_1^{\gamma Z}(W^2, Q^2)$ structure function against Q^2 at fixed $W^2 = 4$, 6, 9 and 12 GeV^2 for the CB parameterisation [192] (blue dashed), the VMD+Regge model [196] (red dashed) and the ABM11 PDF parameterisation [197](green dashed). The common borders between these regions are indicated by the vertical dashed lines at $Q^2 = 1$ and 10 GeV^2.

In Fig. 7.8, a comparison of $T_1^{\gamma Z}$ from both combinations is presented, and remarkable agreement is noted in both central curve and uncertainty. Consequently, this discussion will continue with one of these combinations.

In Fig. 7.9, a comparison of the estimated $T_1^{\gamma Z}$ from $F_1^{\gamma Z}$ in the AJM model with those obtained from $F_1^{\gamma Z}$ in the GHRM model at Q^2 =1 GeV^2 reveals that the $T_1^{\gamma Z}$ obtained from the GHRM model shows a larger uncertainty, and this is attributed to the continuum part treatment followed by Gorchtein *et al.* [158]. The central curves of $T_1^{\gamma Z}$ from the AJM model and its associated uncertainty are completely contained within the GHRM $T_1^{\gamma Z}$'s uncertainty. Looking more closely at Fig. 7.9, one can see that the difference between the uncertainties of the two models is more pronounced in the region between $\omega \sim 0.5$ and $\omega \sim 0.85$. Between these ω values, the GHRM model shows approximately a 20% relative error on $T_1^{\gamma Z}$.

In order to constrain the phenomenological models, the necessary accuracy of $T_1^{\gamma Z}$ on lattice QCD can be found by studying the difference between the calculated $T_1^{\gamma Z}$ from the GHRM and AJM models for low-Q^2 values. In Fig. 7.10, for fixed $Q^2 = 1$ GeV^2 (top panel) and $Q^2 = 0.5$ GeV^2 (bottom panel), the magnitude of the

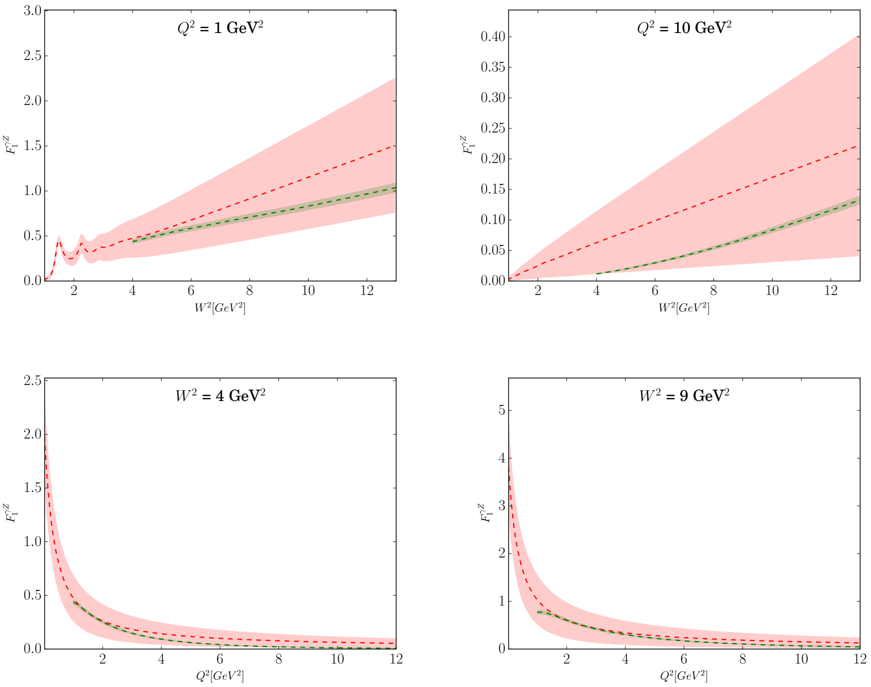

Figure 7.6: Comparison of the proton $F_1^{\gamma Z}(W^2, Q^2)$ structure function in the GHRM model [158] (red dashed) with the ABM11 parton distribution functions [197] (green dashed) for fixed Q^2 (top panels) and fixed W^2 (bottom panels).

difference has been plotted (dashed blue line) against ω, and the blue shaded area indicates the uncertainty of $T_1^{\gamma Z}$ from the GHRM model, while the dashed magenta line is the uncertainty of those from the AJM model around zero. The former line provides a baseline that can be used to estimate the required reduction on the uncertainty of $T_1^{\gamma Z}$ from the GHRM model. From Fig. 7.10 and the uncertainty of $T_1^{\gamma Z}$ from the AJM model, taking the percent error suggests a reduction of approximately 70% on $T_1^{\gamma Z}$'s uncertainty from the GHRM model at $Q^2 = 1.0$ and 0.5 GeV^2. This corresponds to a necessary reduction of the relative errors of lattice results for the proton Compton amplitude $T_{33}(p, q)$ presented in Fig 7.3, in particular the results obtained at ω between $\omega \sim 0.6$ and $\omega \sim 0.85$, roughly, to be between $\sim$ 20% and $\sim$ 8%.

7.5 Summary and Discussion

Recently, a new lattice method was proposed [8] to calculate the structure functions directly from the product of electromagnetic currents. There is a possibility that this method can be extended to study the γZ interference Compton amplitude $T_1^{\gamma Z}$.

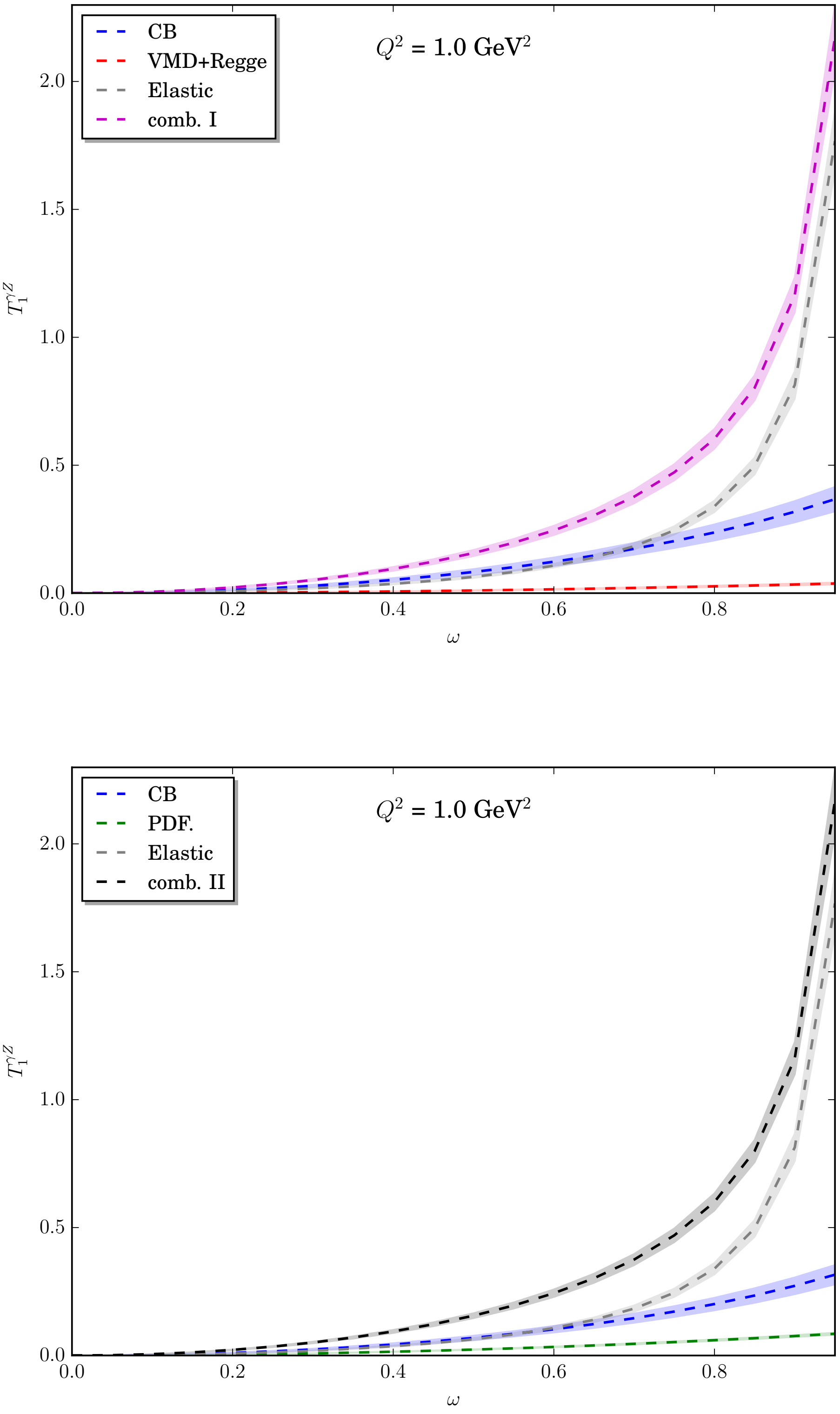

Figure 7.7: The determined proton $T_1^{\gamma Z}$ with comb. I (top panel) and with comb. II (bottom panel). The breakdown into the contributions from the different regions is shown. The total uncertainty is obtained by adding in quadrature the uncertainties from the relevant regions.

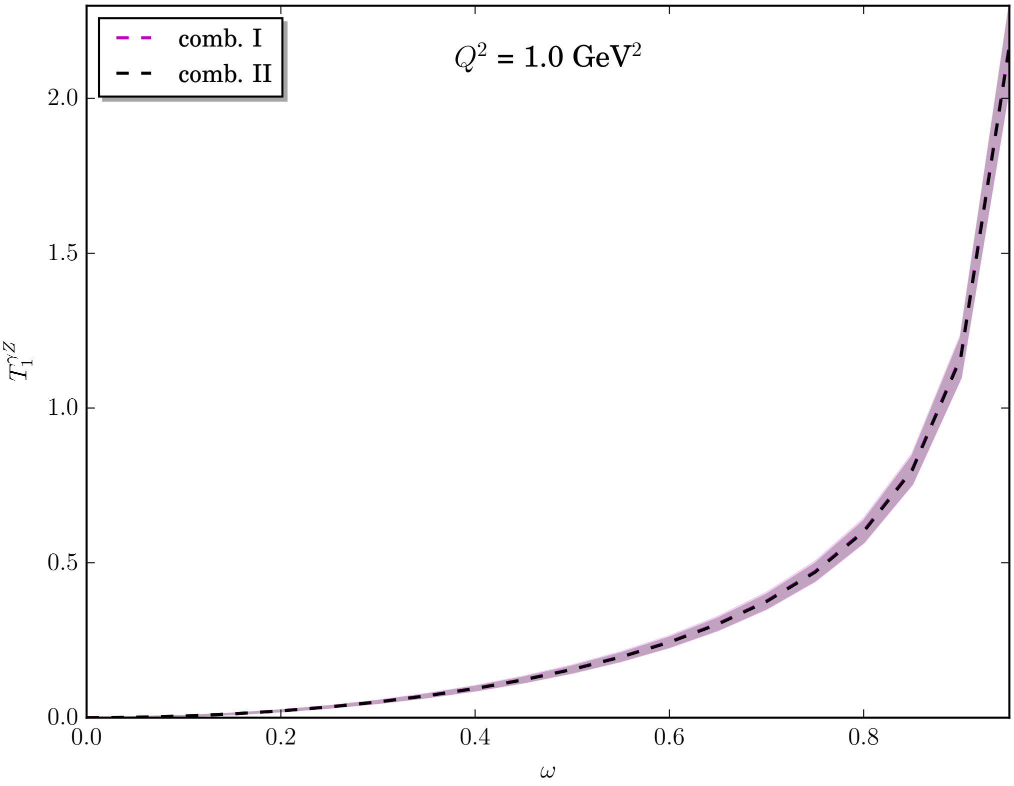

Figure 7.8: A comparison between the calculated proton $T_1^{\gamma Z}$ using comb. I and comb. II.

This chapter addressed the question regarding the necessary accuracy of $T_1^{\gamma Z}$ from the lattice at low Q^2 to constrain phenomenological models that have been used thus far to calculate the γZ box correction.

In order to accomplish the objectives of this study, two phenomenological models have been considered, the Adelaide-Jefferson Lab-Manitoba (AJM) model, as it obtained the most precise calculation of $\Box_{\gamma Z}^{V}(E)$, and the GHRM model, as it provided the largest uncertainty on the estimation of $\Box_{\gamma Z}^{V}(E)$.

Since the structure function $F_1^{\gamma Z}$ is relevant to the calculation of $T_1^{\gamma Z}$, the consistency of this structure function at the common boundaries between the regions described in the AJM model was investigated and it was found that $F_1^{\gamma Z}$ shows excellent matching at the boundaries between the regions. Furthermore, using Eq. (7.29), $T_1^{\gamma Z}$ has been calculated for two different combinations of $F_1^{\gamma Z}$ that can be obtained from the AJM model Q^2-W^2 plane for a common Q^2 value, i.e., $Q^2 = 1$ GeV^2, and a remarkable agreement has been found.

In order to improve the phenomenological models, the required accuracy of $T_1^{\gamma Z}$

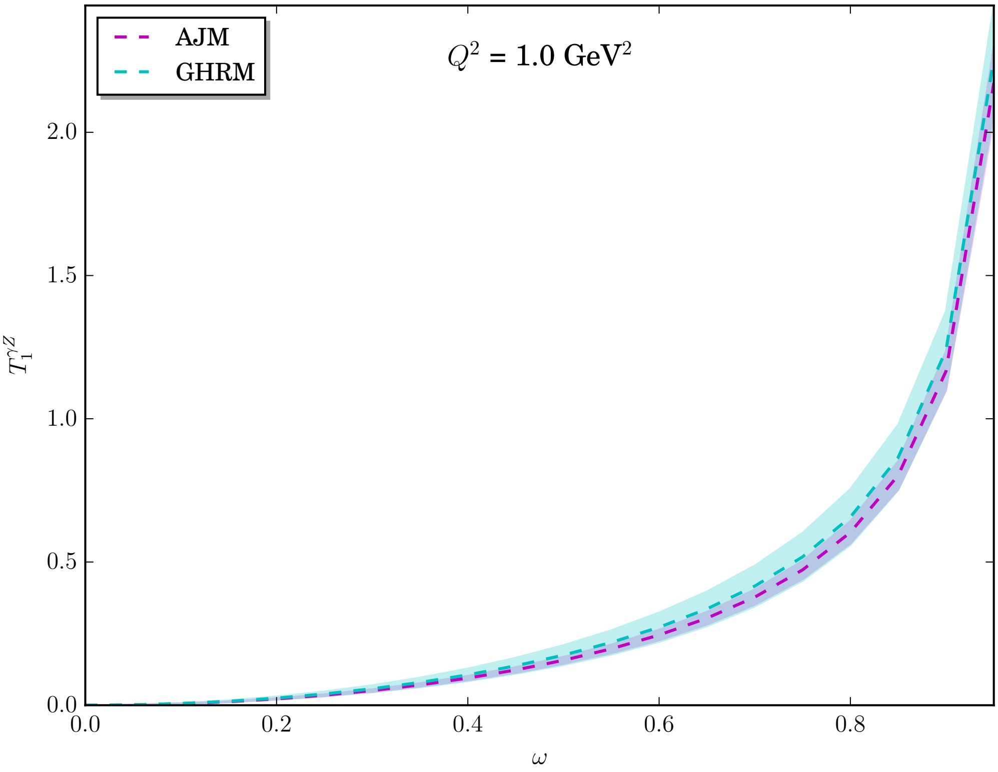

Figure 7.9: A comparison between the calculated proton $T_1^{\gamma Z}$ from the AJM and GHRM models at $Q^2 = 1$ GeV^2.

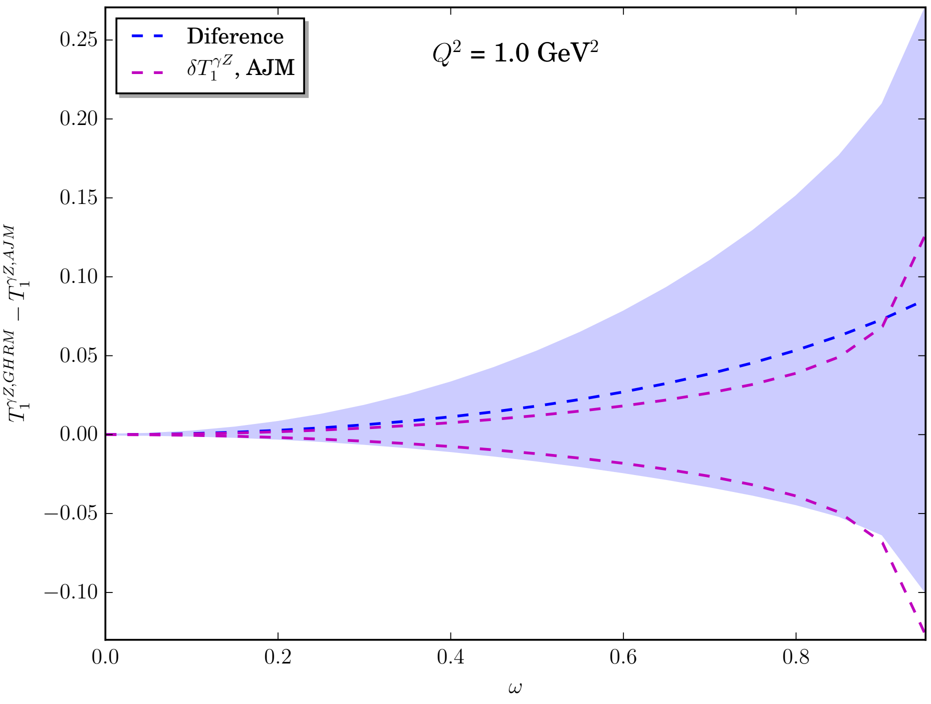

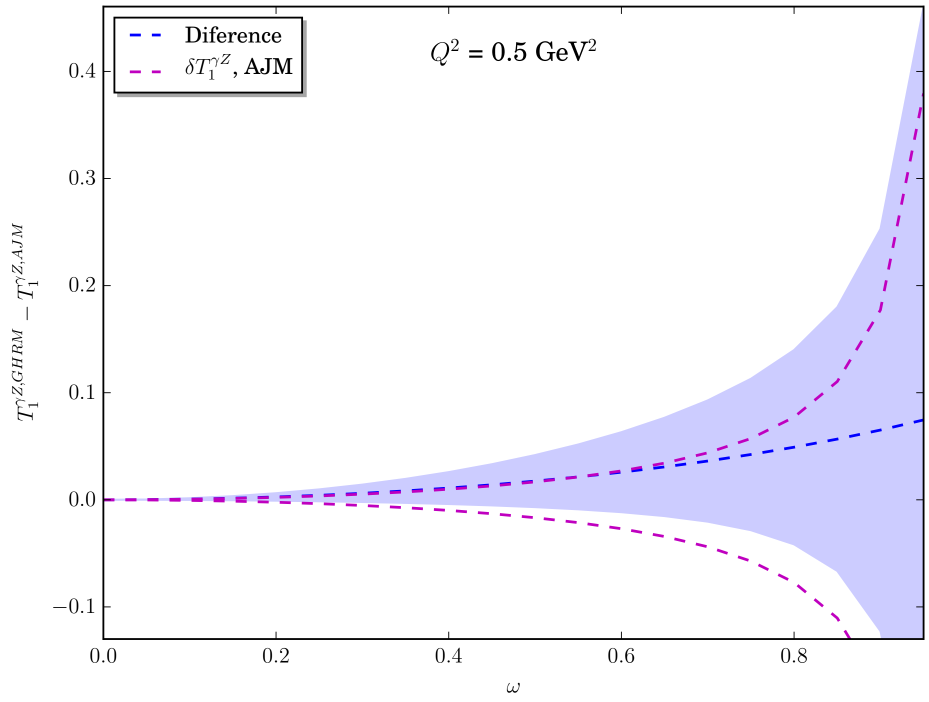

Figure 7.10: The magnitude of difference between the calculated $T_1^{\gamma Z}$ from the GHRM and AJM models (dashed blue line) at $Q^2 = 1$ GeV^2 (top panel) and $Q^2 = 0.5$ GeV^2 (bottom panel). The blue shaded area indicates the uncertainty of $T_1^{\gamma Z}$ from the GHRM model, while the dashed magenta line shows the uncertainty of those from the AJM model around zero.

from lattice QCD can be estimated by studying the difference between the calculated $T_1^{\gamma Z}$ from the GHRM and AJM models for low-Q^2 values. This study revealed that a large reduction on $T_1^{\gamma Z}$'s uncertainty from the GHRM model is needed. This necessitates a reduction of the relative errors of the lattice results of the Compton amplitude to be between $\sim 20\%$ and few percent.

In order to achieve this improvement, the lattice calculations are likely to require a two order magnitude increase in statistics.

Chapter 8

Summary and Conclusion

The investigation of the strange quark contributions, that would necessarily be related to the ‘sea’, is particularly interesting. The vector matrix elements of the strange quark, which contribute to the electromagnetic (EM) form factors of the nucleon, were the primary focus of this work. Within the context of studying the strange quark EM form factors contribution, the two quantities usually considered at low momentum transfers are the strange charge radius and strange magnetic moment. These quantities play a complementary role in low-energy precision measurements such as Q_{weak} and P2 experiments.

The parity-violating electron scattering (PVES) formalism, which connects the experimentally measured asymmetry to proton structure, was used in this work to perform a global analysis of all available world data up to $Q^2 \sim 1$ GeV^2 to determine the strange quark contribution. Under charge symmetry assumption, separation of the strange quark contributions to nucleon electromagnetic currents requires a third combination. This combination can be obtained using parity violating electron scattering from the proton, which determines the proton’s weak form factors. To build a coherent picture of this work, the importance of the PVES technique—which is a useful method in, for example, Q_{weak} precision measurements—was motivated as a starting point. In Chapter 3, the role of strangeness in nucleon structure has been highlighted to present a relevant perspective for studying the content of the strange quark of the neutral weak form factors. In Chapter 4, a review of the theoretical predictions of G_E^s and G_M^s was presented and it was emphasised that none of the theoretical approaches renders unambiguous estimates. Lattice QCD, as a first-principles approach to QCD, can give model-independent estimations. However, the majority of previous lattice QCD studies have been accomplished in the quenched approximation and only considered the calculation of the connected diagram contribution. Very recently, several extensive direct calculations of the nucleon’s strangeness form factors that involve calculations of the disconnected diagram contribution, which is considerably more computationally expensive, have been made. Therefore, in Chapter 5, the PVES formalism, as a tool to access information about the strange quark contributions, is introduced in detail along with a brief discussion on the radiative corrections.

In Chapter 6, a complete global analysis of all PVES asymmetry data, up to the currently available limit of $Q^2 \sim 1\text{GeV}^2$, for the proton, ^{4}He and deuteron has been performed. The Q^2-dependence of the strange quark electromagnetic form factors has been parameterised by a Taylor expansion in Q^2, and the nucleon effective axial form factor has been described by the dipole form factor with the aim to fit the entire contributions from the axial radiative and anapole corrections to the data. From the description of the Q^2-dependence, the global analysis was divided into a leading order (LO) global fit with four parameters $\tilde{g}_A^p$, $\tilde{g}_A^n$, μ_s and ρ_s, and next-to-leading order (NLO) fit of six parameters, namely, μ_s' and ρ_s' in addition to the previous four parameters.

To examine the model-dependence of employing a Taylor expansion in the analysis, a z-expansion fit was performed and was found that the determinations of the strangeness from factors from both expansions fits were in agreement.

The γZ exchange correction and the effect that the CSV form factors have on the extraction of the strange quark contribution have been studied. Including the γZ box contribution in the analysis resulted in small increases in the magnitude of the central values of μ_s and ρ_s when compared to results obtained without constraints from the γZ-exchange. The CSV results considered in this work have negligible effects on the central values of the strangeness parameters.

From the clustering of the considered data set, the separation of the electric and magnetic strange form factors is most reliable at the discrete momentum transfers near $Q^2 \sim 0.1$, 0.2 and 0.6 GeV^2. At $Q^2 = 0.63$ GeV^2, this work suggested non-zero strangeness, with a negative G_M^s and positive G_E^s. In contrast to earlier work that has suggested vanishing strangeness at this Q^2, the dominant difference in the present study is the treatment of the axial/anapole form factor. It was noted that the back-angle measurements show sensitivity to the effective axial form factor, presenting an opportunity for future investigation.

In addition, this study revealed an excellent agreement between the extracted strangeness based on the PVES data and lattice QCD results over the full Q^2 range.

The interpretation of the Q_{weak} collaboration results is subject to calculating the radiative corrections to the level of the required precision. The γZ box corrections have received special attention from the physics community since the other radiative corrections have been calculated to the level of Q_{weak} experiment precision. The γZ box correction, so far, is understood within phenomenological models such as Adelaide-Jefferson Lab-Manitoba (AJM).

Recently, a new lattice method was developed to calculate the structure functions directly from a lattice calculation of the electromagnetic Compton amplitude $T_1^{\gamma\gamma}$. This method opens the door for a possible extension which involves studying the γZ interference Compton amplitude $T_1^{\gamma Z}$ at low Q^2. In Chapter 7, the question of what accuracy of $T_1^{\gamma Z}$ on the lattice is necessary to improve the phenomenological models was studied, and was found that there is a possibility that structure functions can be computed from a lattice calculation of the Compton amplitude with the necessary accuracy to constrain the phenomenological models.

In summary, a complete global analysis of all PVES asymmetry data for the proton, ^{4}He and deuteron was presented to determine the strange quark contributions to the electromagnetic form factors of the proton. The γZ exchange correction and the effect that the CSV form factors have on the extraction of strangeness were investigated. The CSV form factors taken into account in this work have tiny impacts on the central values of the strangeness parameters. The results of this study provide an update to the determination of strangeness over a range of Q^2 where, under specific assumptions regarding the effective axial form factor, an non-zero strangeness is obtained in the vicinity of $Q^2 \sim 0.6$ GeV^2. The back-angle measurements have sensitivity to the effective axial form factor. This presents an opportunity for future investigation. The size of $\Box_{\gamma Z}$ correction is particularly significant to the Standard Model test by the Q_{weak} experiment. This correction can be constrained by phenomenological models. The significance of the $\Box_{\gamma Z}$ is somewhat less obvious in the determination of strangeness. Nevertheless, for example, the correction makes approximately $\sim \frac{1}{2}$-sigma shift to the central value of the precise HAPPEX proton point at $Q^2 \sim 0.1$ GeV^2. This study found that there is a possibility that structure functions can be calculated from a lattice calculation of the Compton amplitude with the necessary accuracy to improve these phenomenological models.

Appendix A

Notations and Conventions

A.1 Pauli Matrices

$$\tau_1 = \begin{pmatrix} 0 & 1 \\ 1 & 0 \end{pmatrix}, \qquad \tau_2 = \begin{pmatrix} 0 & -i \\ i & 0 \end{pmatrix}, \qquad \tau_3 = \begin{pmatrix} 1 & 0 \\ 0 & -1 \end{pmatrix}, \tag{A.1}$$

$$\vec{\tau} = (\tau_1, \tau_2, \tau_3), \tag{A.2}$$

$$\tau_\pm = \frac{1}{2}(\tau_1 \pm i\tau_2), \tag{A.3}$$

where $\tau_\pm$ are isospin raising and lowering matrices. These matrices satisfy the following properties:

- $\tau_1^2 = \tau_2^2 = \tau_3^2 = \begin{pmatrix} 1 & 0 \\ 0 & 1 \end{pmatrix} = I.$
- $\det(\tau_i)$=-1; $i = 1, 2, 3.$
- $\mathrm{Tr}[\tau_a \tau_b] = 2\delta_{ab}.$
- $\mathrm{Tr}[\tau_i]$=0; $i = 1, 2, 3.$
- $[\tau_a, \tau_b] = 2i\varepsilon_{abc}\tau_c.$
- $\{\tau_a, \tau_b\} = 2\delta_{ab}.I.$
- $\tau_a\tau_b = \delta_{ab}.I + i\varepsilon_{abc}\tau_c.$

The proton and neutron form an isospin $SU(2)$ doublet

$$|\text{proton}\rangle = |p\rangle = \begin{pmatrix} 1 \\ 0 \end{pmatrix}, \qquad |\text{neutron}\rangle = |n\rangle = \begin{pmatrix} 0 \\ 1 \end{pmatrix}. \tag{A.4}$$

Applying τ_3, isospin raising and lowering matrices to the nucleon states yields

$$\tau_3|p\rangle = |p\rangle, \quad \tau_3|n\rangle = -|n\rangle, \quad \tau_-|p\rangle = |n\rangle, \quad \tau_+|n\rangle = |p\rangle. \tag{A.5}$$

The electric charge of the nucleon can be written as

$$Q = \frac{1}{2}(B + \tau_3), \tag{A.6}$$

where baryon number $B = 1$. Analogous relations hold for the isospin doublet of u and d quarks, with the proton replaced by the u quark, the neutron by the d quark and baryon number $B = 1/3$ [67].

Appendix B

The Dispersion Relation

Because of the research of Kronig and Kramers in optics, the dispersion relations have been considered as a powerful tool to study many physics observables. The name dispersion is related to the optical dispersion. In general, dispersion theory relies on a few basic principles of physics: relativistic covariance, causality and unitarity [135]. A complete set of scattering amplitudes has to be created within the framework of the relativity and without kinematical singularities. The scattering amplitudes and vertex functions will, in general, contain both real and imaginary parts. The causality implies certain analytic properties of the analytic structure amplitudes, which enable for a continuation of the scattering amplitudes into the complex plane and lead to dispersion relations connecting the real and imaginary parts of these scattering amplitudes. Such dispersion relations have the following general form:

$$\Re e f(s) = \frac{1}{\pi} P \int_{s_0}^{\infty} ds' \frac{\Im m f(s')}{s' - s}, \tag{B.1}$$

where P is the Cauchy principle value. The above relation is a consequence of using Cauchy's integral formula. Using the identity

$$\frac{1}{x - x_0 - i\epsilon} = P \frac{1}{x - x_0} + i\pi\delta(x - x_0) \tag{B.2}$$

allows one to write the full scattering amplitude $f(s)$ as an integral over its imaginary part:

$$f(s) = \frac{1}{\pi} \int_{s_0}^{\infty} ds' \frac{\Im m f(s')}{s' - s - i\epsilon}. \tag{B.3}$$

The above dispersive integral involves all s'. Knowing $f(s)$ at small s requires an understanding of $\Im m f(s)$ at large s'. Therefore, the subtraction technique must be utilised to reduce the dependence on large s'. However, note that the integral still run over all s'. The subtracted dispersion relation can be written as

$$\frac{f(s) - f(0)}{s} = \frac{1}{\pi} \int_{s_0}^{\infty} \frac{ds'}{s' - s - i\epsilon} \Im m \left[\frac{f(s') - f(0)}{s'} \right]; \tag{B.4}$$

since $\Im m f(0) = 0$, the above dispersion relation can be reduced further to

$$f(s) = f(0) + \frac{s}{\pi} \int_{s_0}^{\infty} ds' \frac{\Im m f(s')}{s'(s' - s - i\epsilon)}. \tag{B.5}$$

The subtracted form of the dispersion relation may be required if $f(z) \neq 0$ as $|z| \to \infty$, as a good behaviour at infinity is required for the derivation of the dispersion relation. However, even if subtracted dispersion relations are not required, it may still be useful to perform dispersion relations, particularly in the context of effective field theories. The subtracted dispersion relation integral weights lower energies more heavily and reduces the influence of the high-energy region to the subtraction constant $f(0)$.

Appendix C

The Parameterisation of the Nucleon Form Factors

Ye *et al.* determined the proton and neutron EM form factors and the associated uncertainties using world electron scattering data [180]. In their analysis, the effects of two-photon exchange were incorporated.

This appendix presents the fit parameters of the electromagnetic nucleon form factors obtained by Ye *et al.* [180]. They performed a global fit procedure using the parameterisation of the systematic z-expansion:

$$G(Q^2) = \sum_{k=0}^{k_{\max}} a_k z^k, \; z = \frac{\sqrt{t_{cut} + Q^2} - \sqrt{t_{cut} - t_0}}{\sqrt{t_{cut} + Q^2} + \sqrt{t_{cut} - t_0}}, \tag{C.1}$$

where G refers to the G_E^p, G_M^p/μ_p, G_E^n and G_M^n/μ_n with $k_{\max} = 12$ for the proton and $k_{\max} = 10$ for the neutron. Here, $t_0 = -0.7$ GeV^2 and $t_{cut} = 4m_\pi^2$ with the charged pion mass $m_\pi = 0.13957$ GeV. The proton and neutron magnetic moments are given by $\mu_p = 2.79284356$ and $\mu_n = -1.91304272$, respectively.

C.1 Fitting Results

The fit parameters provided in Table C.1 are obtained from fits using radius constraints that are presented in Table C.2. For G_E^n, the 2016 PDG value $\langle (r_E^n)^2 \rangle = -0.1161(22)$ fm^2 was used.

Figs. C.1 and C.2 show the results of the fit for G_E^p and G_M^p normalised to the dipole form factor.

Table C.1: Fit parameters for the electromagnetic nucleon form factors obtained by Ye *et al.* [180] using the z-expansion parameterisation.

Parameter	G_E^p	G_M^p/μ_p	G_E^n	G_M^n/μ_n
a_0	0.23916	0.26414	0.04892	0.25776
a_1	−1.10986	−1.09531	−0.06453	−1.07954
a_2	1.44438	1.21855	−0.24083	1.18218
a_3	0.47957	0.66114	0.39211	0.71102
a_4	−2.28689	−1.40568	0.30045	−1.34808
a_5	1.12663	−1.35642	−0.66189	−1.66244
a_6	1.25062	1.44703	−0.17564	2.62435
a_7	−3.63102	4.23567	0.62469	1.75123
a_8	4.08222	−5.33405	−0.07768	−4.92230
a_9	0.50410	−2.91630	−0.23600	3.19789
a_{10}	−5.08512	8.70740	0.09040	−0.71207
a_{11}	3.96774	−5.70700	0	0
a_{12}	−0.98153	1.28081	0	0

Table C.2: Constrained values of form factor radii for G_E^p, G_M^p and G_M^n.

radius	output value (fm)	error (fm)
r_E^p	0.879	0.012
r_M^p	0.851	0.028
r_M^n	0.864	0.079

$$G_D = \frac{1}{\left(1 + \frac{Q^2}{\Lambda^2}\right)^2}, \tag{C.2}$$

where $\Lambda^2 = 0.71$ GeV^2.

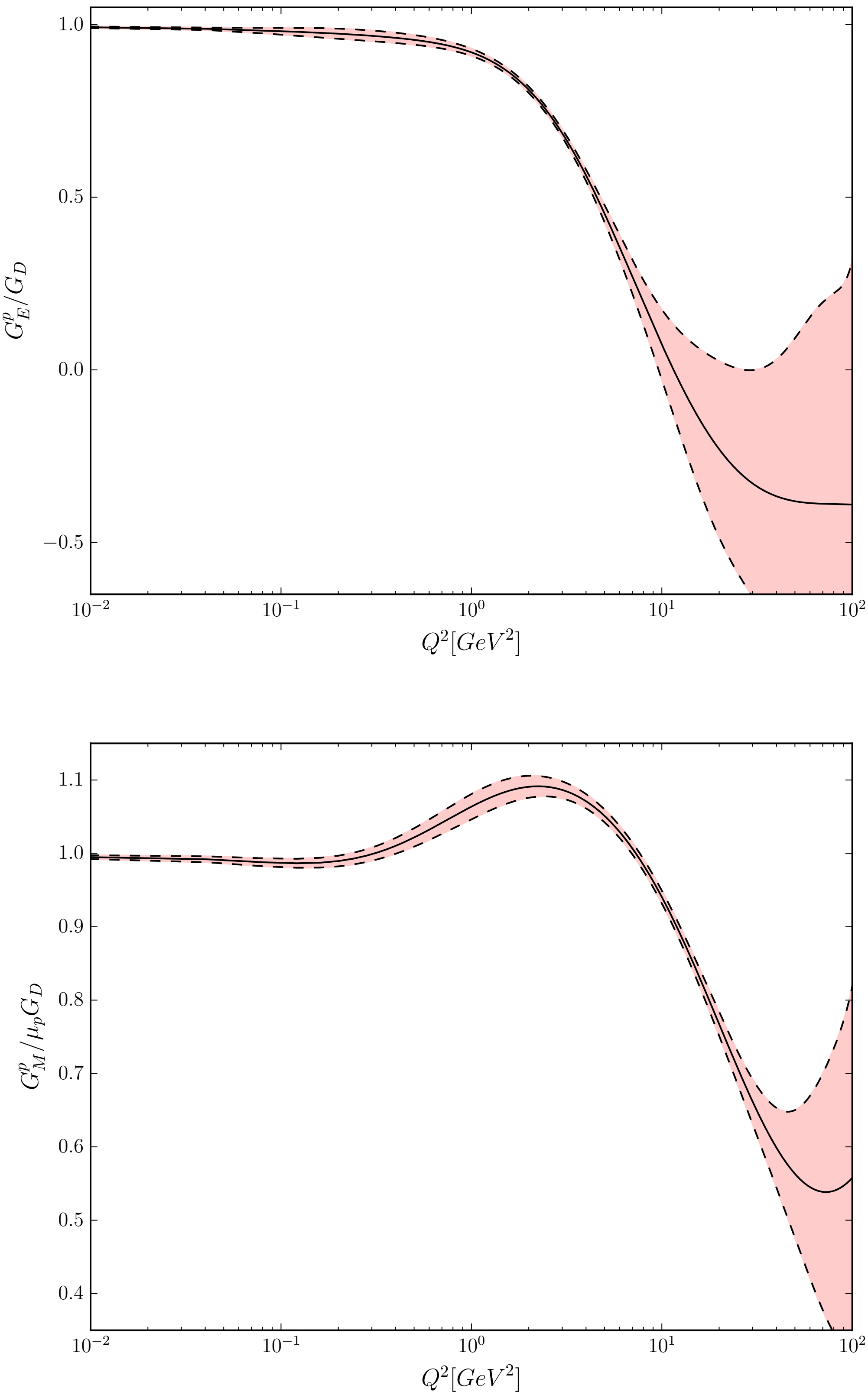

Figure C.1: Parameterisation of the G_E^p/G_D (upper) and $G_M^p/\mu_p G_D$ (lower), where the shaded areas reflect the total uncertainties as described in the global lift presented in [180].

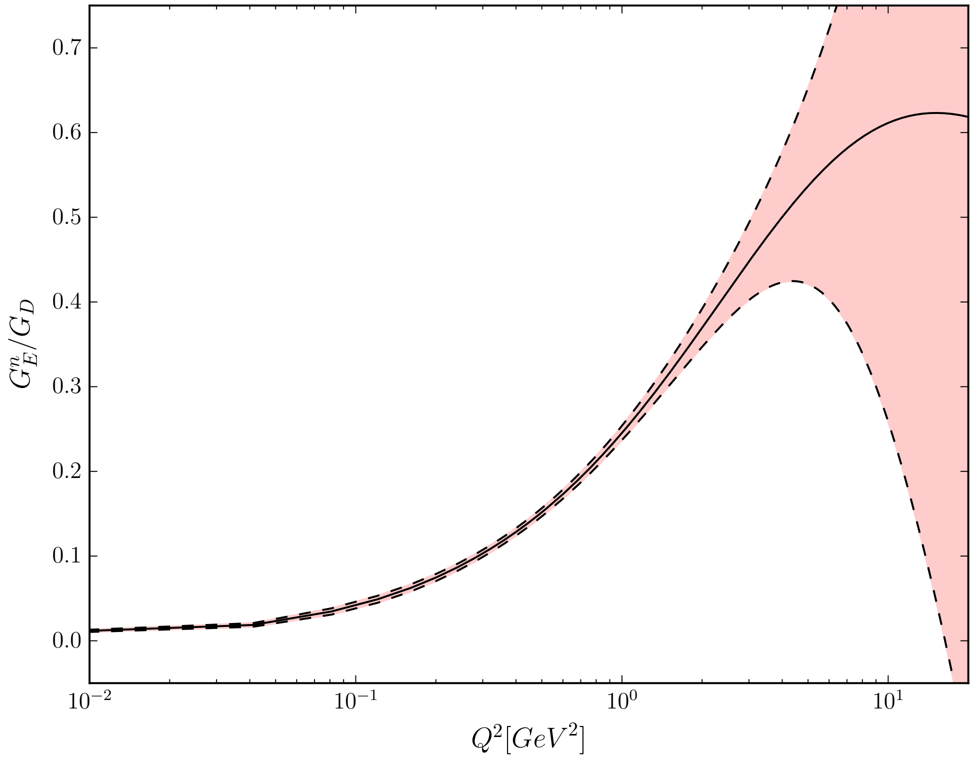

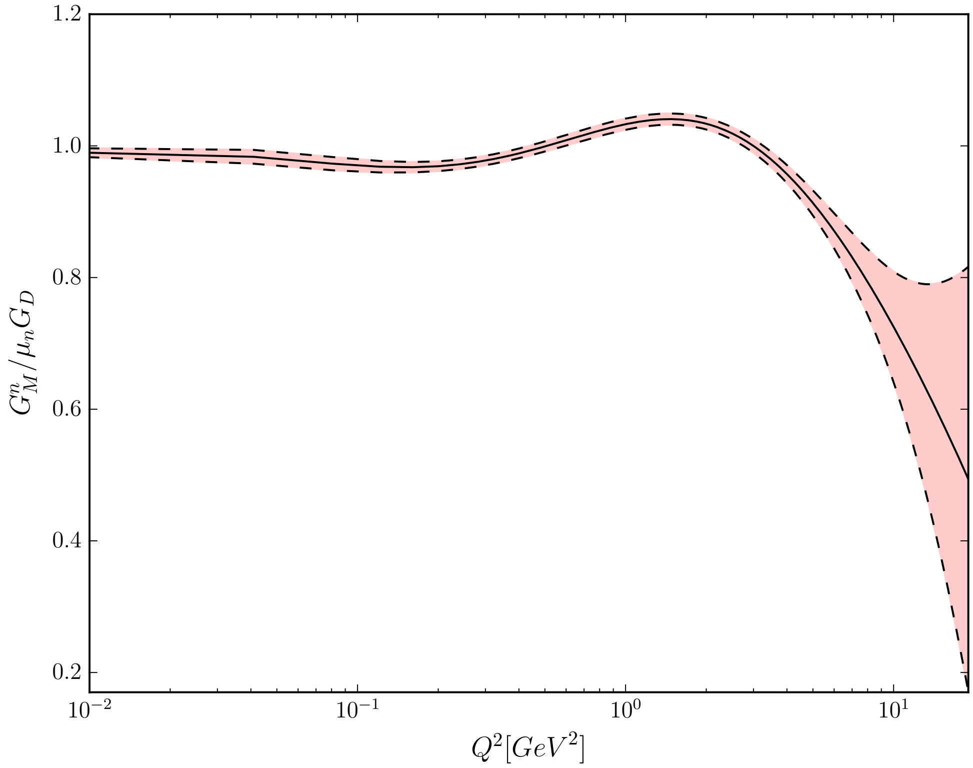

Figure C.2: Parameterisation of the G_E^n/G_D (upper) and $G_M^n/\mu_n G_D$ (lower), where the shaded areas reflect the total uncertainties as described in the global lift presented in [180].

Appendix D

List of Conferences, Workshop Proceedings, Submitted and Future Publications

- Ali Alkathiri, Ross D. Young and James M. Zanotti, *Interference electroweak structure functions*, in preparation.
- Ali Alkathiri, Ross D. Young and James M. Zanotti, *Charge symmetry violation in the determination of strangeness form factor*, submitted to Physical Review C, arXiv:1902.01590v1.
- Ali Alkathiri, Ross D. Young and James M. Zanotti, *Charge symmetry violation in the determination of strangeness form factor*, Oral presentation, 'QCD Downunder 2017 Workshop', Cairns, Australia, July 10-14, 2017.
- Ali Alkathiri, Ross D. Young and James M. Zanotti, *Charge symmetry violation in the determination of strangeness form factor*, poster presented at 'The International Nuclear Physics Conference 2016', Adelaide, Australia, September 11-16, 2016.

Bibliography

[1] D. B. Kaplan and A. Manohar, Nucl. Phys. **B310**, 527 (1988).

[2] R. D. Mckeown, Phys. Lett. **B219**, 140 (1989).

[3] D. H. Beck, Phys. Rev. **D39**, 3248 (1989).

[4] D. Androić *et al.* (Qweak), Nature **557**, 207 (2018).

[5] N. Berger *et al.*, J. Univ. Sci. Tech. China **46**, 481 (2016).

[6] M. Gorchtein and C. J. Horowitz, Phys. Rev. Lett. **102**, 091806 (2009).

[7] N. L. Hall, P. G. Blunden, W. Melnitchouk, A. W. Thomas, and R. D. Young, Phys. Rev. **D88**, 013011 (2013).

[8] A. J. Chambers, R. Horsley, Y. Nakamura, H. Perlt, P. E. L. Rakow, G. Schierholz, A. Schiller, K. Somfleth, R. D. Young, and J. M. Zanotti, Phys. Rev. Lett. **118**, 242001 (2017).

[9] K. S. Kumar, S. Mantry, W. J. Marciano, and P. A. Souder, Ann. Rev. Nucl. Part. Sci. **63**, 237 (2013).

[10] M. J. Musolf, T. W. Donnelly, J. Dubach, S. J. Pollock, S. Kowalski, and E. J. Beise, Phys. Rept. **239**, 1 (1994).

[11] A. Sirlin and A. Ferroglia, Rev. Mod. Phys. **85**, 263 (2013).

[12] G. Aad *et al.* (ATLAS), Phys. Lett. **B716**, 1 (2012).

[13] S. Chatrchyan *et al.* (CMS), Phys. Lett. **B716**, 30 (2012).

[14] P. Gagnon, *The Standard Model: a beautiful but flawed theory* (https://www.quantumdiaries.org, accessed 22 November 2018).

[15] C. Patrignani *et al.* (Particle Data Group), Chin. Phys. **C40**, 100001 (2016).

[16] S. L. Glashow, Nucl. Phys. **22**, 579 (1961).

[17] A. Salam, Conf. Proc. **C680519**, 367 (1968).

[18] S. Weinberg, Phys. Rev. Lett. **19**, 1264 (1967).

[19] G. S. Guralnik, C. R. Hagen, and T. W. B. Kibble, Phys. Rev. Lett. **13**, 585 (1964).

[20] F. Englert and R. Brout, Phys. Rev. Lett. **13**, 321 (1964).

[21] P. W. Higgs, Phys. Rev. Lett. **13**, 508 (1964).

[22] P. W. Higgs, Phys. Lett. **12**, 132 (1964).

[23] A. Sirlin, Phys. Rev. D **22**, 971 (1980).

[24] D. C. Kennedy, B. W. Lynn, C. J. C. Im, and R. G. Stuart, Nucl. Phys. **B321**, 83 (1989).

[25] D. Yu. Bardin, M. S. Bilenky, G. Mitselmakher, T. Riemann, and M. Sachwitz, Z. Phys. **C44**, 493 (1989).

[26] W. F. L. Hollik, Fortsch. Phys. **38**, 165 (1990).

[27] W. J. Marciano and A. Sirlin, Phys. Rev. Lett. **46**, 163 (1981).

[28] J. Erler and M. J. Ramsey-Musolf, Phys. Rev. **D72**, 073003 (2005).

[29] R. D. Young, R. D. Carlini, A. W. Thomas, and J. Roche, Phys. Rev. Lett. **99**, 122003 (2007).

[30] J. Erler, A. Kurylov, and M. J. Ramsey-Musolf, Phys. Rev. **D68**, 016006 (2003).

[31] B. Kubis and R. Lewis, Phys. Rev. **C74**, 015204 (2006).

[32] M. Wagman and G. A. Miller, Phys. Rev. **C89**, 065206 (2014), [Erratum: Phys. Rev. C91, 019903 (2015)].

[33] G. A. Miller, A. K. Opper, and E. J. Stephenson, Ann. Rev. Nucl. Part. Sci. **56**, 253 (2006).

[34] R. Lewis and N. Mobed, Phys. Rev. **D59**, 073002 (1999).

[35] P. E. Shanahan, R. Horsley, Y. Nakamura, D. Pleiter, P. E. L. Rakow, G. Schierholz, H. Stüben, A. W. Thomas, R. D. Young, and J. M. Zanotti, Phys. Rev. **D91**, 113006 (2015).

[36] R. Frisch and O. Stern, Z . Phys. **85**, 4 (1933).

[37] I. Estermann and O. Stern, Z . Phys. **85**, 17 (1933).

[38] L. W. Alvarez and F. Bloch, Phys. Rev. **57**, 111 (1940).

[39] M. Gell-Mann, Nuovo Cim. **4**, 848 (1956).

[40] T. Nakano and K. Nishijima, Prog. Theor. Phys. **10**, 581 (1953).

[41] K. Nishijima, Prog. Theor. Phys. **13**, 285 (1955).

[42] J. Gasser and H. Leutwyler, Nucl. Phys. **B250**, 465 (1985).

[43] R. D. Young, PoS **LATTICE2012**, 014 (2012).

[44] L. S. Brown, W. J. Pardee, and R. D. Peccei, Phys. Rev. **D4**, 2801 (1971).

[45] J. Gasser, H. Leutwyler, and M. E. Sainio, Phys. Lett. **B253**, 260 (1991).

[46] M. Hoferichter, J. Ruiz de Elvira, B. Kubis, and U.-G. Meißner, Phys. Rev. Lett. **115**, 092301 (2015).

[47] R. Horsley, Y. Nakamura, H. Perlt, D. Pleiter, P. E. L. Rakow, G. Schierholz, A. Schiller, H. Stuben, F. Winter, and J. M. Zanotti (QCDSF-UKQCD), Phys. Rev. **D85**, 034506 (2012).

[48] P. Junnarkar and A. Walker-Loud, Phys. Rev. **D87**, 114510 (2013).

[49] S. Durr *et al.*, Phys. Rev. Lett. **116**, 172001 (2016).

[50] Y.-B. Yang, A. Alexandru, T. Draper, J. Liang, and K.-F. Liu (xQCD), Phys. Rev. **D94**, 054503 (2016).

[51] A. Abdel-Rehim, C. Alexandrou, M. Constantinou, K. Hadjiyiannakou, K. Jansen, C. Kallidonis, G. Koutsou, and A. Vaquero Aviles-Casco (ETM), Phys. Rev. Lett. **116**, 252001 (2016).

[52] G. S. Bali *et al.*, Nucl. Phys. **B866**, 1 (2013).

[53] G. S. Bali, S. Collins, D. Richtmann, A. Schäfer, W. Söldner, and A. Sternbeck (RQCD), Phys. Rev. **D93**, 094504 (2016).

[54] G. S. Bali, S. Collins, and A. Schafer, Comput. Phys. Commun. **181**, 1570 (2010).

[55] S. Dinter, V. Drach, R. Frezzotti, G. Herdoiza, K. Jansen, and G. Rossi (ETM), JHEP **08**, 037 (2012).

[56] R. Babich, R. C. Brower, M. A. Clark, G. T. Fleming, J. C. Osborn, C. Rebbi, and D. Schaich, Phys. Rev. **D85**, 054510 (2012).

[57] R. P. Feynman, Phys. Rev. **56**, 340 (1939).

[58] J. Gasser and A. Zepeda, Nucl. Phys. **B174**, 445 (1980).

[59] M. Gell-Mann, R. J. Oakes, and B. Renner, Phys. Rev. **175**, 2195 (1968).

[60] G. Zweig, CERN Reports 8182/TH.401, 8419/TH.412 (1964).

[61] M. Gell-Mann, Phys. Lett. **8**, 214 (1964).

[62] K. Abe *et al.* (E143), Phys. Rev. **D58**, 112003 (1998).

[63] P. L. Anthony *et al.* (E155), Phys. Lett. **B493**, 19 (2000).

[64] J. R. Ellis and R. L. Jaffe, Phys. Rev. **D9**, 1444 (1974), [Erratum: Phys. Rev. D10, 1669 (1974)].

[65] J. D. Bjorken, Phys. Rev. **148**, 1467 (1966).

[66] J. D. Bjorken, Phys. Rev. **D1**, 1376 (1970).

[67] A. W. Thomas and W. Weise, *The Structure of the Nucleon* (Wiley-VCH, Berlin, Germany, 2001).

[68] S. A. Larin and J. A. M. Vermaseren, Phys. Lett. **B259**, 345 (1991).

[69] S. A. Larin, T. van Ritbergen, and J. A. M. Vermaseren, Phys. Lett. **B404**, 153 (1997).

[70] J. Ashman *et al.* (European Muon), Phys. Lett. **B206**, 364 (1988).

[71] B. W. Filippone and X.-D. Ji, Adv. Nucl. Phys. **26**, 1 (2001).

[72] E. Leader, A. V. Sidorov, and D. B. Stamenov, Eur. Phys. J. **C23**, 479 (2002).

[73] E. Leader, A. V. Sidorov, and D. B. Stamenov, Phys. Rev. **D67**, 074017 (2003).

[74] L. A. Ahrens *et al.*, Phys. Rev. **D35**, 785 (1987).

[75] G. T. Garvey, W. C. Louis, and D. H. White, Phys. Rev. **C48**, 761 (1993).

[76] S. F. Pate, D. W. McKee, and V. Papavassiliou, Phys. Rev. **C78**, 015207 (2008).

[77] S. Pate and D. Trujillo, EPJ Web Conf. **66**, 06018 (2014).

[78] S. D. Bass, Rev. Mod. Phys. **77**, 1257 (2005).

[79] V. Yu. Alexakhin *et al.* (COMPASS), Phys. Lett. **B647**, 8 (2007).

[80] C. A. Aidala, S. D. Bass, D. Hasch, and G. K. Mallot, Rev. Mod. Phys. **85**, 655 (2013).

[81] A. W. Thomas, Phys. Rev. Lett. **101**, 102003 (2008).

[82] Y.-B. Yang, R. S. Sufian, A. Alexandru, T. Draper, M. J. Glatzmaier, K.-F. Liu, and Y. Zhao, Phys. Rev. Lett. **118**, 102001 (2017).

[83] W. M. Alberico, S. M. Bilenky, and C. Maieron, Phys. Rept. **358**, 227 (2002).

[84] U. Dore, Eur. Phys. J. **H37**, 115 (2012).

[85] D. H. Beck and R. D. McKeown, Ann. Rev. Nucl. Part. Sci. **51**, 189 (2001).

[86] T. Adams *et al.* (NuTeV), PoS **EPIC–99**, 337 (1999).

[87] H. Abramowicz *et al.*, Z. Phys. **C15**, 19 (1982).

[88] S. A. Rabinowitz *et al.*, Phys. Rev. Lett. **70**, 134 (1993).

[89] A. O. Bazarko *et al.* (CCFR), Z. Phys. **C65**, 189 (1995).

[90] P. Vilain *et al.* (CHARM II), Eur. Phys. J. **C11**, 19 (1999).

[91] P. Astier *et al.* (NOMAD), Phys. Lett. **B486**, 35 (2000).

[92] O. Samoylov *et al.* (NOMAD), Nucl. Phys. **B876**, 339 (2013).

[93] M. Goncharov *et al.* (NuTeV), Phys. Rev. **D64**, 112006 (2001).

[94] G. P. Zeller *et al.* (NuTeV), Phys. Rev. Lett. **88**, 091802 (2002), [Erratum: Phys. Rev. Lett. 90, 239902 (2003)].

[95] G. P. Zeller *et al.* (NuTeV), Phys. Rev. **D65**, 111103 (2002), [Erratum: Phys. Rev. D67, 119902 (2003)].

[96] D. Mason *et al.* (NuTeV), Phys. Rev. Lett. **99**, 192001 (2007).

[97] A. Kayis-Topaksu *et al.* (CHORUS), Nucl. Phys. **B798**, 1 (2008).

[98] A. Kayis-Topaksu *et al.*, New J. Phys. **13**, 093002 (2011).

[99] M. Aaboud *et al.* (ATLAS), Eur. Phys. J. **C77**, 367 (2017).

[100] S. Weinberg, Physica **A96**, 327 (1979).

[101] J. Gasser and H. Leutwyler, Annals Phys. **158**, 142 (1984).

[102] E. E. Jenkins and A. V. Manohar, Phys. Lett. **B255**, 558 (1991).

[103] M. J. Musolf and H. Ito, Phys. Rev. **C55**, 3066 (1997).

[104] D. H. Beck and B. R. Holstein, Int. J. Mod. Phys. **E10**, 1 (2001).

[105] H. W. Hammer, S. J. Puglia, M. J. Ramsey-Musolf, and S.-L. Zhu, Phys. Lett. **B562**, 208 (2003).

[106] J. J. Sakurai, Annals Phys. **11**, 1 (1960).

[107] J. J. Sakurai, *Currents and Mesons* (Univ. of Chicago Press, Chicago, USA, 1969).

[108] R. P. Feynman, *Photon-Hadron Interactions* (W. A. Benjamin, Reading, USA, 1972).

[109] G. Hohler, E. Pietarinen, I. Sabba Stefanescu, F. Borkowski, G. G. Simon, V. H. Walther, and R. D. Wendling, Nucl. Phys. **B114**, 505 (1976).

[110] S. Okubo, Phys. Lett. **5**, 165 (1963).

[111] R. L. Jaffe, Phys. Lett. **B229**, 275 (1989).

[112] H. Forkel, Phys. Rev. **C56**, 510 (1997).

[113] M. J. Musolf and M. Burkardt, Z. Phys. **C61**, 433 (1994).

[114] W. Koepf, E. M. Henley, and S. J. Pollock, Phys. Lett. **B288**, 11 (1992).

[115] P. Geiger and N. Isgur, Phys. Rev. **D55**, 299 (1997).

[116] T. D. Cohen, H. Forkel, and M. Nielsen, Phys. Lett. **B316**, 1 (1993).

[117] J. F. Donoghue and B. R. Holstein, Phys. Lett. **B436**, 331 (1998).

[118] M. Malheiro and W. Melnitchouk, Phys. Rev. **C56**, R2373 (1997).

[119] U.-G. Meißner, V. Mull, J. Speth, and J. W. van Orden, Phys. Lett. **B408**, 381 (1997).

[120] H. Forkel, F. S. Navarra, and M. Nielsen, Phys. Rev. **C61**, 055206 (2000).

[121] Y. Nambu and G. Jona-Lasinio, Phys. Rev. **122**, 345 (1961).

[122] Y. Nambu and G. Jona-Lasinio, Phys. Rev. **124**, 246 (1961).

[123] V. Bernard, R. L. Jaffe, and U.-G. Meißner, Nucl. Phys. **B308**, 753 (1988).

[124] H. Forkel, M. Nielsen, X.-m. Jin, and T. D. Cohen, Phys. Rev. **C50**, 3108 (1994).

[125] H. Weigel, A. Abada, R. Alkofer, and H. Reinhardt, Phys. Lett. **B353**, 20 (1995).

[126] H. Yabu and K. Ando, Nucl. Phys. **B301**, 601 (1988).

[127] C. S. An and B. Saghai, Phys. Rev. **C88**, 025206 (2013).

[128] B. S. Zou and D. O. Riska, Phys. Rev. Lett. **95**, 072001 (2005).

[129] T. H. R. Skyrme, Proc. Roy. Soc. Lond. **A260**, 127 (1961).

[130] T. H. R. Skyrme, Nucl. Phys. **31**, 556 (1962).

[131] N. W. Park, J. Schechter, and H. Weigel, Phys. Rev. **D43**, 869 (1991).

[132] A. Silva, H.-C. Kim, and K. Goeke, Phys. Rev. **D65**, 014016 (2002), [Erratum: Phys. Rev. D66, 039902 (2002)].

[133] A. Silva, H.-C. Kim, and K. Goeke, Eur. Phys. J. **A22**, 481 (2004).

[134] S.-T. Hong, B.-Y. Park, and D.-P. Min, Phys. Lett. **B414**, 229 (1997).

[135] D. Drechsel, B. Pasquini, and M. Vanderhaeghen, Phys. Rept. **378**, 99 (2003).

[136] M. J. Musolf, H. W. Hammer, and D. Drechsel, Phys. Rev. **D55**, 2741 (1997), [Erratum: Phys. Rev. D62, 079901 (2000)].

[137] M. J. Ramsey-Musolf and H. W. Hammer, Phys. Rev. Lett. **80**, 2539 (1998).

[138] H. W. Hammer and M. J. Ramsey-Musolf, Phys. Rev. **C60**, 045204 (1999), [Erratum: Phys. Rev. C62, 049902 (2000)].

[139] H. W. Hammer and M. J. Ramsey-Musolf, Phys. Rev. **C60**, 045205 (1999), [Erratum: Phys. Rev. C62, 049903 (2000)].

[140] H. W. Hammer and M. J. Ramsey-Musolf, Phys. Lett. **B416**, 5 (1998).

[141] K. G. Wilson, Phys. Rev. **D10**, 2445 (1974).

[142] J. N. Labrenz and S. R. Sharpe, Phys. Rev. **D54**, 4595 (1996).

[143] S. J. Dong, K. F. Liu, and A. G. Williams, Phys. Rev. **D58**, 074504 (1998).

[144] N. Mathur and S.-J. Dong (Kentucky Field Theory), Nucl. Phys. Proc. Suppl. **94**, 311 (2001).

[145] D. B. Leinweber, Phys. Rev. **D53**, 5115 (1996).

[146] D. B. Leinweber and A. W. Thomas, Phys. Rev. **D62**, 074505 (2000).

[147] D. B. Leinweber, S. Boinepalli, I. C. Cloet, A. W. Thomas, A. G. Williams, R. D. Young, J. M. Zanotti, and J. B. Zhang, Phys. Rev. Lett. **94**, 212001 (2005).

[148] P. E. Shanahan, R. Horsley, Y. Nakamura, D. Pleiter, P. E. L. Rakow, G. Schierholz, H. Stüben, A. W. Thomas, R. D. Young, and J. M. Zanotti, Phys. Rev. Lett. **114**, 091802 (2015).

[149] J. Green, S. Meinel, M. Engelhardt, S. Krieg, J. Laeuchli, J. Negele, K. Orginos, A. Pochinsky, and S. Syritsyn, Phys. Rev. **D92**, 031501 (2015).

[150] T. Doi, M. Deka, S.-J. Dong, T. Draper, K.-F. Liu, D. Mankame, N. Mathur, and T. Streuer, Phys. Rev. **D80**, 094503 (2009).

[151] R. S. Sufian, Y.-B. Yang, A. Alexandru, T. Draper, J. Liang, and K.-F. Liu (χQCD Collaboration), Phys. Rev. Lett. **118**, 042001 (2017).

[152] R. G. Sachs, Phys. Rev. **126**, 2256 (1962).

[153] S. Galster, H. Klein, J. Moritz, K. H. Schmidt, D. Wegener, and J. Bleckwenn, Nucl. Phys. **B32**, 221 (1971).

[154] E. J. Beise, M. L. Pitt, and D. T. Spayde, Prog. Part. Nucl. Phys. **54**, 289 (2005).

[155] G. S. Bali *et al.* (QCDSF), Phys. Rev. Lett. **108**, 222001 (2012).

[156] A. Sibirtsev, P. G. Blunden, W. Melnitchouk, and A. W. Thomas, Phys. Rev. **D82**, 013011 (2010).

[157] B. C. Rislow and C. E. Carlson, Phys. Rev. **D83**, 113007 (2011).

[158] M. Gorchtein, C. J. Horowitz, and M. J. Ramsey-Musolf, Phys. Rev. **C84**, 015502 (2011).

[159] P. G. Blunden, W. Melnitchouk, and A. W. Thomas, Phys. Rev. Lett. **107**, 081801 (2011).

[160] S.-L. Zhu, S. J. Puglia, B. R. Holstein, and M. J. Ramsey-Musolf, Phys. Rev. **D62**, 033008 (2000).

[161] K. S. Kumar and P. A. Souder, Prog. Part. Nucl. Phys. **45**, S333 (2000).

[162] R. D. Young, J. Roche, R. D. Carlini, and A. W. Thomas, Phys. Rev. Lett. **97**, 102002 (2006).

[163] C. Y. Prescott *et al.*, Phys. Lett. **B77**, 347 (1978).

[164] D. S. Armstrong *et al.* (G0), Phys. Rev. Lett. **95**, 092001 (2005).

[165] D. Androic *et al.* (G0), Phys. Rev. Lett. **104**, 012001 (2010).

[166] T. M. Ito *et al.* (SAMPLE), Phys. Rev. Lett. **92**, 102003 (2004).

[167] A. Acha *et al.* (HAPPEX), Phys. Rev. Lett. **98**, 032301 (2007).

[168] K. A. Aniol *et al.* (HAPPEX), Phys. Rev. Lett. **96**, 022003 (2006).

[169] K. A. Aniol *et al.* (HAPPEX), Phys. Lett. **B635**, 275 (2006).

[170] D. T. Spayde *et al.* (SAMPLE), Phys. Lett. **B583**, 79 (2004).

[171] F. E. Maas *et al.*, Phys. Rev. Lett. **94**, 152001 (2005).

[172] S. Baunack *et al.*, Phys. Rev. Lett. **102**, 151803 (2009).

[173] D. Balaguer Ros *et al.*, Phys. Rev. **D94**, 051101 (2016).

[174] F. E. Maas *et al.* (A4), Phys. Rev. Lett. **93**, 022002 (2004).

[175] K. A. Aniol *et al.* (HAPPEX), Phys. Rev. **C69**, 065501 (2004).

[176] Z. Ahmed *et al.* (HAPPEX), Phys. Rev. Lett. **108**, 102001 (2012).

[177] N. L. Hall, P. G. Blunden, W. Melnitchouk, A. W. Thomas, and R. D. Young, Phys. Lett. **B753**, 221 (2016).

[178] W. J. Marciano and A. Sirlin, Phys. Rev. **D27**, 552 (1983).

[179] W. J. Marciano and A. Sirlin, Phys. Rev. **D29**, 75 (1984), [Erratum: Phys. Rev. D31, 213 (1985)].

[180] Z. Ye, J. Arrington, R. J. Hill, and G. Lee, Phys. Lett. **B777**, 8 (2018).

[181] V. Bernard, L. Elouadrhiri, and U.-G. Meißner, J. Phys. **G28**, R1 (2002).

[182] J. Liu, R. D. McKeown, and M. J. Ramsey-Musolf, Phys. Rev. **C76**, 025202 (2007).

[183] R. González-Jiménez, J. A. Caballero, and T. W. Donnelly, Phys. Rev. **D90**, 033002 (2014).

[184] D. B. Leinweber, S. Boinepalli, A. W. Thomas, P. Wang, A. G. Williams, R. D. Young, J. M. Zanotti, and J. B. Zhang, Phys. Rev. Lett. **97**, 022001 (2006).

[185] P. Wang, D. B. Leinweber, A. W. Thomas, and R. D. Young, Phys. Rev. **C79**, 065202 (2009).

[186] Z. Epstein, G. Paz, and J. Roy, Phys. Rev. **D90**, 074027 (2014).

[187] R. J. Hill and G. Paz, Phys. Rev. **D82**, 113005 (2010).

[188] R. E. Cutkosky and B. B. Deo, Phys. Rev. **174**, 1859 (1968).

[189] O. Moreno, T. W. Donnelly, R. González-Jiménez, and J. A. Caballero, J. Phys. **G42**, 034006 (2015).

[190] M. Viviani, R. Schiavilla, B. Kubis, R. Lewis, L. Girlanda, A. Kievsky, L. E. Marcucci, and S. Rosati, Phys. Rev. Lett. **99**, 112002 (2007).

[191] J. Arrington, P. G. Blunden, and W. Melnitchouk, Prog. Part. Nucl. Phys. **66**, 782 (2011).

[192] M. E. Christy and P. E. Bosted, Phys. Rev. **C81**, 055213 (2010).

[193] G. Cvetic, D. Schildknecht, B. Surrow, and M. Tentyukov, Eur. Phys. J. **C20**, 77 (2001).

[194] A. Donnachie and P. V. Landshoff, Phys. Lett. **B296**, 227 (1992).

[195] J. J. Sakurai and D. Schildknecht, Phys. Lett. **40B**, 121 (1972).

[196] J. Alwall and G. Ingelman, Phys. Lett. **B596**, 77 (2004).

[197] S. Alekhin, J. Blumlein, and S. Moch, Phys. Rev. **D86**, 054009 (2012).

[198] T. H. Bauer, R. D. Spital, D. R. Yennie, and F. M. Pipkin, Rev. Mod. Phys. **50**, 261 (1978), [Erratum: Rev. Mod. Phys. 51, 407 (1979)].

[199] J. Breitweg *et al.* (ZEUS), Phys. Lett. **B487**, 273 (2000).